2D α-In_2Se_3 UNDER STRAIN AND FERROELECTRIC NEUROMORPHIC COMPUTING APPLICATIONS

GUO FENG

PhD

The Hong Kong Polytechnic University

2022

The Hong Kong Polytechnic University

Department of Applied Physics

2D α-In_2Se_3 Under Strain And Ferroelectric Neuromorphic Computing Applications

GUO FENG

A thesis submitted in partial fulfillment of the requirements for the degree of Doctor of Philosophy

January 2022

CERTIFICATE OF ORIGINALITY

I hereby declare that this thesis is my own work and that, to the best of my knowledge and belief, it reproduces no material previously published or written, nor material that has been accepted for the award of any other degree or diploma, except where due acknowledgement has been made in the text.

_____(Signed)

GUO Feng (Name of student)

Abstract

Since the discovery of graphene, the family of 2D materials covering insulators, semiconductors, and metals has been extensively studied in the field of optoelectronics and provides an excellent platform to explore fantastic physical phenomena at the atomic level. As a subgroup, 2D piezoelectric and ferroelectric materials offer an additional degree of freedom to modulate the optoelectronic properties of the material and multifunctionalize the device with the help of ferroelectricity and piezoelectricity.

In this thesis, firstly, the controllable biaxial strain is experimentally imposed on α-In_2Se_3 nanosheets by an electromechanical device. A red shift of Raman spectra of the nanosheets is observed under the strain. The Grüneisen parameter is calculated to analyze the strain effect on the vibrational behavior. Photoluminescence shows a blue shift which can reach up to 215 meV per 1% strain. Such tunability of optical characteristics observed from α-In_2Se_3 nanosheets is much higher than that of conventional semiconductors. Physical mechanism behind the observation is investigated, which is related to the variations in energy band and photoexcited carriers under piezoelectric field and laser power.

Secondly, 2D ferroelectric α-In_2Se_3 is utilized as the channel to construct a novel artificial neuron with an easy-to-prepare structure. And both of linearly separable and nonseparable logic can be performed at the single device level rather than a network based on the principle of combinational and stateful logic, respectively. Compared to the traditional design based on CMOS, the transistor resource can be decreased to 1/6 for XOR logic gate. In addition, as artificial neurons,

there is a high demand for implementing flexible and adaptable behaviors. Thus, the behaviors of multi-terminal synapses are exhibited and the ability to modulate synaptic weights is investigated. Specifically, controlling food intake as a complex nervous system-level behavior is integrated to carry out positive and negative feedback in our device for the first time.

Thirdly, a novel multifunctional synaptic device based on ferroelectric α-In_2Se_3/GaSe vdW heterostructure is proposed to emulate the entire biological visual system. Essential synaptic behaviors were observed in response to light and electrical stimuli; additionally, the retina-like selectivity for light wavelengths and the achievement of Pavlov's dog experiment demonstrate the device's capacity for processing complex electrical and optical inputs. Beyond the optoelectronic synaptic behaviors, the device incorporates memory and logic functions analogous to those in brain's visual cortex. The results of artificial neural network simulations show that the vdW heterostructure-based device is completely capable of performing logic operations and recognizing image with a high degree of accuracy.

In conclusion, our work demonstrates the ability of piezoelectric fields induced by strain to modulate the energy band structure of 2D materials, and the working mechanism is analyzed in detail. Electronic and optoelectronic synaptic devices are designed based on 2D ferroelectric α-In_2Se_3 which exhibits great potential for breaking the bottleneck of von Neumann computers and simplifying current artificial neural networks as well as artificial vision systems.

List of Publications

Journal Papers

1. **Feng Guo**, Yongxin Lyu, Michal Bartlomiej Jedrzejczyk, Yuqian Zhao, Weng Fu Io, Gongxun Bai, Wenzhuo Wu, and Jianhua Hao. "Piezoelectric biaxial strain effects on the optical and photoluminescence spectra of 2D III–VI compound α-In_2Se_3 nanosheets." *Applied Physics Letters* 116, 11 (2020): 113101.

2. **Feng Guo**, Menglin Song, Man-Chung Wong, Ran Ding, Weng Fu Io, Sin-Yi Pang, Wenjing Jie, and Jianhua Hao. "Multifunctional Optoelectronic Synapse Based on Ferroelectric Van der Waals Heterostructure for Emulating the Entire Human Visual System." *Advanced Functional Materials* 32, 6, (2022): 2108014.

3. **Feng Guo**, Menglin Song, Man-Chung Wong, Ran Ding, Weng Fu Io, Sin-Yi Pang, Yuqian Zhao and Jianhua Hao. "A Brain-Inspired Artificial Neuron based on van der Waals Ferroelectric Semiconductor. " Submitted.

4. Menglin Song, Yongxin Lyu, **Feng Guo**, Sin-Yi Pang, Man-Chung Wong, and Jianhua Hao. "One-Step, DNA-Programmed, and Flash Synthesis of Anisotropic Noble Metal Nanostructures on MXene." *ACS Applied Materials & Interfaces* 13, 44 (2021): 52978-52986.

5. Ran Ding, Yongxin Lyu, Zehan Wu, **Feng Guo**, Weng Fu Io, Sin-Yi Pang, Yuqian Zhao, Jianfeng Mao, Man-Chung Wong, and Jianhua Hao. "Effective Piezo-Phototronic Enhancement of Flexible Photodetectors Based on 2D Hybrid Perovskite Ferroelectric Single-Crystalline Thin-Films." *Advanced Materials* 33, 32 (2021): 2101263.

6. Beining Zheng, Zehan Wu, **Feng Guo**, Ran Ding, Jianfeng Mao, Maohai Xie, Shu Ping Lau, and Jianhua Hao. "Large-Area Tellurium/Germanium Heterostructure Grown by Molecular Beam Epitaxy for High-Performance Self-Powered Photodetector." *Advanced Optical Materials* 9, 20 (2021): 2101052.

7. Yuqian Zhao, **Feng Guo**, Ran Ding, Weng Fu Io, Sin-Yi Pang, Wenzhuo Wu, and Jianhua Hao. "Piezo-Phototronic Effect in 2D α-In_2Se_3/WSe_2 van der Waals Heterostructure for Photodetector with Enhanced Photoresponse." *Advanced Optical Materials* 9, 20 (2021): 2100864.

8. Menglin Song, Sin-Yi Pang, **Feng Guo**, Man-Chung Wong, and Jianhua Hao. "Fluoride-Free 2D Niobium Carbide MXenes as Stable and Biocompatible Nanoplatforms for Electrochemical Biosensors with Ultrahigh Sensitivity." *Advanced Science* 7, 24 (2020): 2001546.

9. Ding Ran, Chun-Ki Liu, Zehan Wu, **Feng Guo**, Sin-Yi Pang, Lok Wing Wong, Weng Fu Io, Shuoguo Yuan, Man-Chung Wong, Michal Bartlomiej Jedrzejczyk, Jiong Zhao, Feng Yan, and Jianhua Hao. "A general wet transferring approach for diffusion-facilitated space-confined grown perovskite single-crystalline optoelectronic thin films." *Nano letters* 20, 4 (2020): 2747-2755.

Acknowledgements

Firstly, from the bottom of my heart I would like to express my thanks to my patient and supportive supervisor, Prof. Jianhua Hao for his invaluable advice, and continuous support at every stage during my PhD study. His extensive knowledge in this field has made the research an inspiring experience in my life. And his optimism and enthusiasm for research and life have always encouraged me in my academic career and daily life, especially when I feel confused. Without his help, this work would not have been possible.

Also, I am really grateful to Dr. Wong Hon Fai, Dr. Hardy Lui and Dr. Terence Wong for their assistance in equipment utilization in AP and UMF. And I sincerely appreciate the helpful suggestions and discussions from Prof. Wenzhuo Wu from Purdue University and previous group members including Dr. Gongxun Bai and Dr. Wenjing Jie.

I would like to express my great gratitude to all guys who ever helped me in the past three years, especially my research groupmates and friends. Thanks for the encouragement from Dr. Menglin Song and Dr. Man-Chung Wong, and many thanks to Ms. Yongxin Lyu for teaching me dry transfer, Dr. Ran Ding and Weng Fu Io for their help in PFM, Ms. Yuqian Zhao for the assistance in photolithograghy. And I also feel very fortunate to have received help from Ms. Sin Yi Pang, Dr. Shuoguo Yuan, Dr. Zehan Wu, Mr. Jianfeng Mao, Mr. Jedrzejczyk Michal Bartlomiej, Dr. Beining Zheng, Dr. Wei Xu, Ms. Fumei Yang, and Dr. Yu Sun.

Finally, I would like to express my deepest appreciation to my parents for their endless love and my girlfriend for her accompany.

Table of Contents

Abstract II

List of Publications IV

Acknowledgements VI

Table of Contents VII

List of Figures X

List of Tables XVII

Chapter 1 Introduction 1

1.1 Background of ferroelectricity and piezoelectricity 1

1.1.1 Basic concept 1

1.1.2 Conventional materials 6

1.1.3 2D materials 11

1.2 Strain engineering in 2D materials 16

1.2.1 Uniaxial strain effect 17

1.2.2 Piezoelectric biaxial strain effect 19

1.3 Overview of neuromorphic devices 21

1.3.1 Electrical synapse 22

1.3.2 Optoelectronic synapse 27

1.4 Significance of research 30

1.5 Structure of thesis 33

Chapter 2 Experimental Methods 35

2.1 Fabrication methods of 2D material 35

2.1.1 Exfoliation 35

2.1.2 Chemical vapor deposit growth 39

2.2 Fabrication methods of heterostructures 43
2.2.1 Direct CVD growth 44
2.2.2 Mechanical stacking 48
2.3 Characterizations 51
2.3.1 Structural analysis 51
2.3.2 Optical characterizations 53
2.3.3 Piezoresponse force microscopy 55
2.3.4 Electrical measurement 56
Chapter 3 Piezoelectric Biaxial Strain Effects on the 2D Ferroelectric α-In_2Se_3 Nanosheets 58
3.1 Introduction 58
3.2 Experimental 59
3.2.1 Design of measurement setup 59
3.2.2 Characteristics 61
3.3 Effect of biaxial strain on Raman spectra 62
3.4 Effect of biaxial strain on PL spectra 65
3.5 Strain induced piezoelectric field 67
3.6 Summary 71
Chapter 4 Brain-Inspired Artificial Neuron Based on 2D Ferroelectric Semiconductor 73
4.1 Introduction 73
4.2 Experimental 76
4.2.1 Device fabrication 76
4.2.2 Characterizations to verify ferroelectricity 77
4.3 Working principle 80
4.4 Perform logics in the device 82
4.4.1 linearly nonseparable logic 82
4.4.2 linearly separable logic 87
4.5 Synaptic behaviors 89

4.6 Artificial neural network....92
4.7 Emulation of controlling food intake....93
4.8 Summary....96
Chapter 5 Multifunctional Optoelectronic Synapse Based on 2D Ferroelectric Material....97
5.1 Introduction....97
5.2 Design of the device....100
5.2.1 Experimental methods....100
5.2.2 Structure of device and material characterization....101
5.3 Mimicking the behaviors of biological synapse....105
5.3.1 Emulation of optic nerve....105
5.3.2 Photonic synapse mimicking the retina....109
5.3.3 Emulation of Pavlov's dog experiment....113
5.4 Information storage....116
5.5 Information processing....119
5.6 Summary....124
Chapter 6 Conclusion and Future Prospect....126
6.1 Conclusion....126
6.2 Future prospect....128
References....130

List of Figures

Figure 1-1 A top-view atomic distribution of α-quartz 2

Figure 1-2 Unit cell under mechanical stress. 4

Figure 1-3 Polarization process of dielectric materials 4

Figure 1-4 Ferroelectric hysteresis 5

Figure 1-5 The relationships among piezoelectric, pyroelectric and ferroelectric materials 6

Figure 1-6 The ferroelectric hysteresis curve of Rochelle salt 7

Figure 1-7 ABO_3 cubic perovskite structure. 8

Figure 1-8 Chemical structure of PVDF 9

Figure 1-9 Top view and side-view of 2H-MoS_2 14

Figure 1-10 Apply strain by elongating the flexible substrate 17

Figure 1-11 Inducing strain in 2D materials by bending the substrate 19

Figure 1-12 (a) Schematic of strained thin film of STO:Ni on PMN-PT. (b) The setup for measuring the NIR emission under an external electric field. 21

Figure 1-13 Schematic diagram of a synapse 23

Figure 1-14 A schematic illustration of general mechanisms in memristor 24

Figure 1-15 Schematic diagram of ferroelectric thin-film transistor 27

Figure 2-1 Schematic diagram of the mechanical exfoliation process 35

Figure 2-2 A summary of the methods for exfoliating 2D materials 39

Figure 2-3 Schematic diagram of the furnace for MoS_2 growth on graphene 45

Figure 2-4 High-resolution cross-sectional TEM image of graphene/MoS_2 heterostructure 46

Figure 2-5 Schematic diagram of preparing lateral monolayer WSe_2-MoS_2 heterostructure **48**

Figure 2-6 Steps for preparing vertical 2D heterostructures by mechanical stacking **49**

Figure 2-7 TEM images of the transferred and electron-beam-deposited Au electrode on MoS_2 ..... **51**

Figure 2-8 Schematic diagram of TEM structure **52**

Figure 2-9 Schematic diagram of the PFM structure **55**

Figure 3-1 Schematic diagram of Raman and PL measurements via an electromechanical device **60**

Figure 3-2 AFM image of α-In_2Se_3 nanosheets **61**

Figure 3-3 The Raman peak position as a function of the applied voltage from 0 to 500 V and inset shows the Raman spectrum of α-In_2Se_3 ..... **62**

Figure 3-4 The Raman peak as a function of the applied voltage from 0 to -500 V. **63**

Figure 3-5 PL spectra under various applied voltages from (a) 0 V to 500 V and (b) 0 V to -500 V with 0.1 mW laser power. The inset shows the PL peak position as a function of applied voltage from -500 V to 500 V. **66**

Figure 3-6 PL spectra under various laser powers (a) before polarization, (b) 0 V after polarization, and (c) 500 V after polarization **68**

Figure 3-7 PL peak position as a function of laser power at various applied voltages **69**

Figure 3-8 Schematic energy band structure under piezoelectric fields and laser powers **71**

Figure 4-1 Schematic diagram of the device structure **.....77**

Figure 4-2 a) Raman spectrum of α-In_2Se_3, the peaks are located at 88, 104, 180 and 193 cm^{-1}, respectively. b) Top-view high-resolution TEM of the α-In_2Se_3 nanosheet with 3R structure in this work, which shows its hexagonal symmetry. c) PL spectra of α-In_2Se_3 nanosheet on Si/SiO_2 substrate under 532 nm laser are measured. The peak location of 880 nm indicates the semiconductor nature of the material. d) The crystal structure of α-In_2Se_3 with rhombohedral (3R) stacking mode. The ferroelectricity can be attributed to the central Se atom's lateral movement**. 78**

Figure 4-3 a) The topographic, OOP and IP PFM phase images are used to verify the ferroelectricity of the material. b) PFM phase and PFM amplitude hysteresis loops of α-In_2Se_3 on a conductive substrate indicate its domain can be reversed under external electric field **.....79**

Figure 4-4 a) *I-V* hysteresis curves under V_{DS} sweep of 2 V, 4 V and 6 V due to the IP ferroelectricity. b) The transfer curve of transistor, the clockwise hysteresis loop is induced by OOP ferroelectricity **.....80**

Figure 4-5 The working mechanism of artificial neuron based on ferroelectric 2D α-In_2Se_3. a) After applying positive voltage, the channel is in a state of ferroelectric polarization upward and low conductance, b) The corresponding energy band diagram. c) After applying negative voltage, polarization direction is switched, the channel shows high conductance, and d) Energy band at the interface bends downward **.....82**

Figure 4-6 Schematic diagram of neocortical pyramidal neurons in brain**.....83**

Figure 4-7 Working mechanism of Perceptron**.....84**

Figure 4-8 Logic gates of AND, XOR, OR and NOT **85**

Figure 4-9 a) Demonstration of 10 cycles to execute the XOR logic. In top panel, the drain voltage represents the input, and the drain current represents the output in lower panel. b) The fifth cycle is chosen as an example to demonstrate the details **87**

Figure 4-10 The two panels on the left represent the input IN1 and IN2. The panel on the right depicts that the device can perform OR logic under illumination, while in the dark the device is switched to AND mode **88**

Figure 4-11 The gate voltage is defined as the input and the V_{DS} is used to read the output (I_{DS}) to demonstrate the NOT logic.....**88**

Figure 4-12 a) A schematic diagram of three-terminal biological synapse. b) The side-view of device structure.....**90**

Figure 4-13 a) The PSC triggered by 10, 20 and 30 consecutive V_{DS} electrical pulses (5 V, 270 ms), a 2 V voltage is set as bias. b) Long-term potentiation and depression are obtained by applying 50 consecutive 6 V and -3 V electrical pulses at the source and drain electrodes, respectively **91**

Figure 4-14 The PSC triggered by 10 gate electrical pulses from 2 V to 10 V and -2 V to -10 V, V_{DS} is set to 2 V **92**

Figure 4-15 a) The principle of crossbar based on our device, where the conductance of the channel is defined as the weight of the synapses. b) A three-layer ANN is built for image recognition based on our proposed device. Accuracy rate of c) small digit image and d) MNIST digit image as a function of training epoch.**93**

Figure 4-16 Emulation of controlling food intake. The variation of the drain current is observed after 10 electrical pulses of 6 V applied under different gate bias

voltages a) -5 V, b) -2 V, c) 2 V, d) 5 V, e) 10 V. f) A diagram to illustrate the principle of controlling food intake in the brain to maintain energy homeostasis **.....95**

Figure 5-1 a) Schematic of entire biological visual system. b) The structure of proposed multifunctional optoelectronic synaptic device **.....102**

Figure 5-2 a) Two different stacking modes of ferroelectric α-In_2Se_3: rhombohedral (3R) structure and hexagonal (2H). b) TEM of a side-view α-In_2Se_3 nanosheet **.....103**

Figure 5-3 a) Topography, OOP PFM phase and OOP PFM amplitude images show opposite domain orientation (arrow location), scale bar is 500 nm. b) PFM phase and PFM amplitude hysteresis loops of α-In_2Se_3 on Pt substrate indicate the switchable ferroelectric nature under external voltage **.....104**

Figure 5-4 PL spectra of a) α-In_2Se_3 and b) GaSe under 532 nm laser **.....105**

Figure 5-5 a) Schematic of optic nerve and b) A side-view diagram of the OES device **.....106**

Figure 5-6 PPF index as a function of electrical pulse interval time Δt, the fitting curve shows that PPF decreases exponentially with the increase of Δt. The inset displays PSC triggered by two consecutive electrical pulses; A is defined as the amplitudes of PSC **.....107**

Figure 5-7 LTP and LTD operations under 1 V (175 ms) as well as -3 V (175 ms) 20 applied pulses, respectively **.....108**

Figure 5-8 a) Nonlinearity (NL), cycle to cycle variation (cyc) and symmetry of LTP and LTD under different cases: case1(1 V, -3 V), case2 (2 V, -4 V), case3 (3 V,

-5 V). b) LTP and LTD operations under 3 V (175 ms) as well as -3 V (175 ms) 100 applied pulses, respectively **109**

Figure 5-9 a) Working mechanism of the retina. b) Schematic of OES device under light pulses to mimics the retina **110**

Figure 5-10 a) The PSCs triggered by a pair of light pulses (808 nm wavelength, 7.8 mW cm^{-2}, width 1 s) with Δt=0.5 s. b) PPF index as a function of light pulse interval time Δt **111**

Figure 5-11 The PSC triggered by 5, 10 and 20 consecutive light pulses (808 nm wavelength, 5.7 mW cm^{-2}, 1 s) **112**

Figure 5-12 The different responses of PSC under 10 light pulses (5.7 mW cm^{-2}, 1 s) with a) 450 nm, b) 808 nm and c) 980 nm wavelength, respectively and related diagram of band structure d-f). **113**

Figure 5-13 Pavlov's dog experiments to associate electrical and light stimuli together. a) 20 electrical pulses were applied, the PSC was below threshold of 7 nA (no response). b) A PSC of 10 nA was in response to a light pulse (18.7 mW cm^{-2}, width 7 s, 450 nm wavelength) (salivation). c) In order to couple different stimuli, the coincidence stimuli consist of electrical and light pulses were imposed on device. d) After training, electrical pulses alone can induce above-threshold PSCs. A forgetting behavior was observed with increasing time... **115**

Figure 5-14 *I-V* hysteresis curves under sweep from 2 V to 6 V **116**

Figure 5-15 The *I-V* curve where the currents of stage 1 and 3 in hysteresis loop are smaller than those of stage 2 and 4 ..... **118**

Figure 5-16 a) *I-V* curve under ferroelectric polarization orientation shown in inset. b) Photoresponse at zero bias voltage under 50 light pulses (18.7 mW cm^{-2}, 0.1

Hz, 450 nm wavelength) and the ferroelectric polarization orientation in a). c) The *I-V* curve after a positive voltage applied, and d) corresponding photoresponse **119**

Figure 5-17 The "AND" logic function of device under light and electrical pulses **120**

Figure 5-18 a) The *I-V* hysteresis curves of ferroelectric α-In_2Se_3/GaSe vdW heterostructure. Photoresponse at zero bias voltage when the polarization orientations of two parts of channels are b) the same or c) opposite. The orientation of polarization is indicated by the arrows **122**

Figure 5-19 The basic principle of crossbar **122**

Figure 5-20 a) An ANN built to perform XOR logic. b) Accuracy rate as a function of training number **124**

List of Tables

Table 1. Comparison of inducing strain on material phonon……..**65**

Table 2. Effect of strain on the PL shift……...**66**

Chapter 1 Introduction

Due to the asymmetry of the unit cell of piezoelectric materials, the accumulated charge can be observed on the surface of the material under external stress, which is known as the piezoelectric effect. The phenomenon is an advantageous tool to modulate the properties of the material and is of great benefit to improve the performance of the devices. As a special piezoelectric material, ferroelectric materials with spontaneous polarization can not only respond to the applied pressure, its polarization direction also can be reversed under the external electric field. Therefore, since the discovery of ferroelectric materials, its unique properties have attracted extensive research interest and have been widely studied in the fields of memory, field-effect transistors (FET), photovoltaic cells, and so on.[1-3] With the growing demand for miniaturization in devices and the continuous development of neuromorphic computing, two-dimensional (2D) ferroelectric materials show great advantages to improve device performance and multifunctionalize devices.

1.1 Background of ferroelectricity and piezoelectricity

1.1.1 Basic concept

When an external force is applied to a piezoelectric material, accumulated charges appear on its certain surfaces due to deformation, which is known as the piezoelectric effect. The piezoelectric effect was first discovered by brothers Cuire in 1880.[4] Due to the excellent performance and stability, α-quartz crystals as a

representative of piezoelectric materials are still widely utilized in piezoelectric devices until today. Therefore, here, the piezoelectric effect in α-quartz is chosen as an example to illustrate this unique phenomenon.

Based on symmetry, all crystals can be classified into 32 point groups and 7 crystal systems.[5] The α-quartz possesses one axis of threefold symmetry and three axes of twofold symmetry, therefore, it is categorized as three-two point group of the trigonal crystal system. In general, the threefold rotational axis of α-quartz is defined as the Z-axis, while the twofold rotational axis is considered as the X-axis and the third direction is the Y-axis. The Figure 1-1 shows a top-view atomic distribution. The oxygen atom is extremely electronegative, so the silicon atom exhibits a positive charge while the oxygen atom is negatively charged. It can be seen from the figure，the center of the positive charge is located in the center of the triangle formed by silicon atoms, while the center of the negative charge is located in the center of the triangle composed of oxygen atoms. For α-quartz, in the absence of applied forces, its positive charge center coincides with the negative charge center.

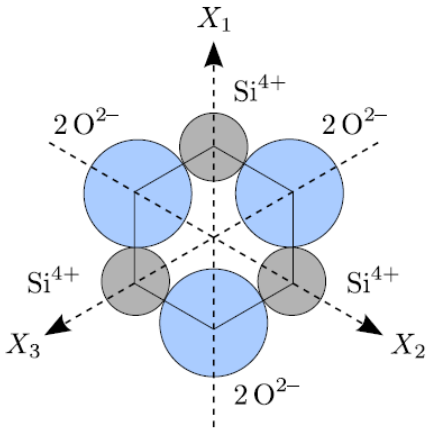

Figure 1-1 A top-view atomic distribution of α-quartz[5]

However, the external force will cause a distortion in the unit cell structure, the positive and negative charge centers of the unit cell will move as shown in Figure 1-2, where the positive and negative charge centers no longer coincide. From a macroscopic view, the accumulated charges will be observed on the surface of the material, which is known as direct piezoelectric effect. P is generally introduced to describe the macroscopic polarizing state in the material, which represents macroscopic polarization vector per unit volume according to Equation 1-1. Under mechanical force, the relationship between P and stress σ is shown in Equation 1-2, where d is the piezoelectric coefficient. In contrast, when an applied electric field (E) is imposed on the piezoelectric materials, mechanical deformation (S) is generated in certain directions of the material, which is defined as the inverse piezoelectric effect as shown in Equation 1-3.[6]

$$P = \lim_{\Delta V \to 0} \frac{\sum_{\Delta V} P_{micro}}{\Delta V} \tag{1-1}$$

$$P = d\,\sigma \tag{1-2}$$

$$S = d_t\,E \tag{1-3}$$

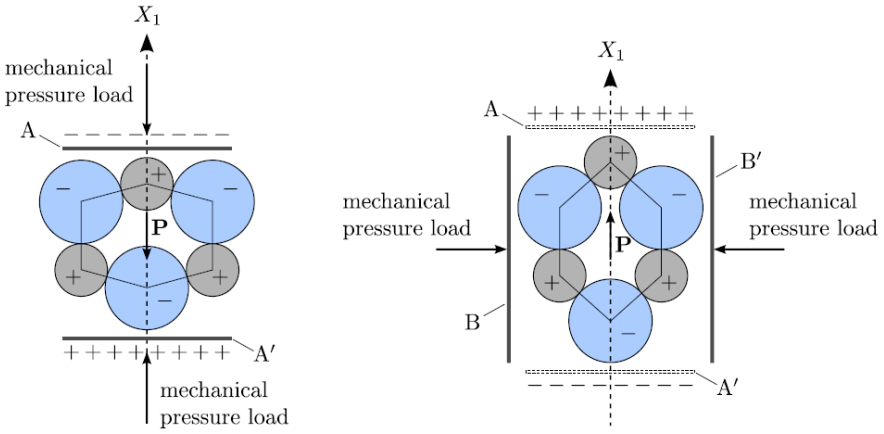

Figure 1-2 Unit cell under mechanical stress[5]

In contrast to conductors and semiconductors, there are no free carriers in an ideal dielectric material. Under the external electric field, the positive and negative charge centers of the non-polar molecules in the dielectric material are separated, which result in the formation of dipoles. Due to driven by the imposed electric field, the dipole tends to be aligned along the direction of the external electric field, the phenomenon is called polarization of the dielectric. Simultaneously, a large amount of so-called polarization charges can be observed on the surface of the dielectric material. When the applied electric field is removed, the positive and negative charge centers of the molecules are coincident again and the polarization of the dielectric material will disappear. The generation process of dipoles in dielectric materials and the influence of the external electric field on the dipole alignment are shown in Figure 1-3.[7]

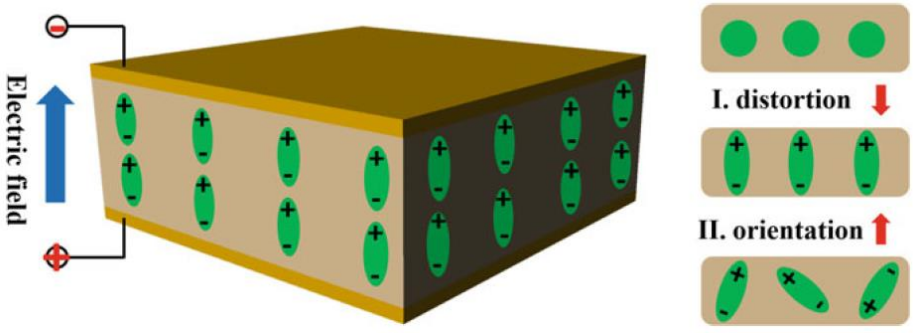

Figure 1-3 Polarization process of dielectric materials[7]

However, as a special type of dielectric material, ferroelectric materials with spontaneous polarization can remain in the polarized state even after the applied electric field is removed. There are many small areas inside the ferroelectric material,

and their internal polarization directions are the same, but the polarization directions between each area are different. These small regions are denominated as ferroelectric domains, and the boundaries between the domains are called domain walls. Because of the randomly oriented domain, no polarization charge can be observed on the surface of ferroelectric materials in the absence of an external electric field. When an external electric field is gradually applied to the ferroelectric material, the polarization directions of the domains are aligned, the dependence of polarization P on electric field E is shown in Figure 1-4.[8] The saturation polarization (Ps) means the maximum polarization that the material can achieve. And the remnant polarization (Pr) represents the remaining polarization in the material when the external electric field is removed, which is an important parameter for characterizing the ferroelectricity of the material. In addition, the coercive field (Ec) as a special electric field value plays a role in minimizing the polarization of ferroelectric materials to zero. Thus, with the variation of the applied electric field, a ferroelectric hysteresis loop (P-E loop) can be obtained.[9]

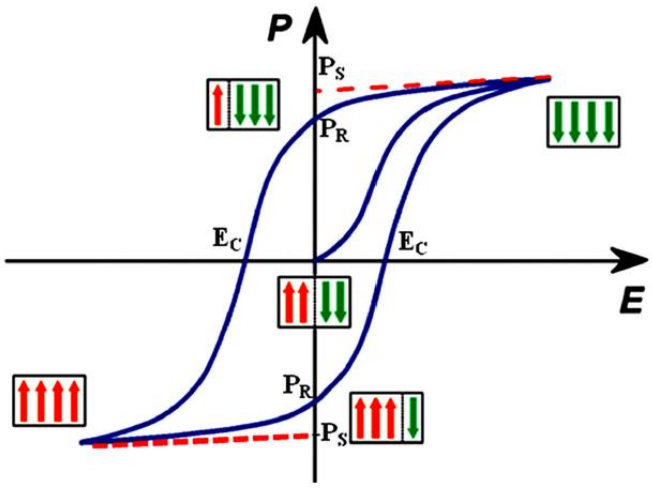

Figure 1-4 Ferroelectric hysteresis[8]

Due to the non-centro-symmetric property, the piezoelectric material generates an electrical potential at the surface as a response to the applied force on it. As a subgroup of piezoelectric materials, some materials possess a special polar axis which can be spontaneously polarized and an electrical potential can be obtained with changes in temperature, the phenomenon is called pyroelectricity. Ferroelectric materials are a subgroup of pyroelectrics, thus, piezoelectric and pyroelectric effects can also be observed in ferroelectric materials,[10] the relationship among them is as shown in Figure 1-5.

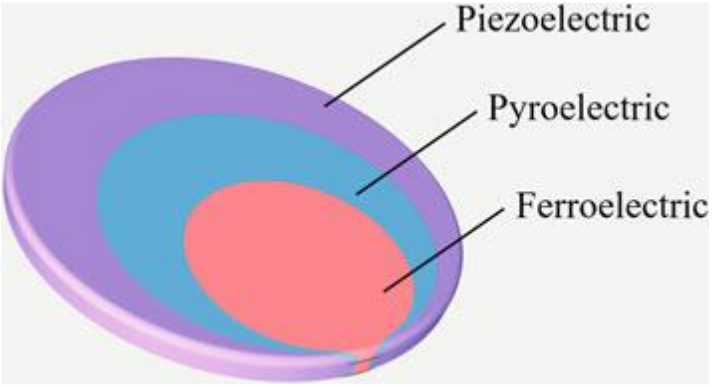

Figure 1-5 The relationships among piezoelectric, pyroelectric and ferroelectric materials[10]

1.1.2 Conventional materials

Although pyroelectric effects have been discovered in ancient times, the time for investigating ferroelectric and piezoelectric effects is not very long, especially the discovery of ferroelectric is only one hundred years. Rochelle salt (potassium sodium tartrate tetrahydrate, $KNaC_4H_4O_6 \cdot 4H_2O$) was first successfully prepared by Pier Seignette from La Rochelle France, in 1672, and the compound played an

important role in the history of ferroelectric and piezoelectric developments. In 1880, brothers Pierre and Paul-Jacques Curie discovered piezoelectricity in Rochelle salt and identified a series of other piezoelectric crystals, the classical work demonstrated that piezoelectricity in Rochelle salt is far more active than α-quartz. However, it took another forty years until its ferroelectricity was discovered. From 1919, Joseph Valasek as a master candidate under the supervision of Prof. W. F. G. Swann conducted a systematic study of electrical properties of Rochelle salt and analogized it to the magnetic properties of ferromagnetics. Later, he presented the results of his research at the meeting of the American Physical Society, although the term "ferroelectricity" had not yet been adopted, the key feature of ferroelectricity was pointed out by him, namely "permanent polarisation is the natural state". In addition, he also presented the first hysteresis curve of a ferroelectric material at the conference as shown in Figure 1-6.[11]

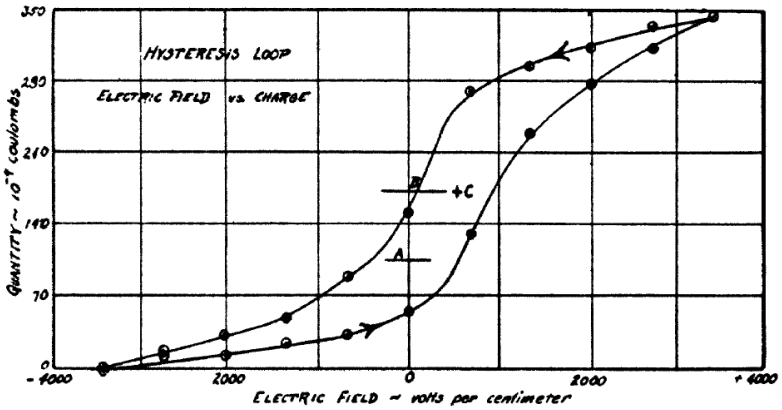

Figure 1-6 The ferroelectric hysteresis curve of Rochelle salt[11]

For a while, it did not attract much research interest, primarily for the reason that the Rochelle salt was the only crystal in which ferroelectricity could be observed at that time, and even a slight deviation in the complex chemical composition would

lead to the disappearance of the phenomenon. The breakthrough came in the 1940s when the first man-made, structurally simple ferroelectric material barium titanate ($BaTiO_3$) was discovered, and a series of piezoelectric devices based on it were investigated. The Figure 1-7 depicts a schematic diagram of ABO_3 perovskite structure. [12] Since then, a large number of ferroelectric materials in perovskite crystal structure with excellent properties have been synthesized, among them the most notable one is lead zirconate titanate (PZT) which is first reported by G. Shirane in 1952.[13] Despite the environmental concerns caused by the lead element in it, PZT is still one of the most widely used ferroelectric materials so far, and the search for a lead-free alternative is a popular research topic at present.

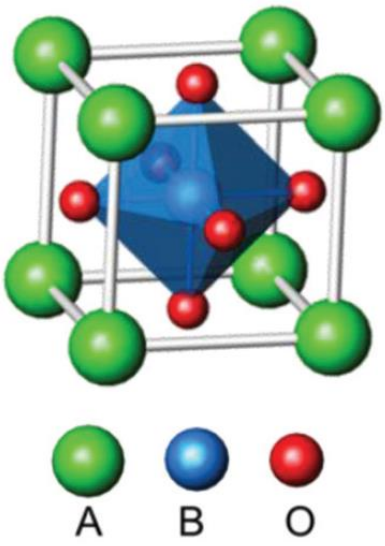

Figure 1-7 ABO_3 cubic perovskite structure[12]

In addition to the rigid and fragile inorganic ferroelectric materials, the piezoelectricity in organic polymer ferroelectric polyvinylidene fluoride (PVDF) was reported by Kawai in 1969.[14] The structure of PVDF is as shown in Figure 1-8, which shows the molecular repeat unit (CH_2–CF_2).[15] The polymers is highly

stretchable, bio-compatible, and capable of self-healing which provide the opportunities for flexible ferroelectric and piezoelectric devices.

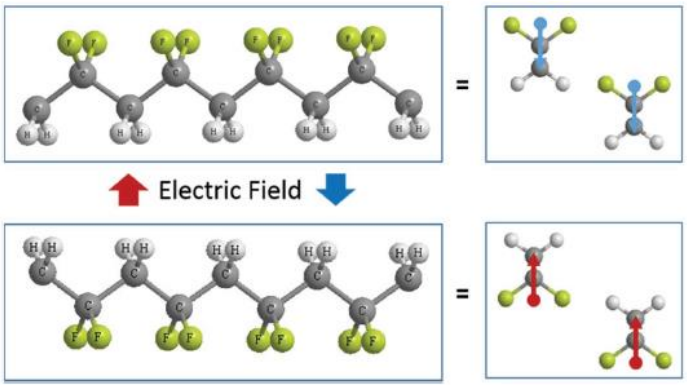

Figure 1-8 Chemical structure of PVDF[15]

For a long time, ferroelectrics were just an interesting academic topic, and it was until World War II that ferroelectric materials began to be used as sonar to detect submarines. Subsequently, other applications such as high capacitance, photovoltaic cells, etc. have been extensively studied. Due to its unique spontaneous polarization properties, ferroelectric materials also attract great research interest in the field of electronic devices. In 1997, S. Mathews et al. reported a novel ferroelectric field-effect transistor (FET) which offers the possibility for ferroelectric nonvolatile memory devices. In their work, semiconducting $La_{0.7}Ca_{0.3}MnO_3$ was used as a channel whose doped rare-earth manganates exhibited colossal magnetoresistive properties, and $PbZr_{0.2}Ti_{0.8}O_3$ was selected as ferroelectric top gate. The device demonstrates a tunable channel conductance of at least a factor of 3 and retention on the order of hours.[16] In addition, ferroelectric tunnel junction (FTJ) throw light on the way for breaking the current bottleneck of low speed and high energy consumption of silicon-based electronic devices. Recently, Ma et al. reported a high-

performance ferroelectric tunnel junction based on a $Ag/BaTiO_3/Nb:SrTiO_3$ whose operation speed can reach up to 600 ps, and synaptic behavior such as spike-timing dependent plasticity was achieved.[17]

In addition to the conventional ferroelectric materials, semiconducting piezoelectric materials with wide band gap, such as ZnO, GaN and CdS, are more suitable as active layers and have been significantly developed in the field of electronic devices. Utilizing the piezoelectricity of materials to modulate the electrical properties of devices was first proposed by Zhonglin Wang. In 2006, his team measured the electrical transport properties of a long ZnO nanowire in the bending state. A decreasing conductance was observed with the continuous bending of the nanowire, and the results indicated that the piezoelectric potential generated in the ZnO under external forces was able to affect the carrier transport.[18] The following year, the term "piezotronics" was created by him. Besides, the piezoelectric potential can also play a role in promoting the separation of photogenerated carriers, thus improving the performance of optoelectronic devices, and a series of research have been conducted. In 2010, Wang et al. proposed a photodetector with metal−semiconductor−metal ZnO micro-/nanowire structure, and the piezoelectric effect on the responsivity was investigated. Their results showed that piezo-phototronic effects can increase detection sensitivity by more than 5 times for pW levels of light detection.[19] Thus ferroelectricity and piezoelectricity have great potential in applications for improving the performance of electronic and optoelectronic devices, and provide inspiration for multifunctionalized devices.

1.1.3 2D materials

2D material refers to the material whose one dimension is restricted. Nanomaterials have been a popular research topic in materials discipline for a long time, and many novel phenomena are found in these materials due to the restriction of one or several dimensions. For a material, the different number of restricted dimensions not only affects the morphology, but also determines its properties, such as 0D fullerenes, 1D nanotubes, 2D graphene and 3D graphite are all composed of carbon. Before 2D materials, one-dimensional materials and zero-dimensional materials have been well explored, such as quantum confinement in semiconductor quantum dots and so on.[20-22] Although their bulks have been discovered for many years such as graphite and MoS_2, they did not attract much attention for a long time due to the difficulty of preparing their 2D single-atomic layer counterparts until the discovery of graphene with atomic-level thickness.

Graphene was the first 2D material with a single atomic layer to be successfully prepared, and although many previous efforts have been made, only multilayer graphene was obtained. Andre Geim's group in 2004 reported a simple method to prepare graphene by repeated mechanical exfoliation using tapes.[23] Despite the method cannot prepare large-area graphene for the purpose of application, it will provide a good platform for physical research. Inspired by the discovery of graphene, a series of 2D materials have emerged including transition metal dichalcogenides (TMDs),[24] h-BN,[25] MXenes[26] and so on. More importantly, as a big family, 2D materials cover metals, semiconductors and insulators, which provides the

possibility to fabricate electronic devices and optoelectronic devices based on 2D materials to break Moore's law.

Because electrical potential can be generated under applied stress and an applied electric field can also induce deformation in the material, piezoelectric properties are highly desired for flexible electronic devices such as sensors or nanogenerators. But the conventional oxide dominant piezoelectric materials are not suitable for flexible devices due to their brittleness. Although organic ferroelectric materials can be stretched, they also suffer from the critical thickness problem, for example, there is no ferroelectricity and piezoelectricity in PVDF with the thickness below 100 nm.[27]

The 2D piezoelectric material becomes intriguing due to its robust electromechanical response even in single-atom thickness, which is promising for flexible nanoelectronics and optoelectronics for energy harvesting, health monitoring, etc.[28, 29] In addition, 2D piezoelectric materials also provide a favorable platform for studying piezoelectric phenomena in ultrathin materials. Due to the opposite orientation in the two adjacent layers, the bulk MoS_2 does not exhibit piezoelectric properties, but according to predictions, piezoelectricity can be obtained in monolayers and thin odd layers of MoS_2. In 2014, the first experimental results on the piezoelectric properties in monolayer MoS_2 were reported by Wu et al. The piezoelectric voltage and current output were observed in odd-layer materials in the case of periodic external stresses, which was not obtained in even-layer. The peak output of a single monolayer flake under 0.53% strain can reach up to 15 mV and 20 pA, and a device based on piezotronics was demonstrated.[30] In the following year,

Zhang's group also reported obtaining piezoelectricity in a free-standing single layer of MoS_2, and the piezoelectric coefficient was measured to be 2.9×10^{-10} C m^{-1}.[31] Subsequently, a series of TMDs materials were identified as piezoelectric. The structure of TMDs is shown in the Figure 1-9. From the top view, the distribution of atoms is similar to that of quartz, so that an intrinsic in-plane piezoelectricity can be observed. From the side view, the metal atom is sandwiched between two S atoms, and the symmetric structure leads to there is no piezoelectric effect in the vertical direction.[32]

In addition to TMDs (including MoS_2, $MoSe_2$, WS_2 and so on),[33-36] h-BN, and graphene nitride have also been confirmed experimentally to be the intrinsic in-plane piezoelectricity. 2D boron nitride (BN) with a stable planar hexagonal structure is one of the few insulators in the 2D material family. Theoretically, the piezoelectric coefficient of h-BN is predicted to range from 118 to 139 pC/m.[37-39] The optical second-harmonic generation (SHG) reveals its non-centrosymmetric structure, which indirectly confirms the existence of piezoelectricity in h-BN.[40] 2D graphene nitride (g-C_3N_4) is a semiconductor with wide band gap that is often used in photocatalysis. Unlike TMDs, robust in-plane piezoelectricity can still be observed in its multilayers and even in the bulk material, which is primarily attributed to the unusual stacking mode.[41]

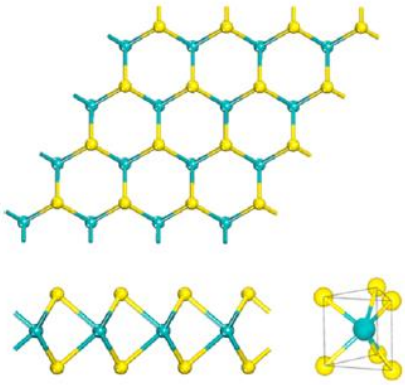

Figure 1-9 Top view and side-view of 2H-MoS_2[32]

Excluding ferroelectric materials, there is no intrinsic out-of-plane piezoelectricity discovered in 2D materials. Due to the atomic-level thickness, the decorated surface has a significant impact on the properties of the material, and therefore a great deal of effort has been made to modify the surface of the material in order to introduce new properties. In 2014, Mohammad et al. predicted that the adsorption of hydrogen and/or fluorine atoms on the surface of h-BN would lead to an out-of-plane dipole moment and the piezoelectric response could be comparable to that of conventional 3D piezoelectric materials.[42] Lu et al. reported in 2017 a method for synthesizing Janus monolayers of TMDs by substituting Se atoms for S atoms in the top-layer, which breaks the out-of-plane symmetry of TMDs and the out-of-plane piezoelectricity is directly confirmed by second harmonic generation and piezoresponse force microscopy.[43]

Ultra-thin ferroelectric materials have great potential for applications in the field of electronic devices, therefore a great deal of effort has been made to solve the critical thickness problem of conventional oxide dominated ferroelectric materials. Currently, numerous experiments have shown that ferroelectricity can still be

observed in conventional ferroelectric materials with thicknesses of a few nanometers, such as $BaTiO_3$ down to 2.4 nm.[44] However, ferroelectricity in conventional ferroelectric materials is greatly affected by lattice mismatch, thus there is a very high requirement for substrates. In recent years, ferroelectric HfO_2 thin films have attracted a lot of research interest because of its robust ferroelectric properties as well as compatibility with silicon-based semiconductor technologies. In 2020, Suraj et al. reported a method to prepare ferroelectric HfO_2 films using atomic layer deposition, and more importantly, ferroelectricity can still be observed at a thickness of one nanometer.[45]

Compared to the oxide ferroelectric materials mentioned above, the 2D layered van der Waals (vdW) ferroelectric materials have many unique advantages, such as free of dangling bonds, tunable band structure, and more flexibility. Although a large number of 2D materials are predicted to be ferroelectric, only a few have been experimentally confirmed so far, including α-In_2Se_3, $CuInP_2S_6$, SnTe, d1T-$MoTe_2$, and WTe_2. It is interesting to note that the few 2D ferroelectric materials cover metals, semiconductors and insulators. In 2018, Fei et al. reported that ferroelectricity was observed in the topological semimetal WTe_2, which showed that a sufficiently thin polar metal can be permeated by an external electric field and the polarity can also be reversed. The ferroelectricity at room temperature in the semiconducting $MoTe_2$ with distorted 1T phase was confirmed by Yuan et al., and $MoTe_2$-based vdW heterostructures are capable of achieving high ON/OFF resistance ratios.[46] In 2016, the in-plane spontaneous polarization of tin telluride (SnTe) of 1 unit cell limit is reported by Chang et al., the works may lead to a wide variety of applications.[47] The

insulating ferroelectric 2D $CuInP_2S_6$ (CIPS) was first reported by Liu et al, whose transition temperature can be up to 320 K. The excellent insulating properties are particularly suitable for application in ferroelectric field-effect transistors.[48]

Among these 2D ferroelectric materials, currently the most reports and research available are about α-In_2Se_3. This is attributed to its stable ferroelectricity even in monolayer at room temperature, as well as the nature of the semiconductor with bandgap ~1.4eV which means the absorption of visible and near-infrared light. In 2017, Zhu's team successfully predicted the in-plane and out-of-plane ferroelectricity in α-In_2Se_3. Subsequently, several reports of experiments confirmed this prediction. In the same year, out-of-plane piezoelectricity and ferroelectricity in α-In_2Se_3 nanosheets was reported by Zhou et al.[49] In the following year, Li's team reported that interrelated out-of-plane and in-plane polarization were observed.[50] Due to its unique in-plane and out-of-plane ferroelectricity, α-In_2Se_3 shows great potential for applications in electronic devices as well as optoelectronic devices.

1.2 Strain engineering in 2D materials

Strain engineering is an effective strategy to modify the electronic structure of a material to affect its many properties such as optical and electrical characteristics. Also, strain engineering provides a way to extend the application of materials in flexible electronic devices and optoelectronic devices as well as improve their performance. The study of the effects of strain engineering has been carried out for decades, for example, strain is confirmed to play a significant role in enhancing the carrier mobility of silicon. However, conventional semiconductors can only

withstand a limited level of strain, which greatly limits the application of strain engineering. In contrast to conventional semiconductor materials, 2D materials can withstand extreme loads even at atomic level thickness.

1.2.1 Uniaxial strain effect

Uniaxial strain can be effectively imposed on the 2D material through the deformation of the flexible substrate under external forces. Currently, a wide variety of flexible substrates are available, such as PMDS, PET, PI, etc. In general, there are two methods that can cause deformation of the flexible substrate, one is to elongate it and the other is to bend it.

As shown in the Figure 1-10, after the 2D material is placed on the flexible substrate, a tensile force is applied to the substrate in one of horizontal directions, and the uniaxial strain can be effectively transferred to the 2D nanosheet due to friction and the adhesion between the 2D material and the substrate.[51] In the early research of strain engineering on 2D materials, this approach provided an advantageous tool to modulate the physical properties of the materials.

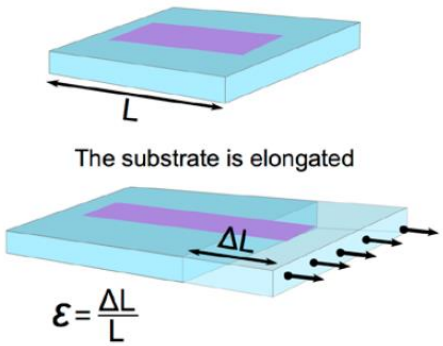

Figure 1-10 Apply strain by elongating the flexible substrate[51]

Graphene offers a promising future for electronics due to its unique and excellent physical properties, but before it can be applied, one problem has to be solved that is how to open its energy band gap at K point in the Brillouin zone. In 2008, Ni et al. successfully applied 0.8% uniaxial tensile stress to graphene by elongating a flexible substrate. The elongated carbon-carbon bonds lead to the redshift of the Raman peaks. Their results show that the energy band of graphene can be opened by strain and provide an efficient way to dynamically tune the electronic structure of graphene.[52] A similar experiment was also performed in WS_2, and a direct-indirect bandgap transition was obtained at 2.5% uniaxial strain when the flexible substrate was elongated. The density-functional-theory calculations further confirm this result.[53]

Bending substrates is another more widely used method to induce strain in 2D materials. As shown in the Figure 1-11,[51] when an external force is applied to a rectangular flexible substrate, a tensile strain along the direction of the force will be generated on the upper surface, and an opposite compressive strain will appear on the lower surface. The method is not only used to modulate the physical properties of materials, but also widely applied in flexible electronic and optoelectronic devices to improve their performance.

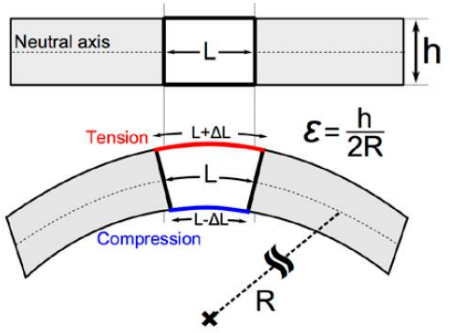

Figure 1-11 Inducing strain in 2D materials by bending the substrate[51]

Uniaxial strain provides a favorable tool for improving the performance of flexible devices based on 2D materials, especially for piezophototronics. In 2016, Wu et al. reported a strain-gated flexible optoelectronic device based on piezoelectric 2D MoS_2, where the piezoelectric potential induced by the strain promotes the separation of photogenerated carriers and greatly improves the photoresponse of the device.[54] In addition to photodetectors, solar cells based on 2D materials have also been investigated theoretically based on single-layer MoS_2 metal-semiconductor contacts. This work demonstrates that piezophototronic effects can increase the open-circuit voltage of solar cells, and also provides theoretical guidance for the design of related devices.[55]

1.2.2 Piezoelectric biaxial strain effect

Applying a voltage to a piezoelectric substrate provides a more precise and controlled method of inducing strain than bending a flexible substrate by mechanical means. When the external electric field is applied in the Z-axis direction, the piezoelectric biaxial deformation will be generated in the X-Y plane based on the inverse piezoelectric effect. Due to the large piezoelectric coefficient, PMN-PT is often selected as a substrate.

In 2007, the effect of the reversible biaxial strain induced by PMN-PT on epitaxial ferromagnetic films $La_{0.7}A_{0.3}MnO_3$ was investigated by Thiele et al. The strain causes a 19 K shift in the Curie temperature of the ferromagnetic film, and the

working mechanism has also been quantitatively analyzed. The effective magnetoelectric coupling coefficient up to 6×10^{-8} s m^{-1} is achieved due to the variation of M caused by strain. Their results show the ability of electrical control in a permanent magnet by piezoelectric biaxial stress.[56]

In addition to ferromagnetic thin films, controlled strain by electric field also shows great promise in modulating luminescence. Zhang et al. in 2012 reported an electric-field-controllable luminescence of ZnS:Mn/PMN-PT system, whose light emission originated from the piezoelectric potential in the epitaxial film caused by the deformation of substrate.[57] Unlike traditional mechanisms of light-emitting diodes, their work proposes a new strategy to modulate the luminescence. Subsequently, Bai et al. reported a tunable near-infrared luminescence of Ni^{2+} doped $SrTiO_3$ (STO:Ni) thin film on a PMN-PT substrate. The emission wavelength and bandwidth are tuned by varying the thickness of the film, which can be attributed to the effect of the strain in the film on the crystal field. Moreover, dynamic modulation of the strain in the thin film is achieved by the inverse piezoelectric effect of the piezoelectric substrate under an external electric field, as shown in Figure 1-12.[58] A similar result was also obtained by Wu et al. in upconversion photoluminescence of $BaTiO_3$:Yb/Er thin films on piezoelectric PMN-PT substrates.[59]

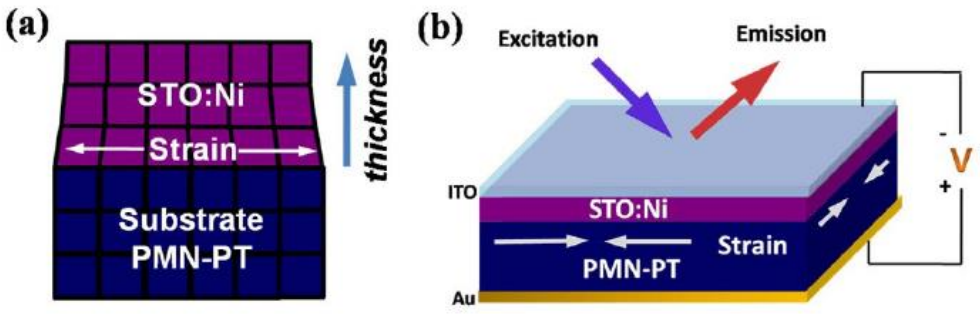

Figure 1-12 (a) Schematic of strained thin film of STO:Ni on PMN-PT. (b) The setup for measuring the NIR emission under an external electric field[58]

For 2D materials, biaxial strains generated by piezoelectric PMN-PT substrates also exhibit an extreme ability to modulate their physical properties. Compared to other methods of applying strain whose tunability of the band gap is within 100 meV per 1% strain, a blue shift of 300 meV per 1% strain is achieved by inducing biaxial strain, and an enhanced PL intensity is observed.[60] Besides, the effect of controlled biaxial strain on monolayer graphene was reported by Jie et al. The Raman spectra of graphene exhibit reversible and real-time manners and the physical mechanism about the variation of Raman is discussed.[61] The exceptionally high tunability of strain in the electronic structure of 2D materials promises a wide range of applications in the dynamic tuning of nanodevice performance.

1.3 Overview of neuromorphic devices

As Moore's Law approaches its limits, it faces a huge challenge to further scale down the size of devices and decrease the power consumption of computing. On the one hand, the emergence of atomic-scale 2D material families, including semiconductors, insulators, and metals, offers the possibility of replacing current silicon-based chips. Therefore, a large number of research on devices based on 2D materials has been carried out, and 2D materials also offer great prospects for designing novel devices due to their ability to be arbitrarily stacked. On the other hand, brain-inspired computing (neuromorphic computing) provides a promising strategy to lower the consumption of computing power and increase the speed of

computing in the device and circuit levels. As the basic unit of artificial neural networks, a series of neuromorphic devices have been designed to emulate the behaviors of biological neurons. In 2016, AlphaGo's victory over the world champion was an important milestone in the history of Artificial Intelligence (AI), which means that AI has the computing power to match that of the human brain. However, unfortunately, AlphaGo's design is still based on the traditional von Neumann architecture, whose memory and processor are separated, and such a mechanism leads to signal latency and high-power consumption. The human brain is a vast neural network composed of numerous neurons connected by synapses. Each neuron is responsible for both storing information and performing logical operations. Such in-memory computing allows the brain to have the ability to process multiple complex tasks flexibly and efficiently in real time. Therefore, recently the study of devices that mimic the synapses of neurons in the brain has attracted widespread interest.

1.3.1 Electrical synapse

In a neural network, neurons are connected by synapses, as shown in the Figure 1-13.[62] After the neurotransmitter released from the pre-synapse is delivered to the post-synapse, an excitatory signal will be evoked in the post-neuron, and if it exceeds the threshold, the excitatory signal will continue to be transmitted. The weight of the synapse implies the degree of tightness of the connections between neurons, which are plasticized by neural activity. Therefore, numerous synaptic behaviors such as short-term plasticity (STP), long-term plasticity (LTP), and paired pulse facilitation

(PPF) are emulated by the electronic synapses where electrical pulses play the role of neural excitation. And a series of electrical synapses have been proposed based on different physical mechanisms.

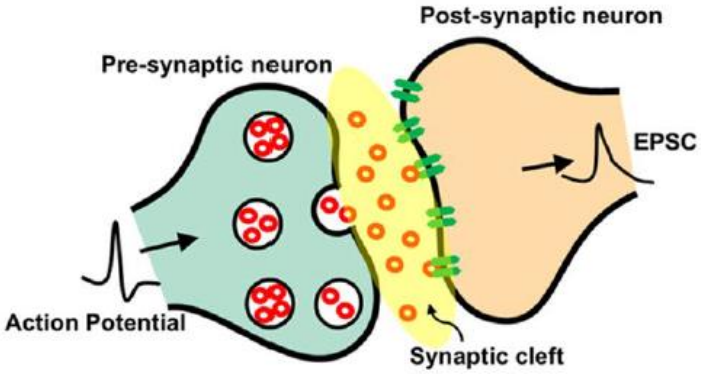

Figure 1-13 Schematic diagram of a synapse[62]

As a two-terminal device, when an electrical pulse is applied to a memristor, the resistance of the device will change in response, implying that the device has the capacity to record the previous activities, which is similar to the plasticity of the synapse. Therefore, synaptic devices based on memristors have been widely studied. The memristor as a phenomenon, in fact, involves abundant working mechanisms, as shown in Figure 1-14.[63]

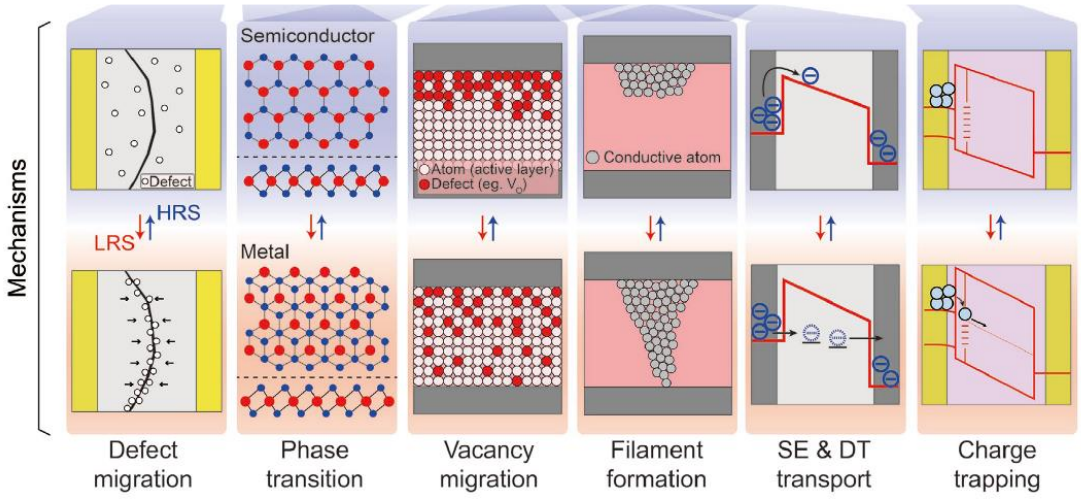

Figure 1-14 A schematic illustration of general mechanisms in memristor[63]

The memristor as the missing circuit element was first predicted theoretically in 1971 by L. Chua.[64] However, it was until 2008 that memristors were experimentally obtained in nanoscale electronic devices based on titanium dioxide (TiO_2) due to the motion of charged atomic or molecular species.[65] Forming conductive filaments in channel of electronic devices between two electrodes is a convenient and controllable method to prepare artificial synapses based on memristors. For example, Liu et al. proposed a synaptic device consisting of TiO_2 films and Ag nanoclusters to achieve enhanced memristor performance. In their work, beyond simple synaptic behaviors, comprehensive synaptic functions such as the transition from short-term memory to long-term memory have also been investigated in depth. The observation of Ag distribution by high-resolution transmission electron microscopy further confirms the formation of conductive filaments under external electric field.[66] Similar results were also obtained by Chen's group, who proposed a method to regulate the formation of conducting filaments by modulating the orientation of mesopores in the dielectric silica layer, thus achieving varying the relaxation time of memory.[67]

Migration of defects and vacancies in materials provides an additional mechanism to prepare memristor-based artificial synapses. In 2015, Hersam et al. reported a novel memristor based migration of grain boundaries in monolayer MoS_2. Experimental results show that the variation of resistance is tunable and repetitive, and switching ratio up to $\sim 10^3$ are achieved. Moreover, the gate terminal in the FET provides an additional degree of freedom to modulate the performance of the

device.[68] Subsequently, they prepared a multi-terminal memristor based polycrystalline MoS_2 film in a scalable fabrication process. Apart from the conventional neural learning behavior of long-term potentiation/depression, MoS_2 memtransistors with six terminals feature gate-tunable heterosynaptic capability, which is not possible in two-terminal memristors. More importantly, the migration of defects in the material is observed by in situ scanning probe microscopy, which reveals the process of dynamically changing the resistance by applied electrical pulses.[69] Although the mechanism for migration of oxygen vacancies was discovered at an early stage in memristors, it generally requires a large operating current. Thus, a memristor consisting of WS_2 with high performance and low power consumption based on the migration of sulfur and tungsten vacancies was demonstrated by Liu et al. A low set (reset) energy is obtained which originated from fast switching times of 13 ns (14 ns) and low program current of 1 μA in ON state. Except for synaptic behaviors that are mimicked, defect states formed by sulfur and tungsten vacancies are also identified by the authors through density functional theory calculations.[70]

Additionally, 2D memristors based on phase transition were proposed in 2015. Their results show that various metastable states appear in 1T-type tantalum disulfide (1T-TaS_2) as the thickness decreases, and several nonvolatile states are obtained by applying in-plane electrical pulses. However, the temperature requirement of 25 K hinders its application at room temperature.[71] In 2021, a nonvolatile memory based on the reversible phase transition of $SrCoO_x$ was proposed by Mou et al. and the selective stabilization of developing synapses was emulated. The image recognition accuracy of the neural network composed of the device can reach up to 99%.[72]

Unfortunately, the device still needs to be operated at a low temperature, so the development of a synaptic device based on the phase transition mechanism where it can be operated at room temperature is highly desired.

The Schottky emission (SE) to direct tunneling (DT) transition is usually observed in ultra-thin materials which refers to the transport conversion from SE to DT. Due to the atomic-level thickness, vertically structured memristors based on this mechanism show great potential in the field of low-power devices. For example, Chen et al. reported that a ferroelectric tunnel memristor whose synaptic plasticity can be tuned by interfacial modifications, the large range of potential barriers with 1.28 eV can be modulated to achieve controllable carrier transport.[73] However, there are still few reports on devices with this mechanism. In contrast, charge trapping is a more general mechanism for artificial synapses, and it has been applied in a variety of materials such as C_{60}, carbon nanotube, van der Waals materials.[74-76]

Due to the controlled surface-bound charge, ferroelectricity provides a unique mechanism for artificial synapses to mimic synaptic behaviors. The conventional ferroelectric field-effect transistor is a typical device structure, as shown in the Figure 1-15. When the gate voltage is applied, the ferroelectric domains are gradually reversed, which leads to a change in the conductance of the channel, thus enabling the emulation of synaptic behavior. In 2019, Lee and his colleagues demonstrated a synaptic transistor consisting of a ferroelectric film and an oxide semiconductor. Synaptic potentiation and depression properties are observed in their devices, and a 91.1% accuracy for handwritten digits is achieved.[77] Similar functions can also be achieved by organic ferroelectric polymer. For example, Tian et al. reported a

synaptic device using ferroelectric PVDF as the gate insulator and 2D MoS_2 as the channel material, which exhibited a high switching ratio.[78]

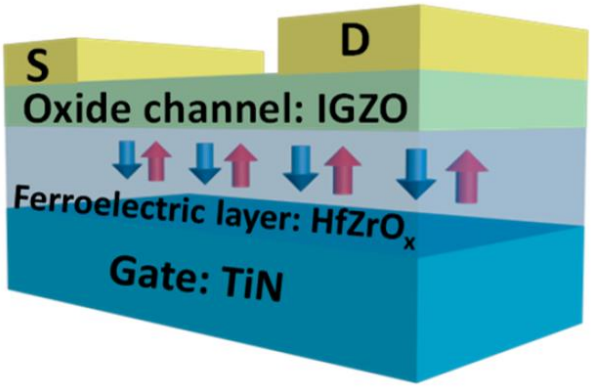

Figure 1-15 Schematic diagram of ferroelectric thin-film transistor[77]

1.3.2 Optoelectronic synapse

For humans, 80% of the information acquired comes from vision, and the high throughput of visual information requires a vision system that can respond in real time and with flexibility. Conventionally, the light signal is converted into an electrical signal through the optical sensor and then transmitted to the von Neumann architecture computer for processing, the signal latency and high energy consumption significantly limit its further development. While the human visual system shows a high degree of flexibility and sophisticated behavior in processing visual information due to its parallel computing capabilities. Besides, there is a difference between photodetectors and optoelectronic synapses, which not only convert light signals to electrical signals but also retain the memory induced by light stimuli for a period of time. Thus, in recent years, the study of optoelectronic

synapses has attracted a great deal of interest, but it is noteworthy that the field is still in its initial stages.

At present, a large number of materials have been investigated to prepare optoelectronic synaptic devices, including inorganic semiconductors, organic semiconductors, perovskite, 2D materials, etc., but their working mechanisms can be generally classified into modulation of trapping and de-trapping processes of photogenerated carriers and persistent photoconductivity (PPC).[79] The intrinsic trap state inside the material or at the interface can be exploited to modulate the recombination process of photogenerated carriers, which leads to a change in the conductance of the device. The approach can be used to mimic the biological synaptic response to light stimuli. For example, Li et al. proposed an optoelectronic synaptic device based on $InGaZnO_x$-Al_2O_3 thin film structure. In their work, ultraviolet (UV) light was utilized as a stimulus for presynapses, and currents in the transistor represented the excitatory signal of the synapse. Under light stimuli, behaviors of synaptic plasticity such as paired-pulse facilitation, transition from short-term memory to long-term memory was obtained, which resulted from trapping and de-trapping processes at the IGZO/Al_2O_3 interface and/or in the Al_2O_3 layer.[80] Additionally, Dai and his colleagues have proposed a simple method to design optoelectronic synapses by exploiting the interface charge trapping effect in organic field-effect transistors, where the organic OSC was used as the conductive channel and the PAN was used as the dielectric material. Due to the polar functional groups in PAN, remarkable charge trapping effect can be observed at the interface

of OSC/PAN. Thus, under light pulses, learning and forgetting processes in the brain are successfully emulated in their devices.[81]

By designing the heterostructure rationally, the energy band alignment at the interface can serve to separate the photogenerated carriers and prevent them from recombining, which leads to a decayed behavior analogous to that of a synapse under stimuli. Recently, Wang et al. reported a multi-functional synaptic device based on MoS_2/PTCDA hybrid heterostructure, which can respond to electrical and optical pulses. The elaborated energy band structure at the interface of the heterostructure can effectively modulate the carrier transport. Their results provide great inspiration for the design of multifunctional synaptic devices.[82] A similar design principle was also adopted by Qian et al. to design the solar-stimulated optoelectronic synapse based on organic heterostructure. At the interface of CuPc/p-6P heterostructure, photogenerated electrons are trapped in the p-6P insulating layer while holes move to CuPc, and the separation of carriers causes an increase in the channel current. A linear increase in the channel conductance is obtained and maximum recognition rate of 78% is achieved for MNIST digit patterns by their device.[83]

Persistent photoconductivity (PPC) is commonly observed in oxide semiconductors, and it is related to the vacancies in the materials. In contrast to carriers trapped which is discussed above, for PPC when the light pulse is removed, the increased conductance can be maintained for a long time or even days. In 2017, Lee et al. designed a brain-inspired photonic neuromorphic device consisting of amorphous oxide semiconductors based on PPC. Moreover, the dynamic processes of photogenerated carriers are systematically analyzed and their results indicate that

activation energy for the neutralization of ionized oxygen vacancies plays an important role in the behavior of PPC.[84] In addition to oxide semiconductors, recently PPC has also been identified to contribute to the behavior of optoelectronic synapses in 2D materials. Seo et al. constructed a flexible optoelectronic synapse based on vdW layered rhenium disulfide (ReS_2). By first-principles calculations, sulfur vacancies in ReS_2 are thought to be responsible for the PPC effect.[85]

1.4 Significance of research

Since the discovery of piezoelectricity more than a hundred years ago, piezoelectric materials have been extensively studied and utilized in the field of sensors and actuators due to the piezoelectric and inverse piezoelectric effects. In addition to piezoelectric applications, as a subclass of piezoelectric materials, ferroelectric materials with spontaneous polarization have also attracted a great deal of research interest for the preparation of electronic devices such as ferroelectric field effect transistors, ferroelectric tunneling junctions, etc. However, as Moore's Law approaches its limits, it faces a great challenge to miniaturize devices based on conventional ferroelectric and piezoelectric materials because of the critical thickness problem, which means that ferroelectricity will disappear as the thickness of the material becomes thinner. Although great efforts were made to break the critical thickness bottleneck, and new oxide ferroelectric materials have been found to be intrinsically ferroelectric even down to atomic thickness, the compatibility with silicon-based chips is still an issue. Besides, the wide forbidden band of conventional ferroelectric materials also limits its application in optoelectronic devices. The

discovery of monolayer graphene sparked research interest in 2D layered vdW materials due to their unique physical and chemical properties such as tunable energy bands and absent dangling bond on the surface. This means that there is no concern about lattice mismatch between the material and the substrate. In recent years, a series of piezoelectric and ferroelectric 2D materials have been predicted and experimentally confirmed, which offer the possibility to design novel electronic devices such as artificial synapses. Among these materials, α-In_2Se_3 is an outstanding candidate because of its robust in-plane and out-of-plane ferroelectricity, semiconductor properties and suitable energy bands for absorption of visible and near-infrared light.

Strain engineering is an effective tool to modulate the physical properties of materials, and it has been investigated in conventional materials for decades. Graphene is very promising for electronic devices due to its high carrier mobility, but the zero-band gap in graphene hinders its practical application. The successfully opening band gap of graphene by strain engineering has boosted the research about the influence of strain on 2D materials. Especially for 2D piezoelectric materials, the piezoelectric potential induced by strain can play a role in promoting or inhibiting carrier transport, so the phenomenon has been widely used in electronic devices and optoelectronic devices. However, so far, most of the generation of strain in the material relies on the mechanical deformation of the flexible substrate. The piezoelectric substrate PMN-PT provides an additional strategy to generate biaxial strain that can be precisely controlled by inverse piezoelectric effects. In addition, α-In_2Se_3 provides an excellent platform to discuss the relationship between strain and

piezoelectric potential in deformed 2D piezoelectric materials, which has not been investigated before.

Although research in the field of AI has been extremely successful, the von Neumann architecture of the computer whose memory and processor are separated has hindered its further development due to the latency of signals and high-power consumption. The human brain is a neural network composed of numerous neurons that can handle complex tasks in efficient and flexible manners. Therefore, great efforts are devoted for designing artificial synapses, which are the basic elements of neural networks. So far, diverse materials including conventional semiconductors, organic perovskite, and 2D materials have been attempted to prepare synaptic devices. However, a long-standing problem has not been solved properly, and it ever triggered the first AI winter. For a single neuron, it cannot perform linearly non-separable logic, and generally a multi-layer neural network is required which leads to a huge amount of operations. Therefore, it is highly desirable to implement linearly separable and non-separable logic at the single device level in order to simplify the current redundant artificial neural networks (ANN).

In contrast to photodetectors, biological synapses not only convert light stimuli into electrical signals but also process the received information. Although artificial vision systems based on traditional photodetectors and von Neumann architecture computers have been widely used in the fields of autonomous driving, image recognition, etc., processing high throughput information in a timely manner is still a problem that needs to be solved. Therefore, a large number of optoelectronic synaptic devices have been designed to mimic synaptic behaviors under illumination.

However, most research up to now has only demonstrated the emulation of simple optical synaptic behaviors, and few of them have reported on the multifunctionalization of synapses by integrating logical functions and information storage in order to mimic the complete human visual system. The emergence of semiconducting 2D ferroelectric materials offers the possibility to achieve this goal.

1.5 Structure of thesis

The chapters of this thesis are organized as follows:

Chapter 1: Introduction. In this chapter, the basic principles of ferroelectricity and piezoelectricity and recent advances in 2D ferroelectric and piezoelectric materials are introduced. Moreover, their potential applications in the field of strain engineering and artificial synapses are presented. In order to better understand this work, the significance of the research is arranged subsequently, and the structure of this thesis is written to facilitate reading.

Chapter 2: Experimental methods. This chapter provides detailed descriptions of methods for the preparation of 2D materials and related devices. The material characterization methods including structural characterization, ferroelectric and piezoelectric characterization, etc., as well as the electrical measurement methods for the devices are carefully discussed.

Chapter 3: Piezoelectric biaxial strain effects on the 2D α-In_2Se_3 nanosheets. This chapter describes the effect of biaxial strain induced by piezoelectric substrates on the PL and Raman spectra of ferroelectric 2D material. In addition, the role of strain

and piezoelectric potential in the material is analyzed through the laser power dependent phenomenon.

Chapter 4: Brain-inspired artificial neuron based on 2D ferroelectric semiconductor. In this chapter, an artificial neuron is carefully designed consisting of 2D ferroelectric material. Linearly separable and non-separable logic are performed in the device. In addition, controlling food intake as a nervous system-level behavior is successfully mimicked for the first time.

Chapter 5: Multifunctional optoelectronic synapse based on 2D ferroelectric material. In this chapter, a multifunctional artificial optoelectronic synapse based on a ferroelectric vdW heterostructure is proposed to emulate the entire human visual system. Beyond the successful emulation of synaptic behaviors, logical operations and information storage analogous to those of the human brain have also been integrated at the single device level for processing complex visual information.

Chapter 6: Conclusion and future prospect. This chapter provides a summary of the experimental results in this thesis, meanwhile an outlook on 2D ferroelectric and piezoelectric materials and their related applications is described.

Chapter 2 Experimental Methods

2.1 Fabrication methods of 2D material

2.1.1 Exfoliation

Mechanical exfoliation is one of the most convenient and easy methods to prepare monolayers of 2D materials, and it was first reported in the successful preparation of graphene. Currently, numerous 2D materials including TMDs, h-BN, etc. have been prepared in this way. The preparation process is shown in the Figure 2-1.[86] Firstly, a piece of 2D material crystal is placed on the scotch tape, and after repeated taping, a large number of 2D nanosheets will be obtained. Next, the tape is placed in contact with a rigid substrate, and the 2D material of the monolayer can be found among the numerous nanosheets on the substrate. The success of this strategy mainly originates from the weak interactions between vdW layers.

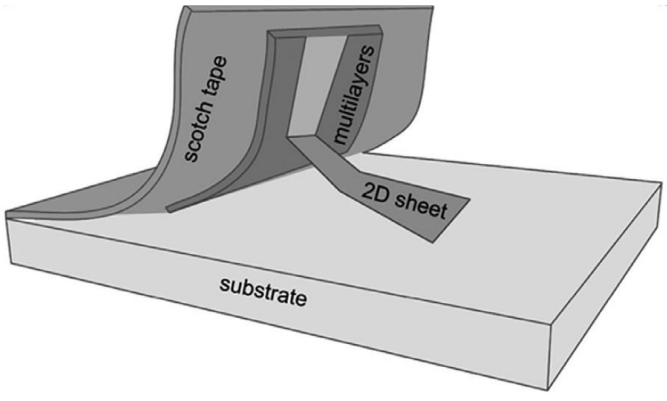

Figure 2-1 Schematic diagram of the mechanical exfoliation process[86]

The method has successfully prepared a series of 2D vdW materials, providing an excellent platform to investigate their unique physical properties, but the uncontrollability, yield and lateral size limit its practical application. Recently, Huang et al. reported a universal mechanical exfoliation method for the preparation of large-area 2D crystals with the help of Au. Their results show that 40 types of single-crystalline monolayers can be successfully exfoliated with centimeter-scale size. The approach provides a new idea to solve the drawbacks of the mechanically exfoliating nanosheets.[87]

Compared to mechanical exfoliation by tape, sonication-assisted exfoliation provides a method of preparing single or few-layer 2D materials with high yields. In 2018, Coleman et. al first reported the preparation of monolayer or few layer graphene by this simple method in different solutions such as N-methyl-pyrrolidone (NMP) and di-methyl formamide (DMF), and graphene dispersions with concentrations up to ~0.01 mg ml^{-1} was obtained. In the process of ultrasound, the ultrasonic waves and the bubbles produced by ultrasound in solution can exfoliate the 2D material crystals into nanosheets. A monolayer yield of ~1 wt% demonstrates the feasibility of the method, meanwhile X-ray photoelectron, infrared and Raman spectroscopies confirm the high quality of the exfoliated nanosheets. Inspired by the successful exfoliation of graphene through sonication-assisted exfoliation, the method has also been attempted to exfoliate other 2D materials including h-BN, WS_2, MoS_2, etc. In addition, for sonication-assisted exfoliation, the yield of the nanosheets

is also highly dependent on the choice of solution with a matching surface energy between the layered material and the solution based on the Hansen solubility parameter theory.

To enhance exfoliation, a method based on shear forces was proposed by Paton et al. in 2014.[88] Unlike ultrasound, a rotor is immersed in the solution containing the 2D material and the high shear rate exceeds 10^4 s^{-1} provides sufficient energy to allow the layered material to be exfoliated, and the yields of few layered graphene can reach up to 5.3 g h^{-1}. More importantly, their results show that the exfoliation process can be performed in several hundred liters of solution, which offers the possibility of preparing 2D nanosheets in large quantities. Ball milling-assisted exfoliation is another method to prepare 2D layered materials with high production based on a shear force. During the high-speed rotation of the container, the balls and the 2D material crystals collide with each other at a high frequency inside the container, and a shear force is applied to exfoliate the 2D material when the direction of motion of the balls is consistent with the in-plane direction of the material. However, the size of the nanosheets obtained by this method is generally smaller because the force with random orientation is also applied in the out-of-plane direction of the material.

Intercalation provides an alternative method of exfoliating layered materials, which can be used alone or in combination with sonication-assisted exfoliation to further improve yields. Strong oxidative agents can be used for intercalation, such as

in electrochemical processes where SO_4^{2-} is introduced into the gallery of 2D materials, resulting in expanding the interlayer spacing between layers. Meanwhile, the bubbles generated during the reaction can further separate the layered nanosheets. For 2D materials which have a small space between layers, alkali metals are good choice due to their small size. After the layers are intercalated, the increased spacing between the layers causes a decrease in vdW force, so it is easier to be exfoliated by the methods such as ultrasound. For example, Loh's team reported a high-yield exfoliation process based on lithium, potassium and sodium naphthalenide. The expansion and intercalation method resulted in large monolayer of nanosheets with size up to 400 μm^2 obtained.[89] However, for ceramic MAX phase materials, there is a very strong bonding between the ion and host layers, so etching is required first. In 2011 Naguib et al. reported that Ti_3AlC_2 was etched into 2D layered Ti_3C_2 in hydrofluoric acid at room temperature. This approach opened the door for exfoliating over 60 currently known MAX phases.[90]A summary of the methods for exfoliating 2D materials is shown in the Figure 2-2.[91]

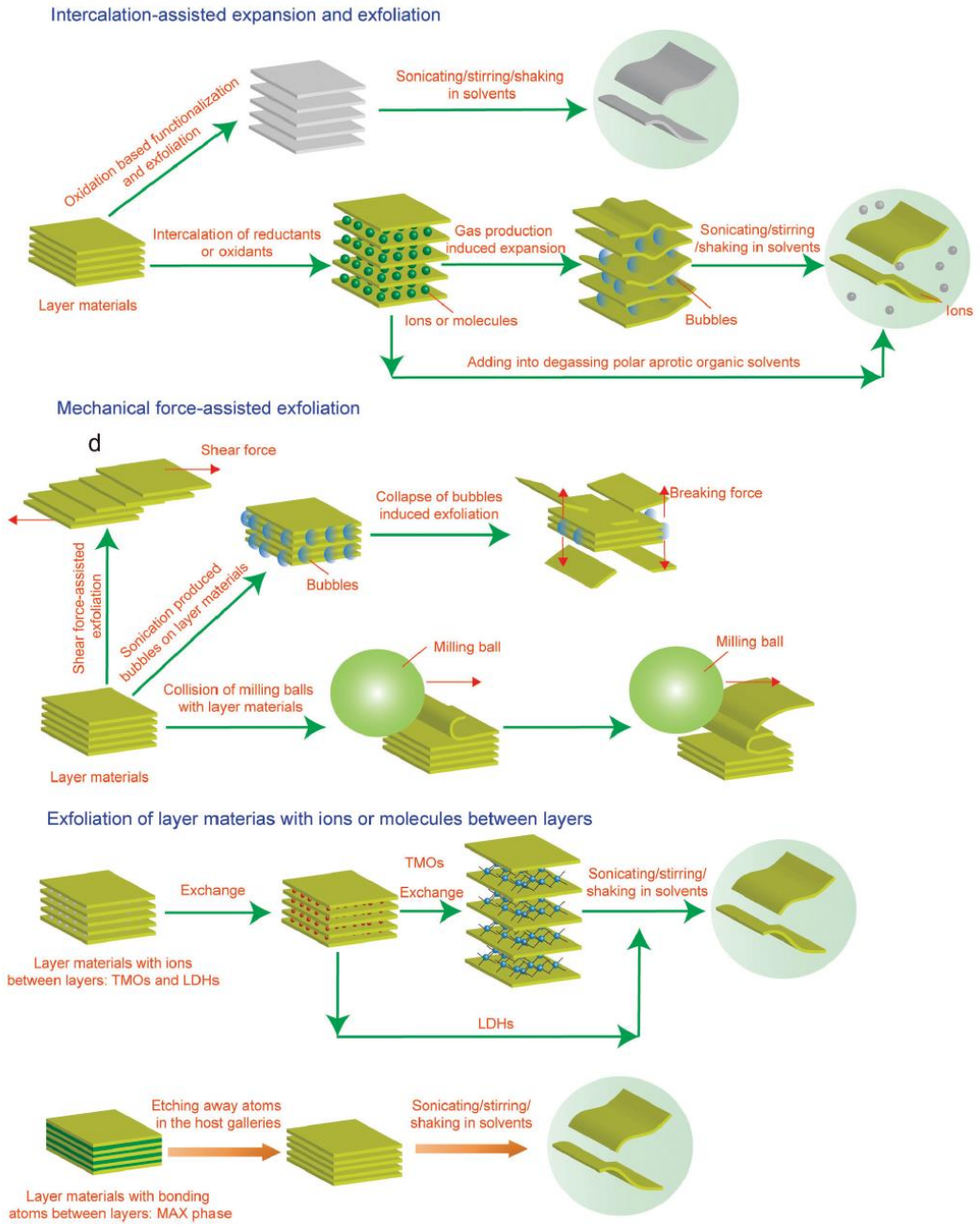

Figure 2-2 A summary of the methods for exfoliating 2D materials[91]

2.1.2 Chemical vapor deposit growth

In contrast to the exfoliation method mentioned above to prepare 2D materials, currently bottom-up fabrication is the mainstream technology to prepare

semiconductor devices. Among the many bottom-up preparation methods including CVD, sputtering, MBE, etc., CVD is chosen as an example to be introduced here due to its widely applications. Before 2D materials can be commercially applied, a series of fundamental issues such as controlled growth, doping, defect density, etc. need to be addressed for preparing high-quality electronic devices. However, currently it still faces great challenges to achieve the goal. The challenge arises firstly from the complex relationship between the numerous growth parameters and the thermodynamic and kinetic processes of crystal growth of 2D material. During the growth of the material, each parameter such as growth temperature, carrier gas flow rate, and precursor concentration can have an important influence on the crystallization quality of the material. More importantly, when one growth parameter is changed, the other parameters are also affected. For example, the partial pressure of the precursor in the reaction depends on the volatile temperature of the precursor, the carrier gas flow rate, the amount of the precursor, etc. When the carrier gas flow rate is increased, not only the total reaction gas pressure is increased, but also the volatilization rate of the precursors and the partial pressure of the precursors are changed, which may lead to a shift in the growth pattern of the material. Such a complex relationship between the growth parameters and the crystalline quality of the material leads to poor reproducibility and it generally requires a long time to optimize the growth parameters. Another challenge is that unlike the growth of conventional semiconductors which has been studied for decades, the research in the growth of 2D materials has only been going on for a very short period of time.

Therefore, the kinetic and thermodynamic mechanisms regarding the growth of 2D material crystals have not been revealed. For example, the nucleation mode in conventional semiconductor growth should not be appropriate for 2D materials due to its van der Waals forces with the substrate. Hence, a systematic understanding in 2D material growth is highly desired and it will be helpful for guiding the design of experiments.

Besides the modulation of growth parameters, the rational design of the growth system also plays a crucial role for the crystalline quality of the material. For example, Li et al. proposed a simple, low-cost method for the synthesis of high-quality monolayer and multilayer MoS_2 by in situ thermal annealing. In their reaction chamber, the precursors Mo and S are sandwiched by two Si/SiO_2 substrates and placed in the heating zone where the 2D material is grown in a confined space. In contrast to conventional CVD, the growth system they designed does not involve complex transportation of precursors, and only very little precursor is required. The characterization of the material also confirmed the reliability of the growth system.[92]Additionally, a reactive-barrier-based growth method was reported by Lim et al. for the growth of large-area monolayers of MoS_2. In their work, the sapphire substrate is placed above the precursor MoO_3, and it is interesting to note that a NiO foam is placed between them. The porous NiO foam ensures that the precursor can be deposited on the substrate and limits the precursor flux. The obtained 2D materials with larger size up to 170 μm are mainly attributed to the restricted number of

nucleation on the substrate.[93] The results show that a suitable chemical potential barrier contributes to the growth of the material in the lateral direction. In order to prepare large-area thin films of 2D materials, Zhang's team attempted to fabricate wafer-scale monolayer MoS_2 by CVD. The high-quality epitaxial films obtained demonstrate the feasibility of the growth process in CVD, and their proposed simple stamp transfer method enables the stacking of films on arbitrary substrates, which is beneficial for the preparation of large-area and diverse devices.[94]

Apart from the growth parameters discussed above as well as the structure of the growth system, the choice of substrate is also crucial for the growth of 2D materials in CVD. Conventional substrates used in epitaxial films were first attempted to prepare 2D materials. In 2014, Xiao et al. reported their successful preparation of high-quality large-sided $MoSe_2$ on SiO_2/Si, mica and Si substrates by atmospheric pressure CVD. The thickness of the monolayer and multilayer is confirmed by AFM, and the PL spectrum demonstrates the transition from an indirect to a direct bandgap as the film thickness decreases.[95] MoS_2 as a very promising candidate in the field of electronics and optoelectronics, it has also been tried to be prepared on SiO_2/Si substrate through CVD by Terrones et al. The photodetectors based on CVD-grown MoS_2 exhibit a photoresponsivity of up to 1.1 mA W^{-1} and are operated at a low voltage at room temperature.[96] Additionally, in contrast to the triangular MoS_2, Liu's group successfully synthesized dendritic MoS_2 on $SrTiO_3$ single crystals. The dendritic monolayer MoS_2 can be transferred intact to Au foil

electrodes for efficient electrocatalysts for hydrogen evolution reaction due to the abundance active sites at the edges.[97] Similarly, monolayer dendritic MoS_2 was also obtained on $LaAlO_3$ (100) substrates by a low-pressure CVD. The undulated substrate exhibited a strong substrate modulation effect that led to unique dendritic morphologies and tunable nucleation densities.[98] Subsequently, Zhang et al. successfully revealed that monolayer dendritic MoS_2 can be attributed to a prominent diffusion anisotropy of monomer precursors by experimental results and theoretical calculations.[99] Compared to the solid-state substrates mentioned above, the growth and nucleation of graphene on liquid substrates such as melted Cu and Ga exhibit better controllability due to the easier migration of carbon atoms on the substrate surface. However, for preparing devices, transfer of graphene from metal substrates to insulated substrates is required, and the process usually results in breakage of 2D materials. To avoid this procedure, Chen et al. proposed to prepare graphene on liquid insulating molten glass substrate by CVD. The uniform and well-dispersed graphene disks is obtained. Moreover, molten glass also serves to increase the nucleation uniformity as well as to improve the growth rate of graphene.[100] The discussion above demonstrates that the selection of a suitable substrate plays a crucial role in the growth of 2D materials by CVD.

2.2 Fabrication methods of heterostructures

Currently, the discovery of the 2D material family has covered insulators, semiconductors and conductors, which offers the possibility to construct diverse

heterostructures for the physical research and potential applications. Due to the layered structure and the absence of dangling bonds, 2D materials as a building block can be assembled arbitrarily, and the thickness of atomic layers also motivates new physical phenomena discovered originating from layer-to-layer interactions. In addition, the abundant choice of 2D materials for energy band alignment also paves the way for the design of high performance electronic and optoelectronic devices. Therefore, extensive research has been carried out to prepare 2D material-based heterostructures by in situ growth methods and mechanical stacking.

2.2.1 Direct CVD growth

For heterostructures, which can generally be classified as lateral heterostructures and vertical heterostructures, different from mechanical stacking, both of them can be prepared by in situ growth, and in this section, heterostructures fabricated by CVD will be discussed. Graphene, as the first discovered layered monolayer 2D material with high carrier mobility and metal-like properties, received extensive research for 2D material based heterostructure. For example, in 2014, McCreary reported the synthesis of vertical large-area and uniform MoS_2-graphene heterostructures by direct CVD growth. First, high-quality large-area graphene is grown on Cu foil by CVD, and then, the graphene is transferred to a Si/SiO_2 substrate. For cleaning the surface of graphene, the sample is annealed in forming gas. Finally, MoS_2 is deposited directly on top of graphene, using S and $MoCl_5$ as precursors, as

shown in Figure 2-3. A series of characterizations including AFM, Raman spectroscopies and so on confirmed the uniformity and high quality of monolayer MoS_2.[101]

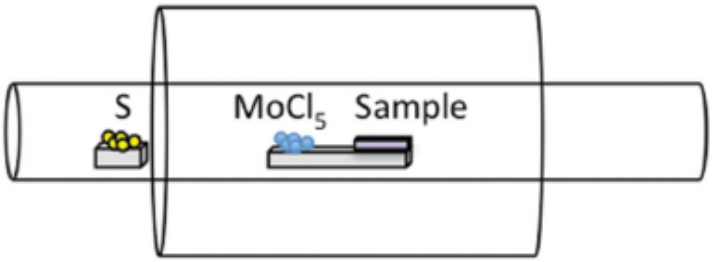

Figure 2-3 Schematic diagram of the furnace for MoS_2 growth on graphene[101]

Recently, a novel method to prepare graphene on MoS_2 was reported by Lee et al. In their work, 1,2,3,4-tetraphenylnaphthalene (TPN) was spin-coated on the prepared MoS_2 films as a precursor of graphene. The UV/ozone treatment for the TPN films served to increase the adhesion between the films and further improved the quality of the heterostructures. The Figure 2-4 shows that a sharp interface between graphene and MoS_2 can be obtained, and devices based the heterostructure exhibit excellent electrical and mechanical characteristics.[102]

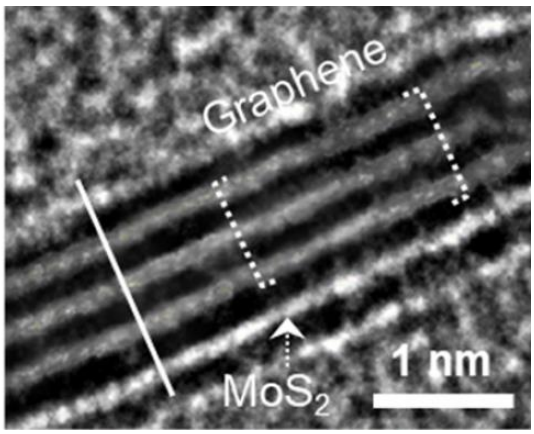

Figure 2-4 High-resolution cross-sectional TEM image of graphene/MoS_2 heterostructure[102]

For heterostructure based on 2D semiconductor materials, Li et al. proposed one-step CVD method to prepare the vertical SnS_2/SnS heterostructures. During the growth process, SnS and S powders as precursors were transported to the mica substrate by the carrier gas and high-quality vertical n-p SnS_2/SnS heterostructure was obtained. Photodetectors based on the heterostructure exhibit a high photoresponsivity and on/off ratio, which can reach up to 27.7 A W^{-1} and 2.2×10^3 respectively.[103] In order to improve optoelectronic performance of monolayers of MoS_2, a MoS_2/$MoSe_2$ heterostructure was designed through direct vapor growth by Pan's team. The high-resolution TEM confirms the high quality of the heterostructure and shows that there is no atomic alloying at the interface of the heterostructure. An enhanced photoresponsivity of 36 A/W is obtained in the photodetector based on vertical vdW MoS_2/$MoSe_2$ heterostructure.[104] Due to the atomic-level flatness and chemical inert, 2D insulating h-BN is an outstanding and promising substrate to prepare 2D semiconductor materials. Yan et al. presented the direct growth of single- and few-layer MoS_2 on tape-exfoliated h-BN, and different growth mechanisms of them are analyzed and discussed.[105]

Compared to vertical 2D heterostructures, it is more difficult to prepare lateral 2D heterostructures due to a strict requirement for lattice matching at the interface between the two kinds of materials. According to a thermodynamically stable

manner, it is easier to form TMD alloys, therefore, an alloy region is often discovered at the interface of two materials, which greatly disrupts the design of the energy band alignment and hinders the research of the intrinsic lateral heterostructure. To solve this problem, Li et al. reported a two-step epitaxial method to achieve atomic-level sharp interfaces in lateral p-n junction. As shown in the Figure 2-5, the monolayer WSe_2 was first grown on the sapphire substrate due to the requirement of a higher growth temperature compared to MoS_2. Then, MoS_2 was deposited in a separate furnace. The experimental results show that a suitable ratio between the relative vapor amount of MoO_3 and S plays a key role to avoid the formation of alloy.[106] A further experiment was carried out by Xie et al. to fabricate a lateral 2D material-based superlattice where different monolayers of transition metal dichalcogenide were repeatedly integrated in 2018. Precise modulation of the strain at the interface of the two kinds of materials is achieved by changing the supercell dimensions, which can be used to tune the photoluminescence peak of the superlattice with a range of 250 millielectron volts.[107]

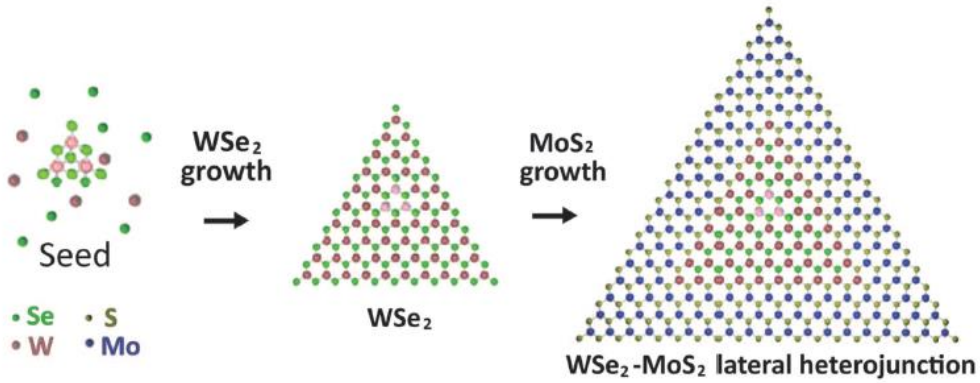

Figure 2-5 Schematic diagram of preparing lateral monolayer WSe_2-MoS_2 heterostructure[106]

2.2.2 Mechanical stacking

Compared to growth in situ, mechanical stacking is a more flexible way to prepare vertical 2D heterostructures due to the disregard of lattice mismatch. And numerous devices composed of heterostructure made by mechanical stacking such as photodetectors, field effect transistors have been widely investigated. Moreover, novel physical phenomena such as piezoelectricity, superconductivity, etc. have also been discovered in elaborately designed stacks of 2D heterostructures. Generally speaking, mechanical stacking can be divided into three steps including transfer, stacking and removal of the carrier, as shown in Figure 2-6.[108]

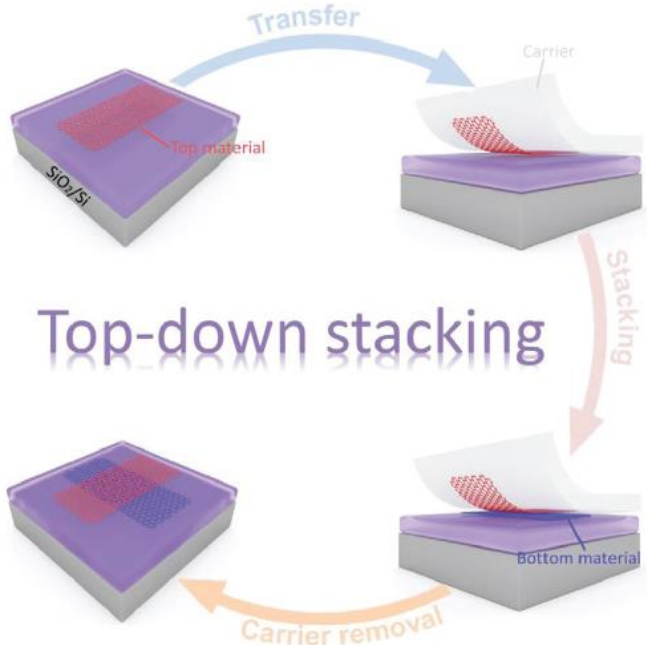

Figure 2-6 Steps for preparing vertical 2D heterostructures by mechanical stacking[108]

In the process of fabricating a heterostructure, first of all, the bottom material should be placed on a target substrate. For 2D materials grown on an insulating substrate such as Si/SiO_2 by CVD, it can be used directly for stacking 2D materials if there are no special requirements for substrate. However, for those 2D materials grown on metal substrates, such as graphene on Cu foil, they need to be transferred to the target substrate in order to prepare electronic devices. Also, monolayer or multilayer nanosheets exfoliated from their bulk counterparts can be placed directly on the target substrate via tape as previously discussed. In general, carriers can be classified into three categories: amorphous polymers membranes such as polymethyl methacrylate (PMMA), poly-propylene carbonate (PPC) and polycarbonate (PC); viscoelastic stamps, such as polydimethylsiloxane (PDMS); and metal films, such as Au, Pt films. The uniform thickness, high transparency of polymer membranes and viscoelastic stamps enable them the most popular carriers currently. Recently, thin films of metals have also been used to transfer 2D materials because of the strong adhesion between them.

In the next step, the top 2D material is transferred and stacked onto the bottom 2D material, thus forming a heterostructure. The working platform usually consists of a microscope and two sets of three-axis micrometer stages, where the position of the 2D material can be observed by the microscope, and two sets of three-axis

micrometer stages are used to modulate the position of the bottom and top nanosheets, respectively. Among the working platforms, some are also fitted with a rotary table to stack two kinds of materials at a specific angle. For example, Cao et al. reported intrinsic unconventional superconductivity in stacking two sheets of graphene where they are twisted relative to each other by a small angle.[109]

After stacking, carriers will be removed normally by one of three methods, including controlled release, thermal decomposition, and dissolution of carriers. Controlled release is a preferred option due to less contaminant residues, such as in the case of the PDMS carrier. For thermal decomposition, a suitable temperature is usually required to remove the carriers and not to cause damage to the 2D nanosheets. In addition, since most carriers are organic, they can also be dissolved in volatile reagents such as acetone, etc.

In order to prepare electronic devices, electrodes of metals need to be deposited on heterostructures. However, for ultrathin 2D heterostructures, the conventional method will induce the damage in the interface between the material and the electrodes due to the high-energy particles during the process of E-beam. In 2016, Li et al. reported an efficient and low-cost method to prepare and transfer metal electrodes for the fabrication of nano electronic devices. The electrical measurement results of the devices also confirm the feasibility of the method.[110] Furthermore, Duan's team reported that creating atomically flat interfaces between metal

electrodes and 2D materials by transferring electrodes which approaches the Schottky–Mott limit, as shown in the Figure 2-7.[111]

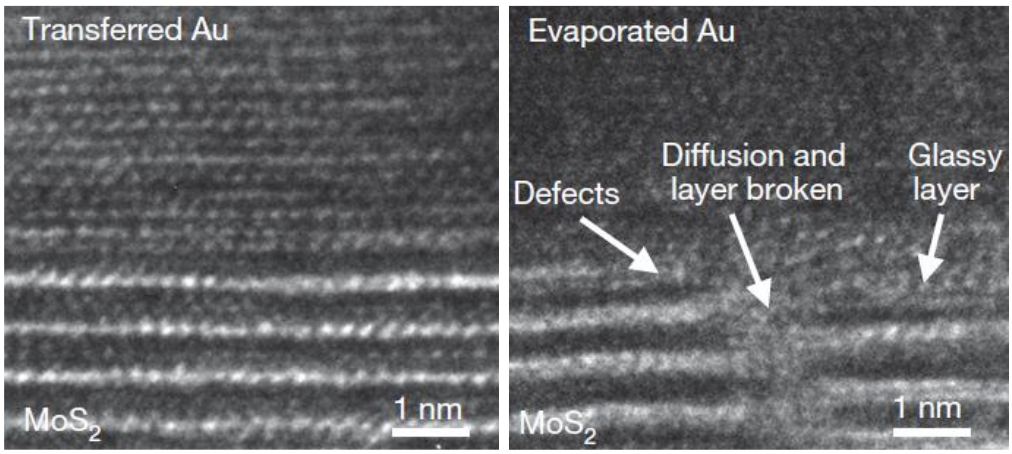

Figure 2-7 TEM images of the transferred and electron-beam-deposited Au electrode on MoS_2[111]

2.3 Characterizations

2.3.1 Structural analysis

Transmission electron microscopy (TEM) is a powerful tool to observe structures of material at the atomic level, which greatly reveals the relationship between microscopic structures and macroscopic phenomenon. The working principle of TEM is shown in the Figure 2-8.[112] A beam of electrons is transmitted through an ultra-thin sample, which is typically less than 100 nm and supported on a copper mesh. As electrons are incident on the sample, they interact with electrons and nuclei via Coulomb forces. The scattered electrons can be collected and refocused by the lens to produce a pixel point, which is similar to the behavior of an

optical microscope for photons. Compared to optical microscopy, the higher resolution of TEM primarily originates from the smaller de Broglie wavelength of electrons. In addition to image mode, the multifunctional TEM can also work in diffusion mode and scanning transmission electron microscopy (STEM) mode for the diffraction pattern and annular dark-field imaging, respectively. With the increasing research on 2D materials, the TEM plays a more and more important role to observe defects, vacancies and interfaces in 2D materials.

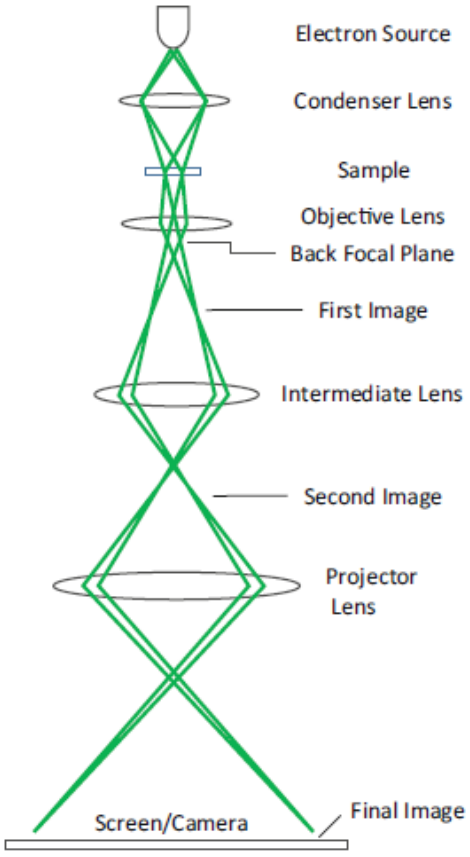

Figure 2-8 Schematic diagram of TEM structure[112]

Raman spectroscopy is another commonly accepted method to analyze the structure of a material and the vibrations of its molecules or atoms, also known as

phonons. It is also a unique fingerprint to identify and distinguish different materials. Raman scattering was first observed by C. V. Raman as well as his colleague K. S. Krishnan in 1928. When light reaches the surface of the sample, the energy of most scattered photons will not be changed, and this process is called Rayleigh scattering which is a kind of elastic scattering. However, for a minority of photons whose energy are increased or decreased due to their interaction with phonons, they are called anti-Stokes Raman scattering and Stokes Raman scattering, respectively. For the research in 2D materials, Raman spectroscopy is often used to identify the material and to distinguish different phases of one material. Moreover, it can also be used to determine the thicknesses for example there is a noticeable difference in their Raman spectra for monolayer and multilayer MoS_2.

2.3.2 Optical characterizations

The optical microscope is a tool based on the lens system to magnify the image of an object through visible light, and its output can be directly observed by the human eyes. Observing samples through an optical microscope is a convenient and time-saving method to determine location, size, and approximate thickness of material. Optical microscopes typically are comprised of two optical systems, namely an eyepiece and an objective lens. When the object is placed on the stage, the scattered light on the sample surface is collected by the objective lens and a magnified real image is produced. Normally, a revolver will be installed at the

bottom of the microscope, where several objective lens are fixed, and the user can rotate the revolver to select an ideal objective lens for the appropriate magnification. The eyepiece is at the top of the microscope tube, bringing a magnified virtual image to the eyes for the purpose of observation. In some cases, an electronic camera is integrated into the optical microscope system to acquire the image and present it on the computer screen. For 2D materials, the nanosheets exfoliated from the bulk are usually transferred to the Si/SiO_2 substrate via tape. The strongly contrast in color between the nanosheets and the substrate is very helpful for finding the location of nanosheets. Moreover, the different colors of 2D material nanosheets can also be used to estimate its thickness empirically.

Photoluminescence Spectroscopy (PL) is a nondestructive, contactless method of probing materials. When light is directed to a material, photons will be reflected, transmitted or absorbed by the material. If the energy of the photon is less than the forbidden band width of the material, the absorbed photon will cause a more intense crystal lattice vibration or intraband transition. For photons with sufficient energy, its absorption will cause band-to-band transitions of carriers in the semiconductor. According to the energy band structure, semiconductors can be classified into direct band gap and indirect band gap, which means that the carrier transition in the indirect band gap typically requires the help of one or several phonons due to the change in momentum in contrast to the direct band gap. PL is a spontaneous emission of photons when the carriers transition from the excited state to the ground state,

therefore the PL spectrum provides information about the structure of the energy band.

2.3.3 Piezoresponse force microscopy

The atomic force microscopy (AFM) is a powerful tool to probe the surface of a material based on the interaction forces between the probe and the material surface atoms, and it has greatly advanced the research in the nanoscale. As a variant of AFM, piezoresponse force microscopy (PFM) not only acquires information on the surface morphology of a material, but more importantly, it has the capacity to sense the piezoelectric deformation of the material under electric field of the tip and to image the pattern of ferroelectric domains. The schematic diagram of the PFM structure is shown in Figure 2-9. On the left side is a standard AFM structure to depict the surface morphology of the sample, while on the right side are additional components for PFM including a lock-in amplifier (LIA) and function generator.[113, 114]

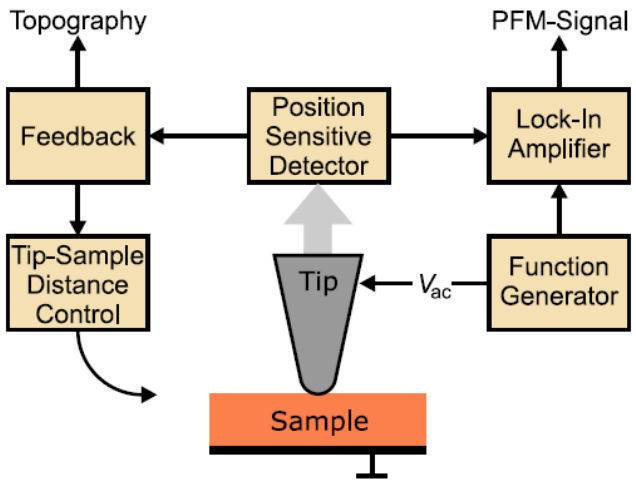

Figure 2-9 Schematic diagram of the PFM structure[113]

When AFM is operated in a contact mode, a conductive probe of PFM can provide an oscillating voltage applied to the piezoelectric or ferroelectric material, which can induce a deformation in the material based on the inverse piezoelectric effect and be detected by the probe. However, in general, for nanoscale materials even conventional oxide ferroelectric materials, its deformation amplitude may also be lower than the sensitivity of AFM, so LIA is used to extract the deformation signal from the noise. In order to visualize the ferroelectric domains, an AC voltage generated by the function generator is imposed on the material by the tip, and a contrast can be observed originating from the different PFM signals obtained from the different domains. The maximum PFM signal contrast can reach as high as 180^{o} between two domains. Moreover, the polarization direction of the ferroelectric domains can also be reversed by applying a DC voltage through the conducting probe. Therefore, PFM provides an efficient method to confirm the piezoelectricity, ferroelectricity in materials and enable the manipulation of ferroelectric domains at the nanoscale.

2.3.4 Electrical measurement

In our experiments, in order to apply a uniform electric field to the piezoelectric substrate PMN-PT, metal films are first deposited on the bottom and top surfaces of the substrate. Silver paste and copper wires are used to connect the two surfaces of the substrate with the sourcemeter Keithley 2410 which can supply a voltage up to

1100V. The high voltage ensures that the piezoelectric substrate can provide a large enough strain to the 2D material on its surface. For measuring the electrical performance of the synaptic device, it is placed in a probe station equipped with four probes. The metal shell of the probe station provides excellent shielding against external interference, so an accurate signal is obtained by Keithley 4200. Measurements for devices are performed in quiet mode, which is a suitable trade-off between measurement speed and accuracy. And the light pulse of LED or laser is controlled by a function generator in order to measure the optoelectronic performance of the device.

Chapter 3 Piezoelectric Biaxial Strain Effects on the 2D Ferroelectric α-In_2Se_3 Nanosheets

3.1 Introduction

Due to their unique physical properties and ideal energy band structure, optoelectronic devices based on 2D semiconducting materials, such as nano laser devices, light emitting diodes, photodetectors, and so on, have been continuously developed.[115-117] For fulfilling the demands of technological growth, significant efforts have been committed to the dynamically tuning of material band structure. Strain engineering provides an excellent platform to investigate and modulate the optical and electrical properties of optoelectronic 2D materials due to its low cost and straightforward manufacturing process. [118, 119] In addition, strain engineering is also a promising strategy for improving the performance of next-generation optoelectronic devices. Due to their ultrathin layered structure, strain has surprising effect on 2D materials in particular. Strain engineering, for example, has been utilized to open a tiny band gap in graphene's Brillouin zone in order to achieve the potential application of graphene. Specifically, the influence of strain on optical and vibrational properties of a variety of 2D piezoelectric materials, such as MoS_2, WS_2, and $MoSe_2$, has been extensively studied and the majority of research attribute the change in energy band to strain.[53, 120] However, the relationships between strains and the effects of strain induced piezoelectric electrical field on the optical characteristics

of III-VI layered semiconductors as an important class of 2D materials remain unexplored. As a result, it is extremely desirable to investigate strain engineering of emerging 2D piezoelectric materials in order to obtain a better understanding of the underlying mechanism. Recently, the III-VI compound α-In_2Se_3 was confirmed to be a layered van der Waals 2D material with a 1.4 eV band gap and excellent piezoelectric and ferroelectric properties, implying possible applications for photodetectors and infrared LEDs.[49, 121, 122] However, there are only very few publications on dynamically controlling the optical and luminescence properties of α-In_2Se_3.

3.2 Experimental

3.2.1 Design of measurement setup

In general, there are two methods for imposing strain on 2D materials. The first is to apply uniaxial strain by stretching or bending flexible substrates such as PDMS, PMMA, and PET. Another method is to place 2D materials onto a piezoelectric substrate to introduce biaxial strain. When compared to uniaxial strain imposed by manually bending a flexible substrate, biaxial strain can be controlled more precisely because it is modulated by applied voltage. As a result of its superior electromechanical and converse piezoelectric capabilities, the single crystalline (1-x)$Pb(Mg_{1/3}Nb_{2/3})O_3$]-x[$PbTiO_3$] (PMN-PT) was employed as the piezoelectric substrate in this work.[57, 123] The Raman and photoluminescence (PL) spectra of mechanical exfoliated layered α-In_2Se_3 nanosheets under biaxial strain triggered by

PMN-PT (001) substrate were studied in this work, which provides an effective method to modulate and investigate 2D material properties using an *in-situ* and dynamical approach.

Mechanical exfoliation of bulk crystal α-In_2Se_3 bought from 2D semiconductor Co. was used to produce nanosheets. Prior to the transfer process, a 100 nm-thick Au layer was coated on the backside of the substrate as a bottom electrode, and a 20 nm-thick Pt film was sputtered on the polished side of the substrate as a top electrode. The resistance of Au and Pt is only a few Ohms, which is substantially lower than that of the PMN-PT substrate. As a result, the majority of the bias voltage was dropped on the substrate. The schematic diagram of Raman and PL measurements is shown in Figure 3-1.

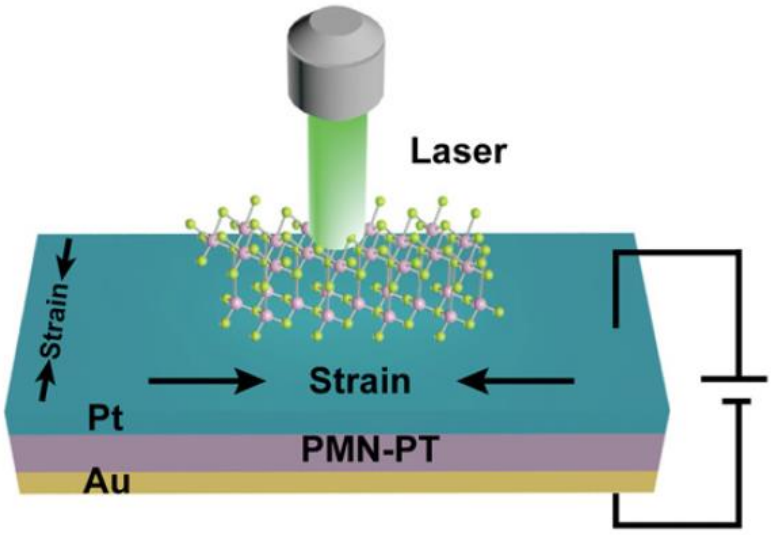

Figure 3-1 Schematic diagram of Raman and PL measurements via an electromechanical device

3.2.2 Characteristics

As illustrated in Figure 3-2, the thickness of the nanosheet was determined using an Asylum MFP 3D Infinity atomic force microscope (AFM) in tapping mode. As shown in the figure, the thickness of sample is about 30 nm. The Raman and PL spectra were analyzed by a WITEC Confocal Raman system with a laser spot size of 1 μm and an excitation wavelength of 532 nm to evaluate the optical property and vibrational behavior. In order to prevent damaging the sample, we employed a lower laser power of less than 0.5 mW in our experiment. A Keithley 2410 Source Meter provided the bias voltage on the piezoelectric substrate. For polarization, an electric field (E) of 10 kV/cm was applied to the PMN-PT substrate prior to the measurements.

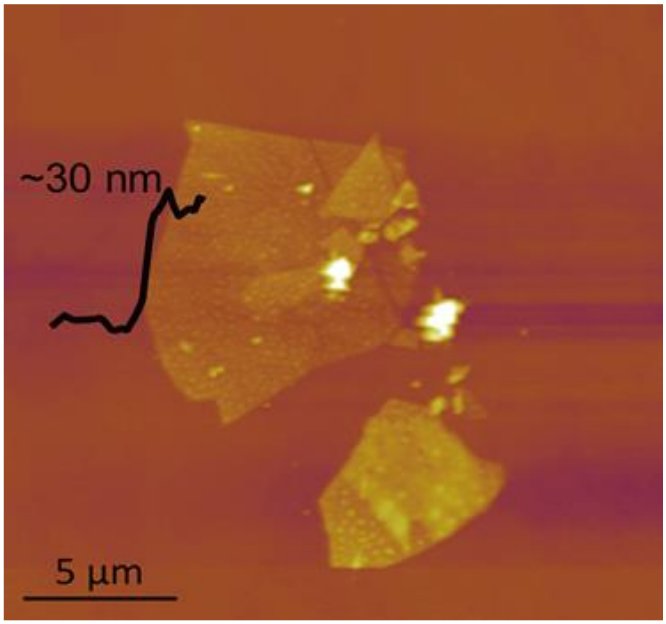

Figure 3-2 AFM image of α-In_2Se_3 nanosheets

3.3 Effect of biaxial strain on Raman spectra

According to the research, Raman peaks were discovered at 89, 104, 180, and 196 cm^{-1},[124] while Zhang et al. reported four peaks at 90, 104, 180, and 195 cm^{-1}.[125] The Raman spectrum was measured to investigate the vibrational behavior of α-In_2Se_3 on PMN-PT substrate, as shown in the inset of Figure 3-3. The Raman peaks correspond to the phonon modes of α-In_2Se_3 and are centered at 88, 104, 180, and 194 cm^{-1}. The characteristic peak, which is centered at 104 cm^{-1}, can be identified as the strongest peak and is attributable to A(LO+TO) phonon modes (inset of Figure 3-4). As a result, in the following measurement, the strongest A(LO+TO) phonon mode will be employed as a reference measured on the samples under low laser power excitation.

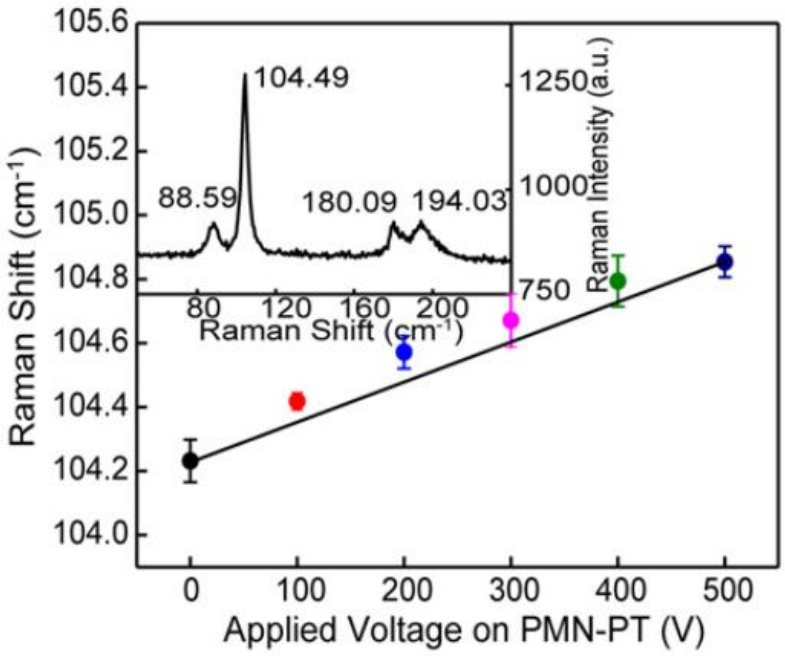

Figure 3-3 The Raman peak position as a function of the applied voltage from 0 to 500 V and inset shows the Raman spectrum of α-In_2Se_3

A positive sign is defined as applying a positive voltage to the top of the substrate (the polished side with Pt). A compressive strain can be produced by a negative or positive bias voltage with a slope of -0.04 % strain per 100 V, according to the prior study.[60] The A(LO+TO) phonon mode shifts toward higher frequency when the applied voltage increases from 0 to 500 V, as illustrated in Figure 3-3, while the opposite tendency is observed when a negative voltage is applied. For positive voltage, the relationship between the Raman shift and strain remains approximately linear at a rate of about 3.1 cm^{-1}/ %.

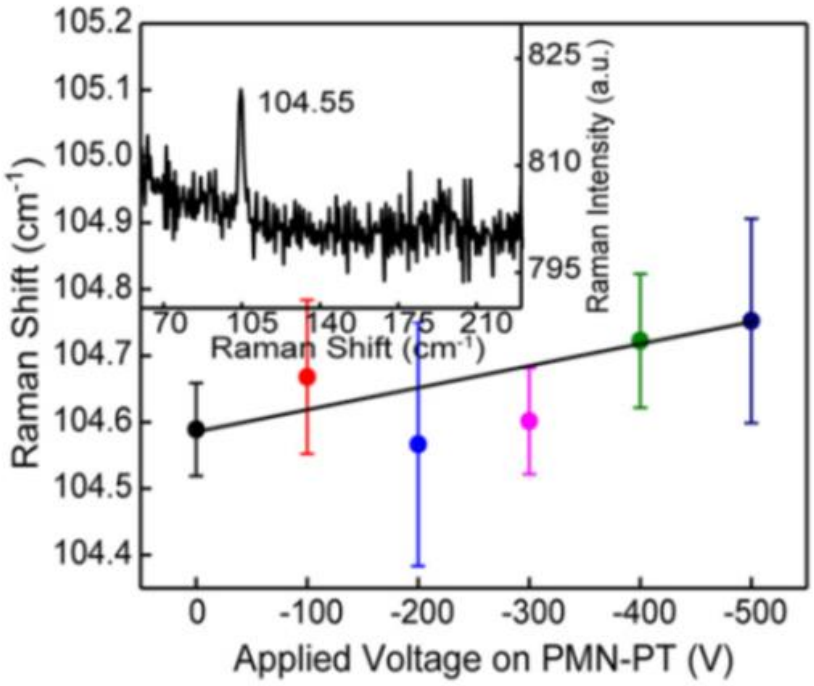

Figure 3-4 The Raman peak as a function of the applied voltage from 0 to -500 V.

The shift in the Raman peak is highly indicative of the variation in lattice constant and phonon vibrational activity that is typically observed when strain is

applied on 2D materials. The Grüneisen parameter is a useful quantity for describing the rate of phonon frequency variation as a function of strain. It is defined as follows:

$$\gamma = \frac{-1}{2\omega_0}\frac{\partial\omega}{\partial\varepsilon} \tag{3-1}$$

where ω_0 and ω are Raman frequencies under no strain and finite biaxial strain, respectively, and ε is the biaxial strain applied on α-In_2Se_3. In this case, it can be simplified as

$$\gamma = -\frac{\Delta\omega}{2\omega_0\varepsilon} \tag{3-2}$$

The obtained Grüneisen parameters for positive and negative voltage are 1.5 and 0.4, respectively. However, the piezoelectric PMN-PT substrate deformation may not have been entirely transferred to the top α-In_2Se_3 layer. The actual strain delivered to the 2D material is about -0.011 % per 100 V using the calibration where graphene was placed on PMN-PT in our previous work.[61] Hence actual Grüneisen parameters are 5.4 and 1.44, respectively, assuming that the strain can be totally transferred to α-In_2Se_3 via the Pt layer. The Grüneisen parameter in the negative voltage case is slightly less than that of the positive voltage. This could be attributable to a minor slippage during the strain application process. In other words, the data from the positive voltage example more clearly reveals strain's modulation capacity on the Raman frequency. When compared to the reported Grüneisen parameters for graphene [126,127] and MoS_2,[120] piezoelectric substrate-induced biaxial

strain can provide a more powerful tool for modulating and investigating lattice vibration, as shown in the Table 1.

Table 1. Comparison of inducing strain on material phonon

Material	Method	Grüneisen parameter	Ref.
Graphene	High pressure	1.4	126
Graphene	Flexible substrate	1.9	127
MoS_2	Flexible substrate	1.1	120
α-In_2Se_3	PMN-PT	5.4	This work

3.4 Effect of biaxial strain on PL spectra

To investigate the evolution of electronic structure in few-layered α-In_2Se_3 nanosheets under biaxial strain, the PL spectra were measured and normalized using their respective maximum values. With 0.1 mW laser power, a PL peak at 833.5 nm was observed under 0 V after polarization, as shown in Figure 3-5(a). When the positive voltage is increased, the PL peak shows a blue shift, and the overall variation can reach up to 6.6 nm (11.87 meV). Similarly, as the negative voltage varies from 0 to -500 V, the PL wavelength decreases linearly from 831.6 to 826.3 nm in Figure 3-5(b). The inset shows the PL emitting-wavelength as a function of applied voltage on the PMN-PT substrate, demonstrating that the behavior of the PL peak shift is similar under positive and negative voltages due to voltage-driven piezoelectric induced biaxial compressive strain.

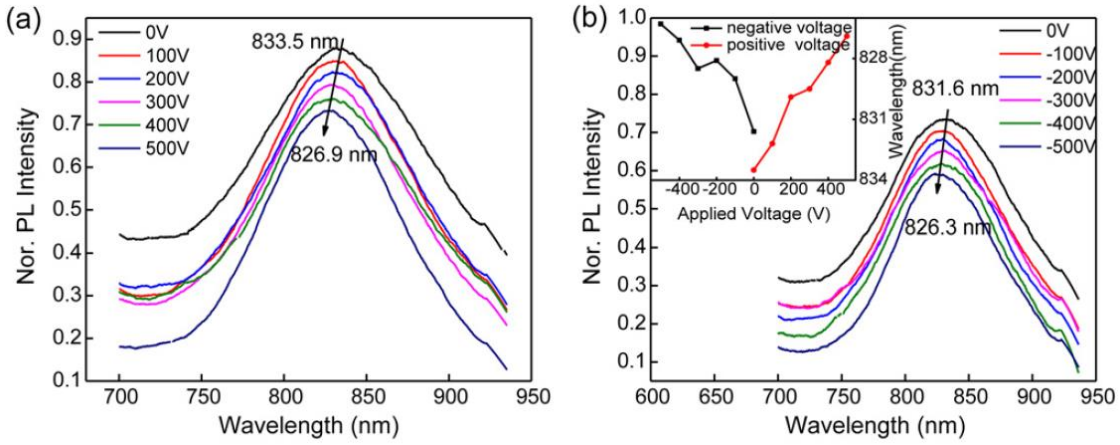

Figure 3-5 PL spectra under various applied voltages from (a) 0 V to 500 V and (b) 0 V to -500 V with 0.1 mW laser power. The inset shows the PL peak position as a function of applied voltage from -500 V to 500 V.

It is worth noting that the tunability of the blue shift in the PL peak under strain can reach nearly 215.82 meV/ %. This value measured from the α-In_2Se_3 nanosheets is significantly higher than that measured from conventional semiconductors such as ZnO microwire,[128] silicon nanowire,[129] and GaAs/AlGaAs quantum dots,[130] as shown in the table below.

Table 2. Effect of strain on the PL shift

Material	Tunability of PL by strain (meV/%)	Ref.
ZnO nanowire	8.5	128
Silicon	100	129
GaAs/AlGaAs quantum dots	70	130
α-In_2Se_3	215.82	This work

3.5 Strain induced piezoelectric field

In general, applied strain can cause variations in band gap of semiconductors, and the imposed electric field can also play a role. In graphene, for example, a band-gap open of 200 meV was observed under an electric field of 1 V/nm.[131] To rule out the effect of the electric field on α-In_2Se_3, we used a careful design of the α-In_2Se_3 /Pt/PMN-PT/Au structure. The electric field was essentially imposed on the Pt/PMN-PT/Au structure in this configuration, with no applied electric field through the α-In_2Se_3 nanosheets. As a result, the applied electric field had little effect on the variation of the band gap. It should be noted that the strain can also induce a piezoelectric field in α-In_2Se_3, and detailed discussions about the relationships between the piezoelectric electric field and band gap will be shown in the following sections.

The evolution of PL peaks as a function of laser power is shown in Figure 3-6 under various polarization and electric field conditions. Before the substrate is polarized, nanosheets exhibit a slight blue shift with increasing laser power, as shown in Figure 3-6(a). This is attributable to the Burstein Moss Effect, which is common in semiconductors with narrow band gaps.[132] As the laser power increases from 0.1 to 0.5 mW after polarization, a red shift from 833 to 836 nm can be seen in Figure 3-6(b). The behavior is analogous to that of an electric field applied to the PMN-PT substrate. Despite the fact that no voltage is applied to the substrate, remanent polarization causes some biaxial strain. Here, a positive voltage case is taken as an

example. The variation of red shift becomes larger and larger as the applied voltage increases from 0 to 500 V under laser power ranging from 0.1 to 0.5 mW. Clearly, when the voltage reaches 500 V, the laser power-dependent red shift from 826.9 to 836.5 nm can be seen in Figure 3-6(c).

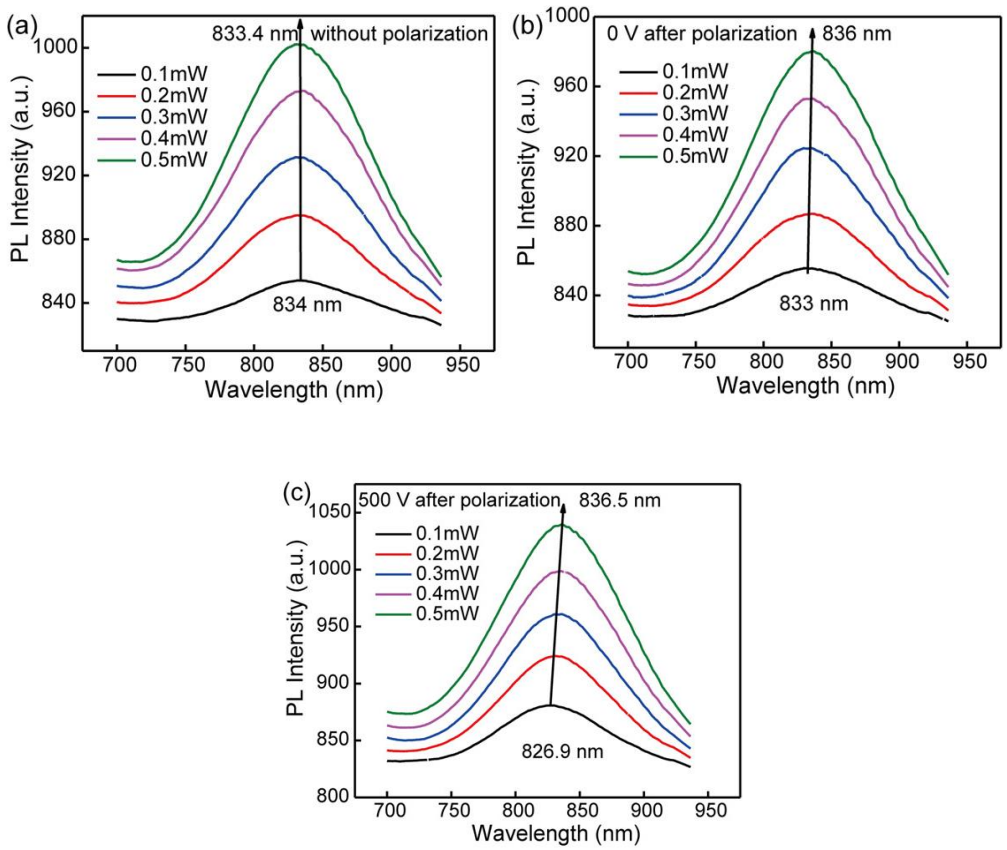

Figure 3-6 PL spectra under various laser powers (a) before polarization, (b) 0 V after polarization, and (c) 500 V after polarization

The relationship between the PL red shift and laser power clearly demonstrates the effect of the piezoelectric field on the α-In_2Se_3 band gap. Logically, biaxial compressive strain and strain induced piezoelectric field can both influence the band gap of nanosheets. When an electric field is applied to the PMN-PT substrate, the

induced strain on α-In_2Se_3 remains constant regardless of the intensity of the incident laser. However, as laser power was increased, we observed a gradual shift of the PL peak towards the wavelength for the fully relaxed nanosheet case in Figure 3-7.

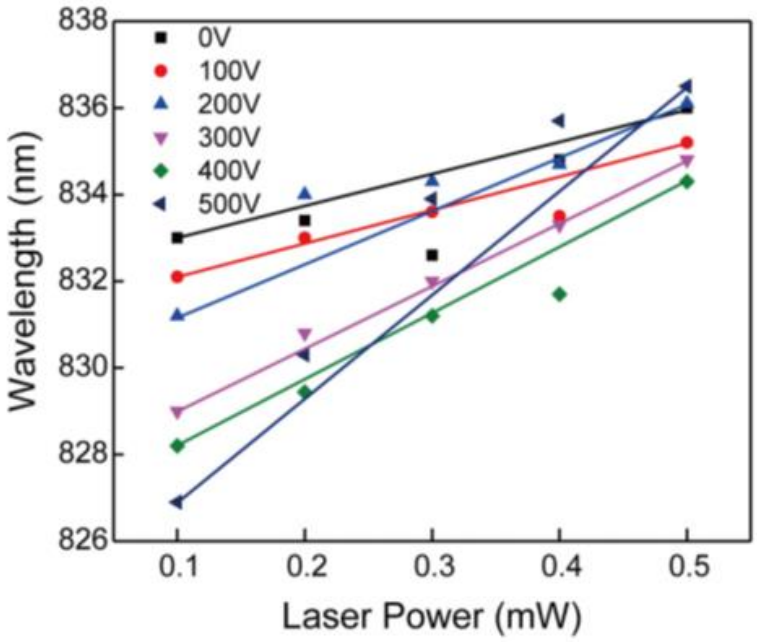

Figure 3-7 PL peak position as a function of laser power at various applied voltages

As a result, it is possible to speculate that the tuning of the α-In_2Se_3 band gap is not directly induced by biaxial compressive strain. The PL peak shift can be attributed to the screening of the piezoelectric field by the photoexcited carriers, and the analysis of excitation power dependent PL spectra is a common way to determine the relationship between piezoelectric effect and band gap variation of a piezoelectric material, such as GaN self-assembled quantum dots on AlN,[133] InAs quantum dots grown on GaAs substrates,[134] and InGaN quantum wells.[135] Due to the non-centrosymmetric structure of α-In_2Se_3, experimental studies have confirmed the coexistence of out-of-plane and in-plane piezoelectricity. There were two types of

electric fields in the nanosheets in this study: the piezoelectric field and the built-in electric field induced by the Pt/α-In_2Se_3 Schottky junction. Because the Schottky contact built-in potential remains constant under varying strain, the piezoelectric field is the only factor influencing the PL peak shift. Polarization-induced charge density n can be calculated as follows:

$$n = \frac{2dY\varepsilon}{e} \quad (3\text{-}3)$$

where d is the piezoelectric constant, Y is the Young's Modulus, ε is the strain and e is elementary electric charge. According to the references, d_{33}=5.6 pC/N,[122] d_{11}=2.55 pC/N;[136] Y001=36.47 GPa, Y100=105.48 GPa.[137] When a -0.055% strain was imposed in-plane under 500 V, a 0.11% strain along the c-axis was induced simultaneously, assuming the volume of the α-In_2Se_3 unit cell was constant. As a result, the polarization induced charge concentration is 2.8×10^{13} cm^{-2} and 1.8×10^{13} cm^{-2} along in plane and out of plane, respectively.

To better understand the effect of photoexcited carriers on the piezoelectric field, a semiquantitative estimation of the number of e-h pairs present in α-In_2Se_3 at 0.5 mW laser power is performed. The absorption of α-In_2Se_3 is 60%,[138] and the lifetime of the e-h pair is 70 ms.[139] In this case, we assume that each photon absorbed by the nanosheet produces an electron-hole pair. When compared to the polarization-induced charge concentration, the generated photoexcited carriers have a much higher charge density on the order of 10^{22} cm^{-2}. The calculation above shows that photoexcited carriers can effectively screen the strain-induced piezoelectric field. In

practice, the quantum yield cannot be 100%, and the Schottky contact-induced space charge can recombine with photoexcited carriers. As a result, the blue shift of the PL peak with increasing voltage is caused by the strain-induced piezoelectric field, and the laser power dependent red shift implies that the piezoelectric field effect on the α-In_2Se_3 band gap can be effectively eliminated by photoexcited carriers, as shown in Figure 3-8.

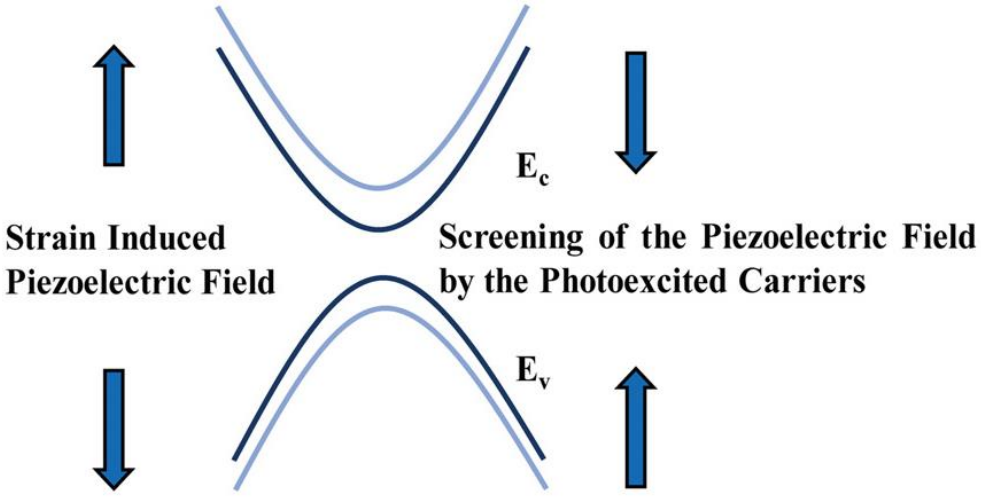

Figure 3-8 Schematic energy band structure under piezoelectric fields and laser powers

3.6 Summary

In conclusion, we showed that the α-In_2Se_3 Raman spectra and PL characteristics are highly tunable under compressive biaxial strain induced by a piezoelectric PMN-PT substrate. Biaxial strain can be generated and delivered to α-In_2Se_3 nanosheets by precisely modulating bias voltage on the substrate, resulting in a noticeable shift in Raman and PL spectra. The vibrational behavior of α-In_2Se_3 is

investigated using the Grüneisen parameter. Furthermore, the effect of a strain-induced piezoelectric field on the α-In_2Se_3 energy band is discussed, and the laser power dependent PL shift is attributed to the screening of the piezoelectric field by photoexcited electron-hole pairs. This study sheds light on the piezoelectric PMN-PT substrate's promising potential as an ideal platform for tuning the electronic structure and optical properties of 2D III-VI compound materials.

Chapter 4 Brain-Inspired Artificial Neuron Based on 2D Ferroelectric Semiconductor

4.1 Introduction

Over the last several decades, the rise of brain-inspired computing systems has resulted in spectacular success in a variety of fields, including image recognition and machine learning which is a promising candidate to overcome the current bottleneck in von Neumann architecture computers.[140-144] Nonetheless, implementing a large number of logical functions and neural responses analogous to those in the human brain continues to be extremely difficult. It is widely believed that a multilayered neural network is required for XOR functions (linearly nonseparable problem), regardless of whether they are implemented in hardware, algorithms, or the human brain. Frank Rosenblatt proposed the Perceptron (a single artificial neuron) in 1958 for supervised learning of binary classifiers capable of performing linearly separable logic operations.[145] At the time, mainstream researchers were optimistic that this was the start of the process of creating intelligence. However, the first artificial intelligence (AI) winter occurred in 1969 as a result of the publication of Marvin Minsky and Seymour Papert's book *Perceptrons*, in which they demonstrated that a single artificial neuron was incapable of learning XOR functions.[146] It's worth noting that, until recently, the XOR function still required a multilayered neural network to execute, and the problem was solved at the expense of using a considerable amount of computational resources, severely impeding the development of AI with energy-

efficient and sophisticated behaviors. Intriguingly, Larkum's team reported in 2020 in *Science* that a single human layer 2/3 cortical neuron is capable of performing the XOR operation, which has never been observed in any other species.[147] This discovery challenges previously owned beliefs about how biological neurons compute and serves as a crucial source of inspiration for the construction of an artificial counterpart.

On the other hand, as a neural device, emulating the complicated activities of biological neurons enables the AI to respond appropriately and flexibly to various conditions encountered in the actual world.[148] Controlling food intake, for instance, is a synergy of positive and negative feedback that typically involves the collaboration of several organs and neurological systems.[149, 150] When a person is hungry, food can provide a sense of pleasure and motivate him to seek out additional food. In comparison, if he or she is satiated, food reduces the level of pleasure in the brain, signaling the individual to quit eating. The ability of a single stimulus to evoke a range of responses under a variety of conditions indicates the human brain's capacity to manage complex tasks. However, no previous effort has demonstrated such an emulation of the nervous system.

Creating an artificial neuromorphic computing system with the capabilities of the human brain has been a critical source of AI innovation throughout history. As a result, considerable effort has been made to design artificial neural devices using a variety of mechanisms, including ion migration, phase transition, and electron/hole

transfer, [151-153] and a wide range of materials, including conventional semiconductors, two-dimensional (2D) materials, and organic perovskite, have also been extensively investigated.[154-158] However, current research only focuses on mimicking and enhancing the simple behaviors of biological synapses, few previous work has attempted to functionalize their artificial neurons in order to achieve complicated logical functions and flexible behaviors such as food intake control. The primary reason that only a subset of fundamental biological behaviors can be accomplished in electronic devices is because even a single neuron also has an enormously complicated structure that enables it to conduct a variety of actions. Ferroelectric materials with spontaneous electric polarizations can give another degree of freedom for device functionalization, and have been widely employed in memory and logic devices for decades.[159-161] At room temperature, the discovered 2D ferroelectric semiconducting α-In_2Se_3 exhibits exceptionally robust ferroelectricity, even down to a single layer.[49, 162, 163] Due to the coupling between in-plane (IP) and out-of-plane (OOP) polarizations, various functionalities can be achieved in a single artificial neuron.

In this work, an artificial neural transistor based on 2D ferroelectric α-In_2Se_3 was proposed to mimic the human brain cortical neuron. Specifically, linearly separable and nonseparable logical functions can be performed at the device level rather than through a neural network, and the underlying mechanism is analysed in this chapter. Additionally, fundamental synaptic behaviors such as short- and long-

term plasticity are demonstrated. The bottom gate can act as a pre-synapse and neuromodulator when equipped as a third terminal. Our proposed device-based artificial neural network (ANN) achieves an accuracy of 85 percent for both small and MNIST handwritten digits images. Due to the robust IP and OOP ferroelectricity of α-In_2Se_3, our device is capable of successfully mimicking human food intake control. This prototypical demonstration presents a novel approach for implementing complex tasks analogous to those found in the human brain through an artificial neuron and effectively simplifying the current artificial neural network.

4.2 Experimental

4.2.1 Device fabrication

Au electrodes (30 nm) were fabricated using a standard lithography method and electron-beam evaporation on a Si/SiO_2 (300 nm) substrate. The nanoflakes were mechanically exfoliated from the bulk supplied from HQ Graphene onto Si/SiO_2 (300 nm) substrate. Then, employing dry transfer, Au electrodes were picked up and deposited on the nanoflakes to generate vdW connections which avoids the destruction of the interface by energetic particles during the E-beam process.[111] The artificial neural transistor is schematically illustrated in Figure 4-1.

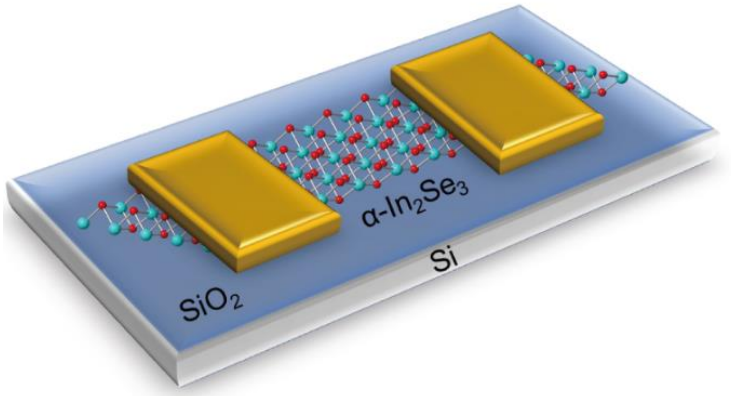

Figure 4-1 Schematic diagram of the device structure

4.2.2 Characterizations to verify ferroelectricity

Due to the asymmetry of the lattice, only the α-phase of In_2Se_3 shows IP and OOP ferroelectricity. A Raman spectrum was utilized to verify the lattice structure of the material used in this experiment. Four Raman peaks are shown in Figure 4-2a at 88, 104, 180, and 193 cm^{-1}, which correspond to the E, A(LO+TO), A(TO), and A(TO) modes of 2D layered α-In_2Se_3, respectively.[164] Additionally, the top image of a high-resolution TEM confirms hexagonal symmetry of α-In_2Se_3 (Figure 4-2b). The PL measurement shows a semiconducting band gap of 1.4 eV in Figure 4-2c. The α-In_2Se_3 exhibits two distinct stacking modes, rhombohedral (3R) and hexagonal (2H), which correspond to the space groups R3m and P63/mmc, respectively.[165] Fortunately, they are both intrinsically ferroelectric. Our previous research indicates that the crystal employed in this experiment belongs to the R3m space group. The schematic diagram of crystal structure is shown in Figure 4-2d.

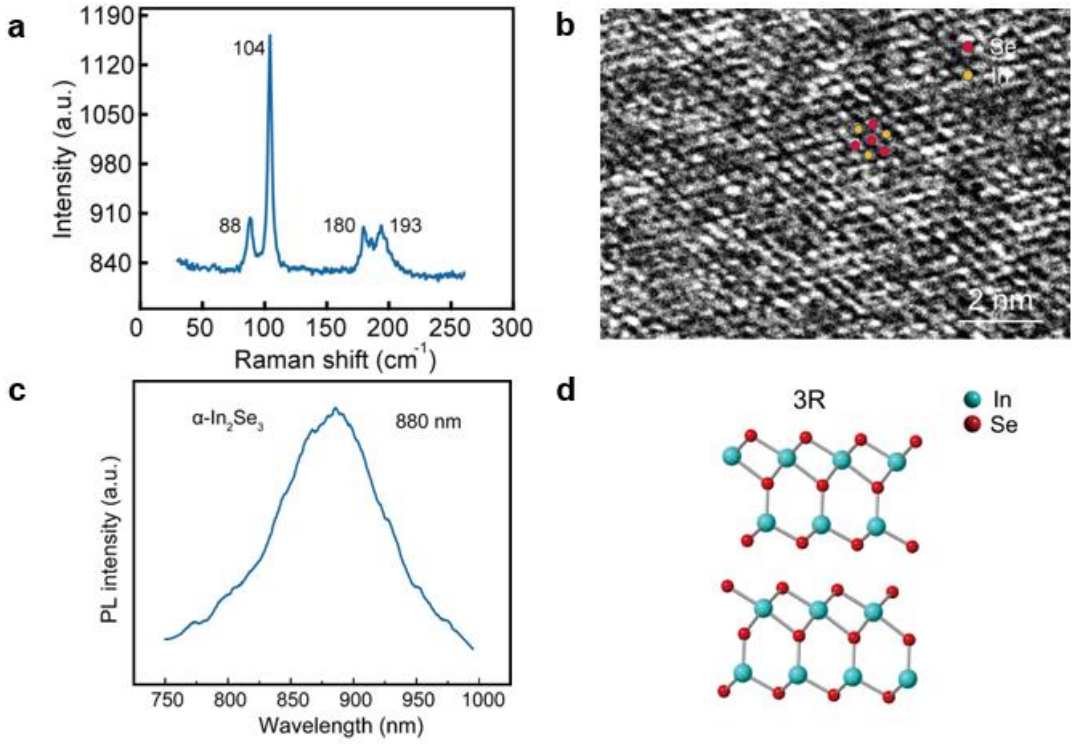

Figure 4-2 a) Raman spectrum of α-In_2Se_3, the peaks are located at 88, 104, 180 and 193 cm^{-1}, respectively. b) Top-view high-resolution TEM of the α-In_2Se_3 nanosheet with 3R structure in this work, which shows its hexagonal symmetry. c) PL spectra of α-In_2Se_3 nanosheet on Si/SiO_2 substrate under 532 nm laser are measured. The peak location of 880 nm indicates the semiconductor nature of the material. d) The crystal structure of α-In_2Se_3 with rhombohedral (3R) stacking mode. The ferroelectricity can be attributed to the central Se atom's lateral movement.

The interlocked OOP and IP ferroelectric polarizations are generated by the lateral movement of the central Se atom driven by an applied external voltage, which demonstrates robust ferroelectricity at room temperature and even at the atomic scale. The ferroelectricity of α-In_2Se_3 nanoflakes was investigated using piezoresponse force microscopy (PFM) after they were transferred on a conductive Pt substrate. As

illustrated in Figure 4-3a, both OOP and IP phase images exhibit the opposite ferroelectric polarization directions of different domains. Additionally, Figure 4-3b shows the phase and amplitude hysteresis loops generated using Dual AC Resonance-Tracking (DART) mode of PFM, which are typical in ferroelectric materials. The polarity of ferroelectrics can be reversed with the external electric field, as shown by the sharp change in the parallelogram-like piezoelectric response loop and butterfly-like amplitude loop.

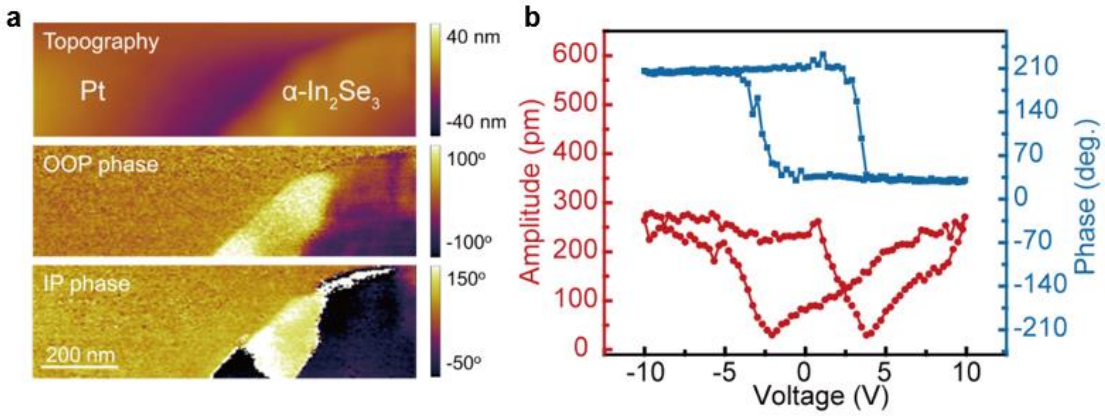

Figure 4-3 a) The topographic, OOP and IP PFM phase images are used to verify the ferroelectricity of the material. b) PFM phase and PFM amplitude hysteresis loops of α-In_2Se_3 on a conductive substrate indicate its domain can be reversed under external electric field

In Figure 4-4a, four-stage *I-V* curve loops are generated under varying maximum sweep V_{DS}. After stage 1, the ferroelectric polarization directions of domains were aligned with the external electric field. A positive voltage converts the channel from the high resistance state to the low resistance state by stage 2 to 3. According to previous research, IP ferroelectricity, rather than OOP, is responsible

for inducing the *I-V* curve loop with the stages sequence depicted in the figure. Additionally, Figure 4-4b illustrates the transfer curve of a ferroelectric transistor based on α-In_2Se_3 with bidirectional sweep gate voltages ranging from -30 V to 30 V with a fixed V_{DS} of 1 V. And a clockwise hysteresis loop is obtained, which demonstrates the ability of OOP ferroelectricity to modulate the carriers in the channel of device.

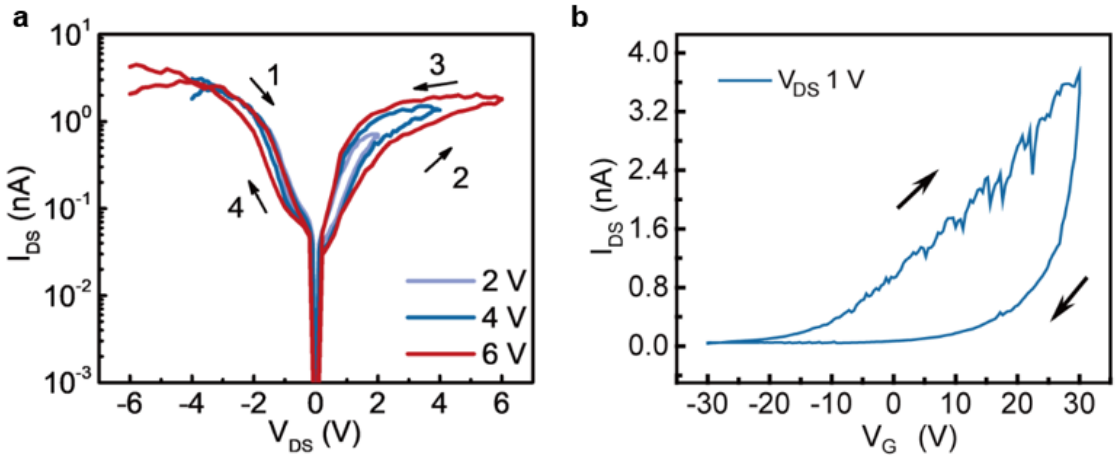

Figure 4-4 a) *I-V* hysteresis curves under V_{DS} sweep of 2 V, 4 V and 6 V due to the IP ferroelectricity. b) The transfer curve of transistor, the clockwise hysteresis loop is induced by OOP ferroelectricity

4.3 Working principle

For conventional ferroelectric FETs, the gate dielectric is typically a high-k oxide-based ferroelectric material, and the carriers in the channel are controlled by the polarization bound charges at the gate dielectric-channel interface. The devices can exhibit a variety of conductance states by changing the polarization direction of the domains in ferroelectric materials. In comparison, the device employing

ferroelectric semiconductors α-In_2Se_3 as the channel demonstrates an entirely unique working principle. When an external electric field polarizes α-In_2Se_3, the polarization bound charges emerge on the upper and lower surfaces of channel. Both positive and negative bound charges impose an impact on the majority carriers (electrons) in semiconducting n-type α-In_2Se_3, thus controlling the magnitude of the drain current in a field effect transistor.

The polarization of the channel can be categorized as entirely polarized or partially polarized in terms of the equivalent oxide thickness (EOT). According to previous research, the 300 nm SiO_2 insulator used in our study has a high EOT,[166] which results in a weak electric field across the channel and insufficient polarization switching of α-In_2Se_3. When a positive voltage is applied to the bottom gate, the device enters a ferroelectric polarization up (P_{FE}) state, in which the free electrons are forced away from the channel by the positive bound charges and the energy band at the interface bends upward, resulting in a low conductance state (Figure 4-5a, b). In comparison, as depicted in Figure 4-5c and d, a negative gate voltage can induce a polarization down state, resulting in the high conductance state. This is the reason why the transfer curve presents a clockwise loop, and the results contribute to understanding the mechanism of emulating complicated biological neuronal activities in the next sections.

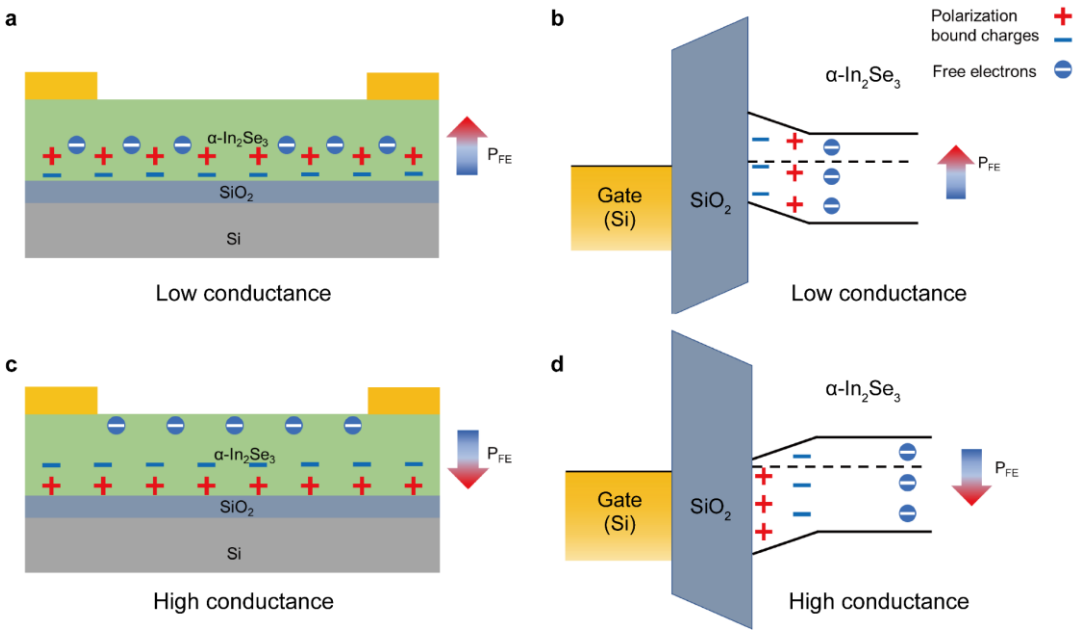

Figure 4-5 The working mechanism of artificial neuron based on ferroelectric 2D α-In_2Se_3. a) After applying positive voltage, the channel is in a state of ferroelectric polarization upward and low conductance, b) The corresponding energy band diagram. c) After applying negative voltage, polarization direction is switched, the channel shows high conductance, and d) Energy band at the interface bends downward

4.4 Perform logics in the device

4.4.1 linearly nonseparable logic

Figure 4-6 shows the structure of a biological neuron, which comprises of dendrites, nucleus, soma, axon, and axon terminal. There are two states of a neuron in terms of excitation and non-excitation, which can be denoted by the numbers 0 and 1. A synapse is the connection between the dendrites and axon terminals of other neurons; the weight of the synapse indicates the degree of influence that other

neurons can apply. When signals, such as neurotransmitters and electrical stimuli, are input via the dendrites, the soma responds synchronously. If the total of all inputs exceeds the threshold, the excitatory signal is delivered through the axon terminal to other neurons.

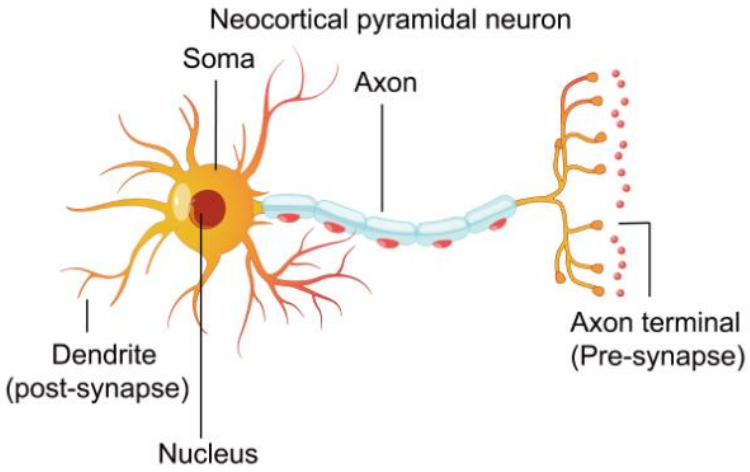

Figure 4-6 Schematic diagram of neocortical pyramidal neurons in brain

The artificial neuron is a biological analogue that is utilized for supervised learning of binary classifiers, as seen in Figure 4-7. The inputs (X_i) are multiplied by their respective weights (W_i), and then the multiplied values and the constant b are added to produce a sum, with b acting as a bias to move the sum away from the origin. Finally, the activation function will convert the total value to a single binary output value (0 or 1), emulating the excitation and non-excitation states of biological neurons.

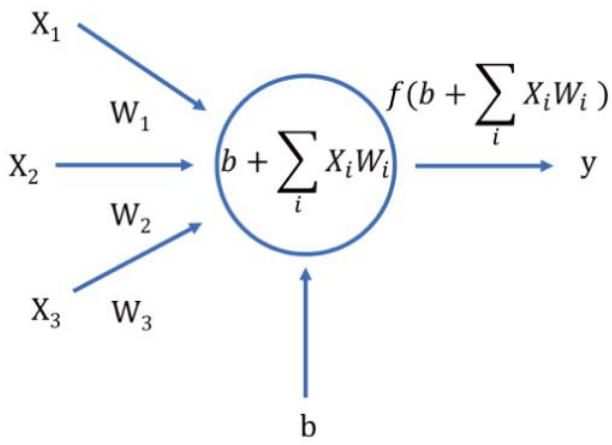

Figure 4-7 Working mechanism of Perceptron

In other words, if the sum value exceeds the specified threshold, the artificial neuron outputs 1, and vice versa, if the sum value is less than the predefined threshold, the artificial neuron outputs 0. The linearly separable logic gates AND, OR, and NOT are depicted in Figure 4-8, where the blue circle represents output 0, the red cross represents output 1, and the axes represent the inputs. The AND logic gate is used as an illustration; as can be seen from the figure, the outputs 0 and 1 are linearly separated by at least one straight line in the plane. As a result, 0 is on one side of the line, while 1 is on the other. For the XOR logic gate, however, one curved line is required. This indicates that a single artificial neuron cannot perform an XOR gate.

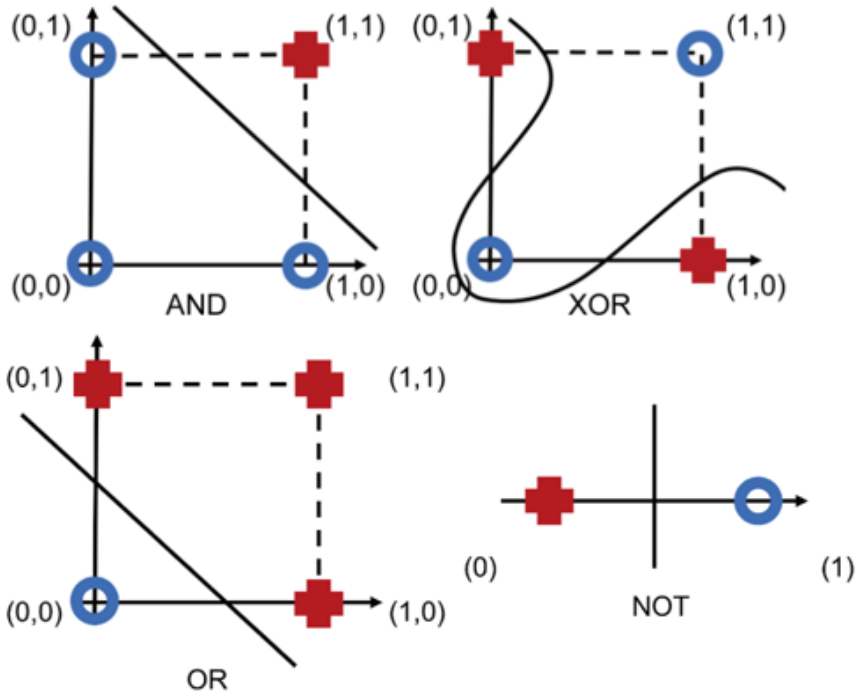

Figure 4-8 Logic gates of AND, XOR, OR and NOT

Stewart et al. proposed the 'stateful' logic and implemented it in resistive memory using the sequential logic principle, where the device can both store and perform logical functions.[167] In comparison to combinational logic, the output of sequential logic is not only dependent on the current input, but also on the previous input level in the device, a process that requires multiple stages. To perform the XOR function of Boolean logic, sequences of signals are applied to the device's source and drain electrodes. The logic function should begin with IN1 to define the device's state, followed by IN2 to operate the XOR logic and perform a nondestructive read-out defined as OUT. Ten repeatable cycles of executing the XOR function are depicted in Figure 4-9a, demonstrating the reliability of our artificial neural transistors.

As an example, the fifth cycle is chosen as presented in Figure 4-9b. For IN1, a voltage of 20 V is deemed to be 1, while a voltage of -10 V is considered to be 0. IN2's 0 and 1 are determined by two voltages, 2 V and -2 V, respectively. Additionally, the current from IN2 is used as an output, with a value greater than the threshold (1 nA) corresponding to a "1" and a value less than the threshold corresponding to a "0". When 20 V is imposed on the device (IN1=1), the ferroelectric domain is aligned by the external electric field, the IN2=0 and 1 will lead to OUT=1 and 0, respectively. After a -10 V voltage applied, the ferroelectric polarity of α-In_2Se_3 is reversed, and the opposite output result can be obtained. The results demonstrate that the XOR operation can be performed successfully in a single artificial neural transistor based on 2D ferroelectric material with repeatable and stable performance. In comparison to traditional CMOS design, which typically requires six devices, our method has the potential to considerably reduce the size of the logic circuit.

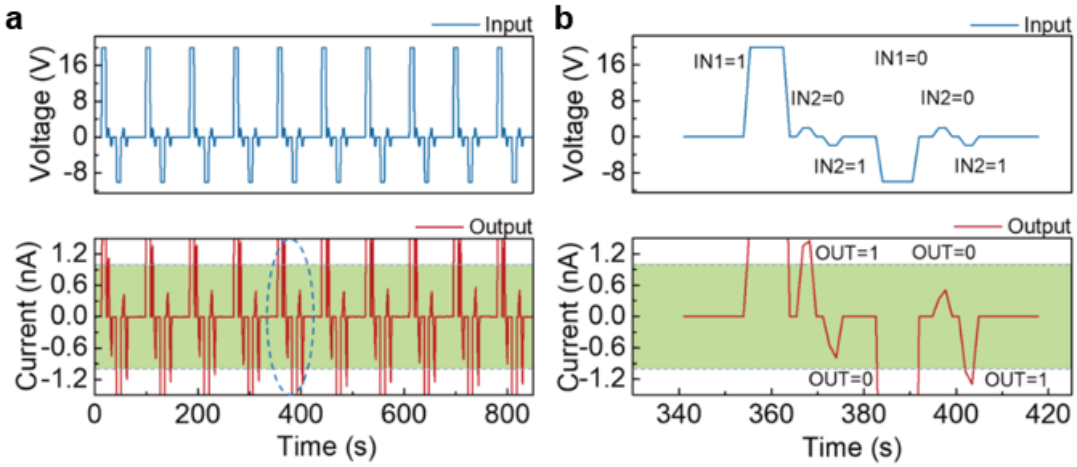

Figure 4-9 a) Demonstration of 10 cycles to execute the XOR logic. In top panel, the drain voltage represents the input, and the drain current represents the output in lower panel. b) The fifth cycle is chosen as an example to demonstrate the details

4.4.2 linearly separable logic

In addition to linearly nonseparable logic, linearly separable logic gates such as AND, OR, and NOT logic gates are implemented in our designed device. Unlike conventional insulating oxide ferroelectric materials with a broad energy band, semiconducting nature of α-In_2Se_3 and 1.4 eV band gap enable it to function as a FET channel, and its performance can be controlled by illumination. On the basis of the combinational logic principle, Figure 4-10 illustrates the implementation of AND and OR logic gates with photoswitchable outputs.[168] In this case, 6 V and 0 V of V_{DS} are defined as 1 and 0, respectively for IN1, whereas applying 3 V of gate voltage or not is defined as 1 or 0 for IN2. To read the output, a bias voltage of 1 V is applied to V_{DS}. For clearly distinguished, the blue line denotes the AND logic function, whereas the red line represents the OR logic gate. The 2 nA of threshold is determined for the two types of logic discussed above. In the dark, the AND logic function is performed, and the output current is greater than the threshold value only if both IN1 and IN2 are equal to 1. Under illumination, with the help of photogenerated carriers, only one of them has an input value of 1, resulting in an output value of 1. Compared to the case in dark, the photocurrent caused by V_{DS} is

greater than that of the gate voltage, implying that the channel voltage is more suitable for separating photogenerated carriers.

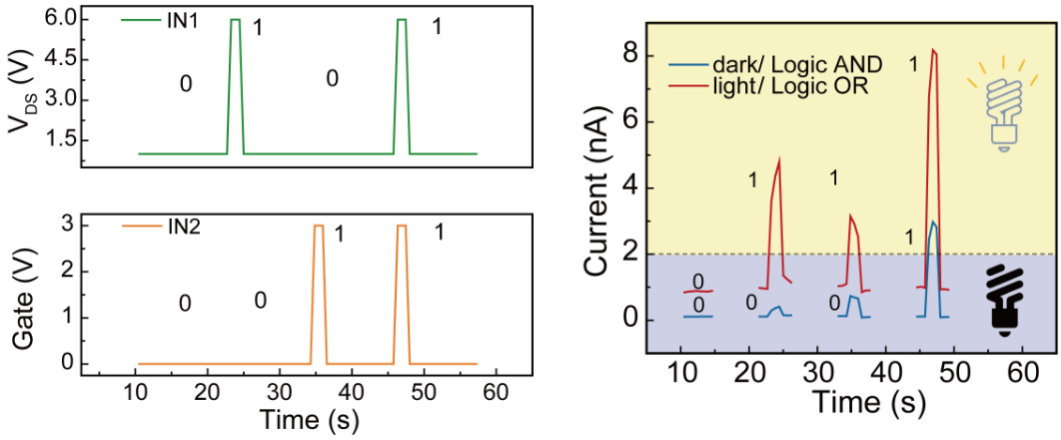

Figure 4-10 The two panels on the left represent the input IN1 and IN2. The panel on the right depicts that the device can perform OR logic under illumination, while in the dark the device is switched to AND mode

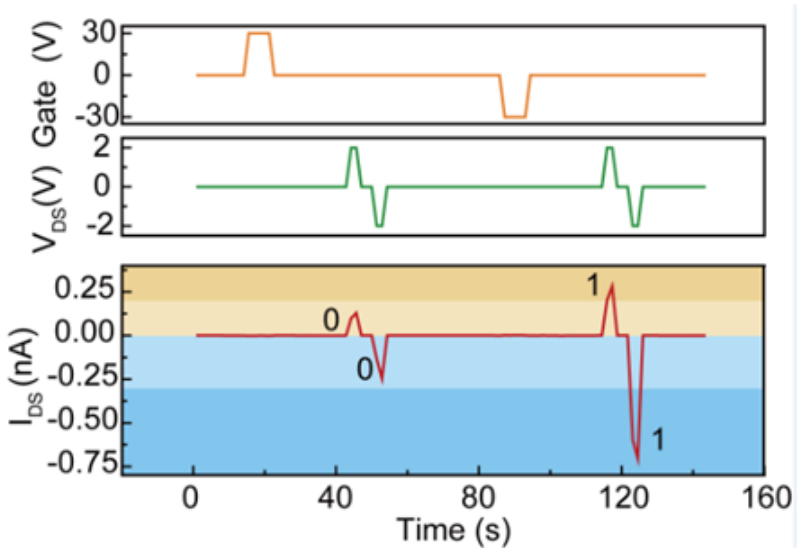

Figure 4-11 The gate voltage is defined as the input and the V_{DS} is used to read the output (I_{DS}) to demonstrate the NOT logic

The NOT logic gate is demonstrated in Figure 4-11, where 30 V gate voltage is defined as 1, -30 V as 0, and 2 V of V_{DS} is used to read the output value. When a 1of

gate terminal is input, an output value of 0 is obtained, conversely, if a 0 is input, a 1 is obtained, thus achieving the NOT logic in the device. It's worth noting that if the read voltage is set to -2 V, the equivalent function will be executed. The implementation of NOT logic gate can be attributed to capacity of the OOP ferroelectricity to control the channel conductance, as discussed in Figure 4-5.

4.5 Synaptic behaviors

As the terminal of a nerve cell, a synapse is responsible for connecting neurons to form neural networks. The weight of a synaptic connection indicates how firmly two neurons are coupled, or how much influence one neuron can apply on another. Synaptic weights are plastic and can be increased or decreased in response to neuronal activity, resulting in memory and forgetting in the brain. In a neural network, a synapse connects many neuronal terminals. Figure 4-12a illustrates a schematic diagram of synaptic connections, in which the pre-synapse delivers signals to the post-synapse by the release of neurotransmitters; the synapse can also act as a modulator, controlling the activity of neighboring synapses. Similar to a synapse of neuron, the source and drain electrodes serve as the pre- and post-terminals, respectively, while the gate electrode serves as both a pre-synapse as well as a modulator in our proposed device (Figure 4-12b).

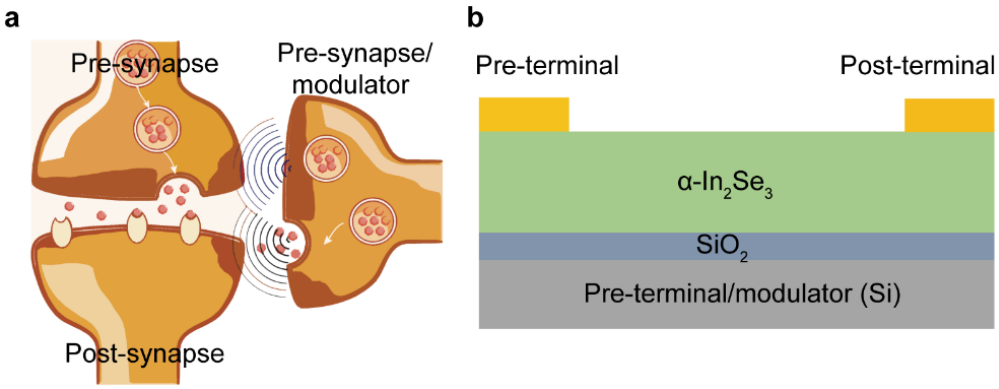

Figure 4-12 a) A schematic diagram of three-terminal biological synapse. b) The side-view of device structure

Synaptic plasticity can be classified into short- and long-term memory (STM and LTM) in terms of time, the transition from STM to LTM depicted in Figure 4-13a. The postsynaptic current (PSC) is used to determine the synaptic weight. The figure illustrates a large increase in PSC following the application of a series of electrical pulses (5 V, 270 ms). When the number of electrical pulses is increased from 10 to 30, the PSC can be sustained at a greater value for an extended length of time, indicating that the electrical stimulus is capable of modulating synaptic weights effectively. To mimic synaptic dynamics such as long-term potentiation/inhibition (LTP/LTD), the conductance state of the device channel is dynamically modulated by switching the ferroelectric domains of α-In_2Se_3. As presented in Figure 4-13b, there is a noticeable rise in conductance from 142 to 290 pS following 50 successive electrical pulses (6 V, 270 ms), and 50 discrete conductance states are achieved during the LTP process. When -3 V electrical pulses are applied to the channel of

device, the polarity of some ferroelectric domains is reversed, resulting in decreased conductance.

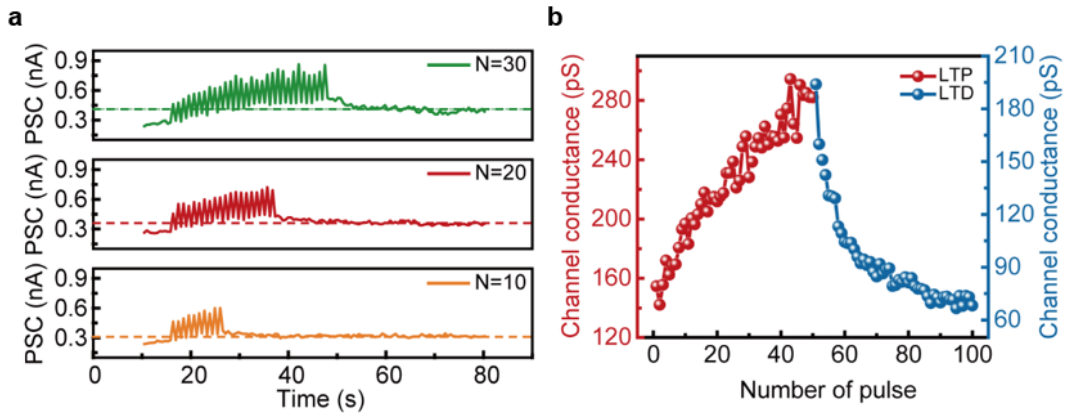

Figure 4-13 a) The PSC triggered by 10, 20 and 30 consecutive V_{DS} electrical pulses (5 V, 270 ms), a 2 V voltage is set as bias. b) Long-term potentiation and depression are obtained by applying 50 consecutive 6 V and -3 V electrical pulses at the source and drain electrodes, respectively

Additionally, the capacity of bottom gate to modulate the conductance of channel was investigated using a variety of different amplitudes of electrical pulses based on the OOP ferroelectricity of α-In_2Se_3, as seen in Figure 4-14. To observe the channel conductance variation, a 2 V voltage was applied to the source and drain electrodes and the PSC values were read. After 10 positive electrical stimuli from the gate electrode, there is a little decrease in PSC; however, when negative gate voltages are applied, there is an increase in PSC, which is caused by the inversion of OOP polarization direction.

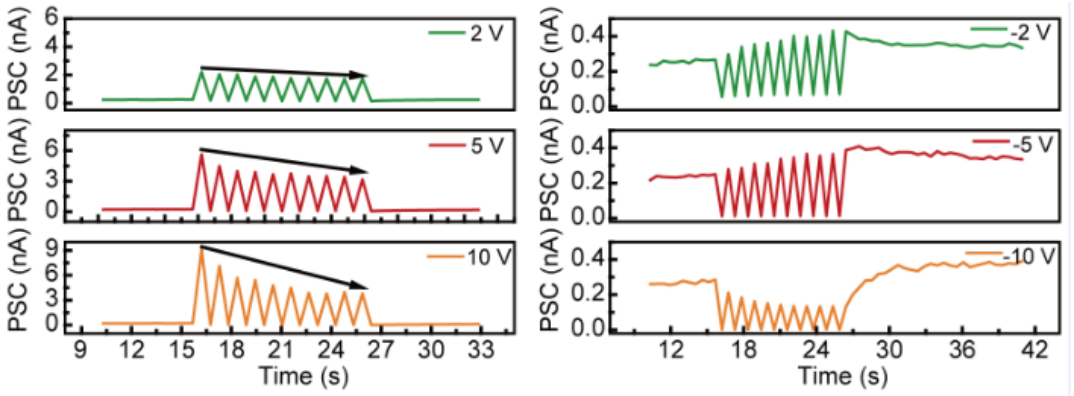

Figure 4-14 The PSC triggered by 10 gate electrical pulses from 2 V to 10 V and -2 V to -10 V, V_{DS} is set to 2 V

4.6 Artificial neural network

The crossbar, as a hardware-based artificial neural network (ANN), is a promising candidate for overcoming the von Neumann computer's bottleneck by minimizing data transmission between processors and memory. Figure 4-15a shows the schematic diagram of a crossbar, where the input terminals represent the input layer in an ANN, the output terminals represent the output layer, and the conductance of the neural device channel serves as the weight. When an external voltage is applied to the programmable neural device, the crossbar emulates the behavior of the biological neural network due to the additive nature of the current, and the weights in ANN are also changed simultaneously. To verify the reliability of the crossbar established by our proposed device, an ANN was constructed using the experimentally determined LTP/LTD characteristics. Crossbar operation and performance are simulated and analyzed using the CrossSim platform, as seen in Figure 4-15b.[169] A recognition accuracy of approximately 85 percent can be obtained

for both small and MNIST handwritten digits images, indicating the feasibility of crossbars based on ferroelectric α-In_2Se_3 (Figure 4-15c,d).

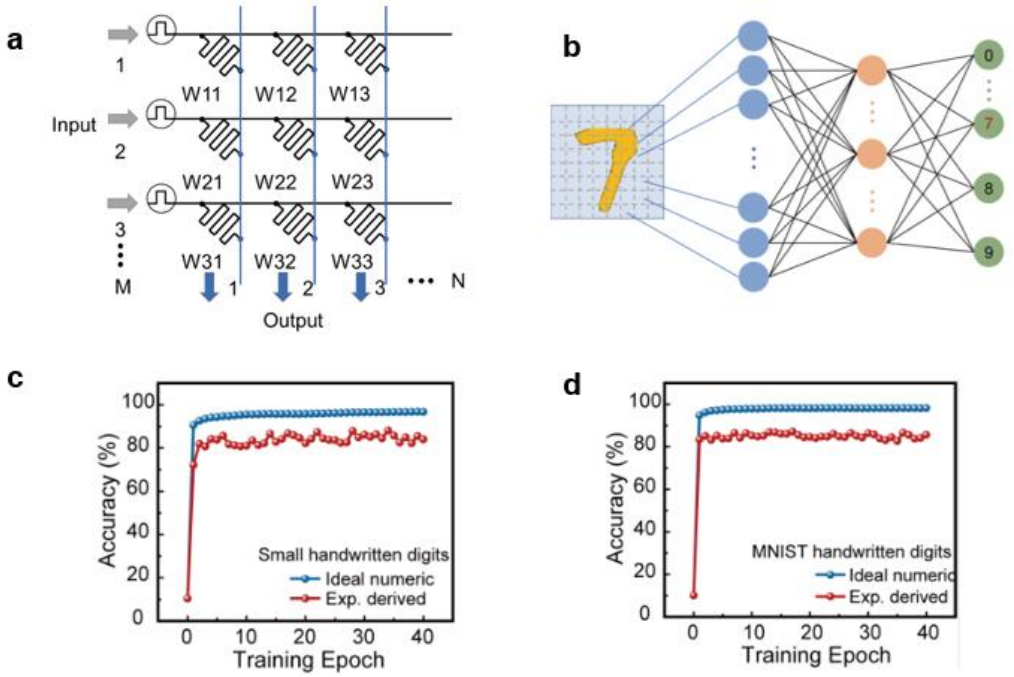

Figure 4-15 a) The principle of crossbar based on our device, where the conductance of the channel is defined as the weight of the synapses. b) A three-layer ANN is built for image recognition based on our proposed device. Accuracy rate of c) small digit image and d) MNIST digit image as a function of training epoch

4.7 Emulation of controlling food intake

Controlling food intake is a critical ability for biological survival since it helps maintain energy balance, but its complexity involves close collaboration between the central nervous system, many organs, and hormones. In a starving state, fat is broken into free fatty acids to stimulate the central nervous system; at the same time, the brain has a low level of pleasure, which promotes food-seeking behavior. Food can

contribute to eliciting a sensation of reward and enhancing our sense of satisfaction. Consumption of food also stimulates the pancreas to release insulin, which enters the brain via circulation and inhibits energy intake. It is self-evident that the brain's satiety information reduces the degree of pleasure associated with stopping eating. Thus, food intake as the only stimulus can provide both positive and negative feedback in states of hunger and satiety, depending on the degree of pleasure experienced. The varied gate voltages in this work indicate the condition of hunger or satiety, and the current modulated by the gate voltage in the device channel represents the brain's level of pleasure. To measure the I_{DS}, a 2 V voltage was applied to the source and drain electrodes, followed by ten successive 6 V electrical pulses to simulate the effect of food on the central nervous system.

As presented in Figure 4-16a, when the gate voltage is -5 V, only a low I_{DS} is observed, indicating a state of starvation with a low degree of pleasure. When electrical pulses representing food are applied to the channel, the current increases to 1.55 times, and the increased pleasure in the brain encourages the search for additional food. However, as the gate voltage is increased from -5 V to 2 V, the variation in channel current induced by the electrical pulses becomes less noticeable, which simulates the process of gradual satiation of humans (Figure 4-16b, c). When the gate voltage is greater than 5 V, negative feedback can be obtained following the application of electrical stimuli, indicating that eating too much food causes the brain to experience discomfort, as illustrated in Figure 4-16d, e. The interconversion

process depicted in Figure 4-16f shows how energy homeostasis is dynamically established through the combined influence of positive and negative feedback on the brain. As discussed above, the successful emulation of food intake control is due to the increase in channel conductance caused by inversion of IP ferroelectric polarity and the modulating influence of OOP ferroelectricity on channel conductance. The results demonstrate that it is possible to integrate complicated nervous system-level functionalities in a single artificial neuron with a compact device architecture.

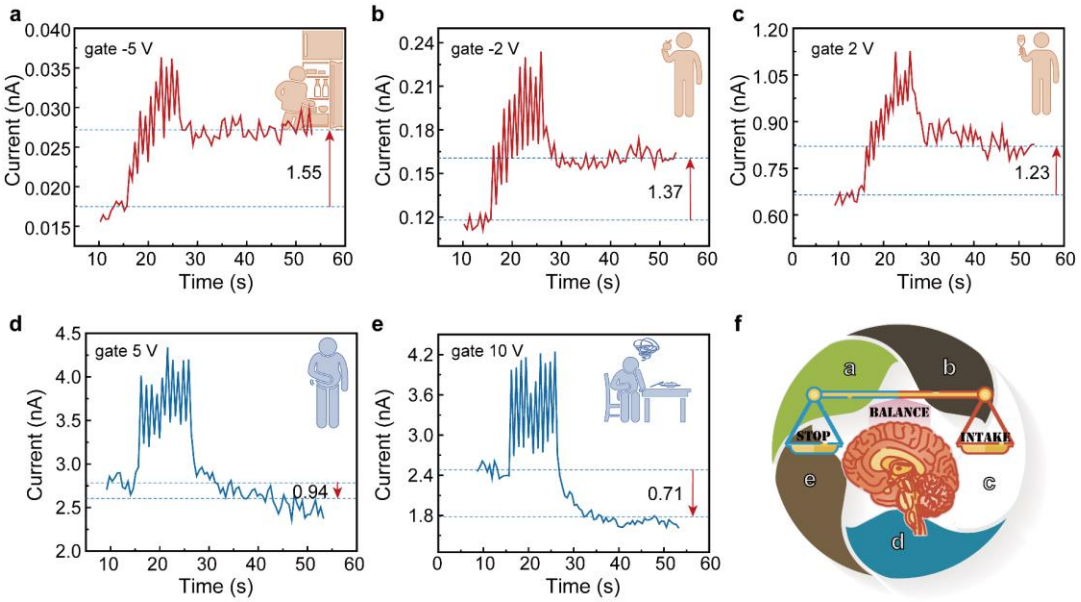

Figure 4-16 Emulation of controlling food intake. The variation of the drain current is observed after 10 electrical pulses of 6 V applied under different gate bias voltages a) -5 V, b) -2 V, c) 2 V, d) 5 V, e) 10 V. f) A diagram to illustrate the principle of controlling food intake in the brain to maintain energy homeostasis

4.8 Summary

In summary, an artificial neuronal electronic device based on 2D vdW ferroelectric α-In_2Se_3 was carefully designed to mimic the complicated behaviors of cortical neurons in the human brain. Due to the robust ferroelectricity, artificial neurons can classify linearly separable and nonseparable inputs at the single device level, rather than through a multilayered neural network. In comparison to the conventional CMOS design, the XOR logic gate, which operates based on the stateful logic by reversing the IP ferroelectric polarity, effectively conserves transistor resources. Additionally, this single electronic device integrates linearly separable logic functions such as AND, OR, and NOT. Beyond logical functions, essential behaviors of biological neuron are demonstrated, and unlike other three-terminal neural devices, the gate terminal in our designed device can not only serve as a pre-synapse but also modulate the weights of other synapses. An ANN was built to simulate the performance of the crossbar made up of our artificial neurons for image recognition to demonstrate the reliability of device. More importantly, for the first time, control of food intake as a nervous system-level complicated behavior was successfully emulated using ferroelectricity in α-In_2Se_3. The results present a significant step toward effectively simplifying current artificial neural networks in order to overcome the von Neumann bottleneck and offer a flexible strategy for AI to handle real-world problems.

Chapter 5 Multifunctional Optoelectronic Synapse Based on 2D Ferroelectric Material

5.1 Introduction

Artificial visual systems have been applied to image recognition, autonomous vehicle driving, and robotics, all of which require not only the conversion of light signals to internal information, but also the processing and rapid response to sensor inputs.[170-173] In general, vision sensors such as charge-coupled device (CCD) cameras or complementary metal-oxide silicon (CMOS) imagers transform external light inputs to electrical signals for image identification using neural network algorithms in the computer.[174] This means that the processors and memories of current artificial visual systems are unable to respond directly to external light stimuli, and signal conversion and transmission in the vision sensor cost additional energy and introduce signal latency. As a result, there is a great need for multifunctional artificial visual devices that combine vision, data storage, and processing into a single device capable of handling complex tasks. Additionally, because von Neumann computers have a separated processing unit and memory, it is difficult for current artificial visual systems to implement real-time and accurate processing of continuous, high-throughput input signals generated by vision sensors while consuming minimal energy.[175] In comparison, the human visual system, which is composed of the retina, optic nerve, and visual cortex, is remarkably flexible and sophisticated. After the retina processes visual signals, the optic nerve transmits them

to the visual cortex, where visual information can be processed in parallel and responded to in real time with a great degree of efficiency and elegance. As with other bionics success stories,[176] an artificial visual system that mimics humans presents a reasonable alternative for visual signal processing.

As a result, much effort has been devoted on constructing artificial visual devices that mimic biological neural behaviors such as synaptic short-term plasticity (STP) and long-term plasticity (LTP).[155, 177] Photonic synaptic behaviors such as light signal interpretation and extraction of pertinent information such as intensity and frequency have been achieved in an optoelectronic synaptic device via the photogating effect or persistent photoconductivity phenomenon.[144, 156, 178, 179] For example, a fully photon modulated device based on a ZnO/PbS heterostructure and a solar-blind SnO_2 nanowire photosynapse have been proposed to emulate plasticity functions.[180, 181] Apart from traditional semiconductors, researchers have been attracted by two-dimensional (2D) layered materials due to their superior optoelectronic capabilities since the discovery of graphene and transition metal dichalcogenides (TMDs).[182-184] Photogating effect is easily realized in 2D materials-based optoelectronic synaptic devices since there are no concerns about lattice mismatching in van der Waals (vdW) heterostructures.

However, currently the most of proposed optoelectronic synaptic devices only mimic the synapses that connect neurons, and few previous works have attempted to functionalize them beyond their synaptic behaviors, such as by integrating them with

data storage and processing functions similar to those found in human visual cortex. Additionally, the optoelectronic synaptic device with a simple structure may be a powerful option for future emulation of more complicated neural systems. For decades, ferroelectric materials based on conventional oxides with spontaneous electric polarizations have been extensively employed in memory and logic circuits. Unique ferroelectricity adds another degree of freedom for device functionalization, and synapses made of conventional ferroelectrics and 2D materials have also been explored.[77, 156] Nonetheless, the oxide ferroelectrics' low conductivity and broad energy band gap restrict their application in optoelectronic synapses. Fortunately, the recent discovery of semiconducting vdW layered α-In_2Se_3 with a narrow band gap of 1.4 eV demonstrates robust ferroelectricity at room temperature and even at the atomic scale, allowing for efficient visual perception and emulating the complete human visual system.

Here, an optoelectronic synaptic (OES) device based on n-type ferroelectric α-In_2Se_3 and p-type 2D material GaSe heterostructure is developed, which includes biological behaviors of synapse, memory, and logic functions. Mimicking the retinal and electrical synapses enables the detection of light stimuli and the transmission of electrical stimuli, respectively. Additionally, the success of well-known Pavlovian classical conditioning experiments designed to mimic associative learning in the human brain indicates that the OES device is completely capable of processing multiple input signals. Furthermore, the development of logic and memory

capabilities enables optical sensing and neuromorphic visual cortex functions to be combined into a single device for multifunctionality.

5.2 Design of the device

5.2.1 Experimental methods

Device Fabrication: Ti/Au (10 nm/50 nm) metal electrodes were prepared on Si/SiO_2 (300 nm) substrates by a standard lithography technique and E-beam. Mechanical exfoliation was used to produce α-In_2Se_3 and GaSe nanosheets from their bulk counterparts purchased from HQ Graphene company. To construct α-In_2Se_3/GaSe vdW heterostructures, nanosheets of α-In_2Se_3 were placed on source and drain electrodes, and then GaSe nanosheets were transferred to connect α-In_2Se_3 channels and gate electrodes, the fabrication processes were carried out by a dry transfer system equipped with a microscope.

Characterizations: Raman and PL spectra of the material were obtained by WITEC_Confocal Raman system with a 532 nm laser at room temperature, and the laser intensity was set to less than 1 mW for avoiding causing damage. Ferroelectricity was confirmed by PFM images of α-In_2Se_3 on a conductive Pt substrate using Asylum MFP 3D Infinity. The transmission electron microscope (TEM) image from Jeol JEM-2100F were used to analyze the lattice structure of α-In_2Se_3. Electrical characteristics were measured by Keithley 4200 in quiet mode. A waveform generator (Keithley 3390) was applied to produce light pulses. The power density of LED and lasers were calibrated by a power meter (Sanwa).

Neural Network Simulations: The program code was written in Python and combined with the neuron cores provided by the CrossSim platform. The program ran under Spyder, a free integrated development environment (IDE).

5.2.2 Structure of device and material characterization

A biological synapse is the most essential component of a brain neural network, sending excitatory signals from the presynaptic terminal to the postsynaptic terminal via chemical neurotransmitters.[185] The timing and strength of spikes can affect the tightness of the connection, referred as synaptic weight. Synapses transfer electrical signals generated by the retina in response to light stimuli to the visual cortex of the brain for information storage and signal processing in the human visual system (Figure 5-1a).[186] The purpose of this study was to develop a vdW-hybrid synaptic three-terminal device capable of successfully mimicking the entire biological visual system's response to external light stimuli as well as the processing of input signals with outstanding synaptic features. The OES device structure is displayed in Figure 5-1b, where three Au electrodes were first produced on a Si/SiO_2 substrate, with the source and drain specified as presynaptic and postsynaptic terminals, respectively, and another employed as a top gate. Prior to connecting the channel and top gate with GaSe, α-In_2Se_3 was deposited as a channel on the source and drain electrodes using dry transfer for the purpose of transferring synaptic excitation.

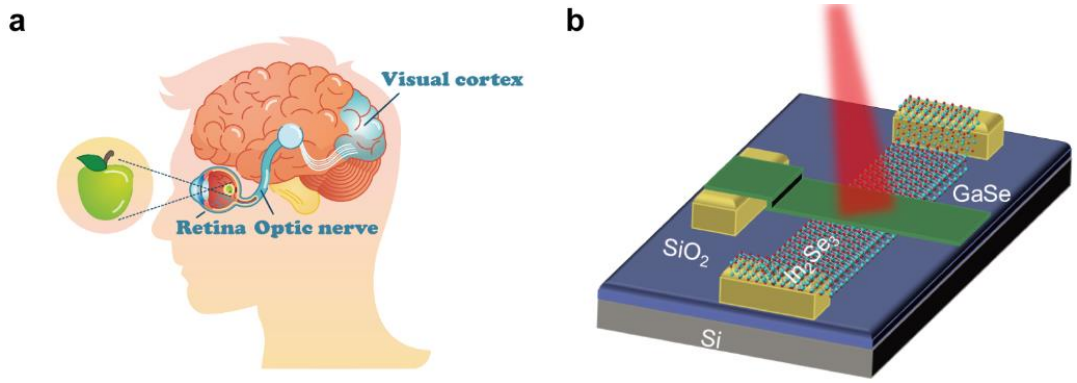

Figure 5-1 a) Schematic of entire biological visual system. b) The structure of proposed multifunctional optoelectronic synaptic device

Ferroelectric materials have been widely used as memory devices, pressure sensors, and photovoltaic solar cells due to its intrinsic spontaneous polarization.[187] [3, 188] Due to the critical thickness problem, it is difficult to sustain Moore's law with the downsizing of devices made of conventional oxide dominated ferroelectric materials.[189] The development of 2D vdW ferroelectric materials offers a solution to the challenge. Unlike other 2D ferroelectric materials, which only display reversible spontaneous electric polarization in pure in-plane (IP) or out-of-plane (OOP) orientations at room temperature, semiconducting α-In_2Se_3 exhibits it in both IP and OOP orientations.[49, 162, 163, 190] The close coupling between the IP and OOP polarizations is attributed to the lateral displacement of the central Se atomic layer generated by an external electric field. Additionally, the ferroelectric α-In_2Se_3 exhibits two distinct stacking modes, rhombohedral (3R) and hexagonal (2H), as illustrated in Figure 5-2a, which belong to the space groups R3m and P63/mmc,

respectively.[165] According to the high-resolution side-view TEM images (Figure 5-2b) and the crystal structure model, the α-In_2Se_3 used in this study is the 3R mode.

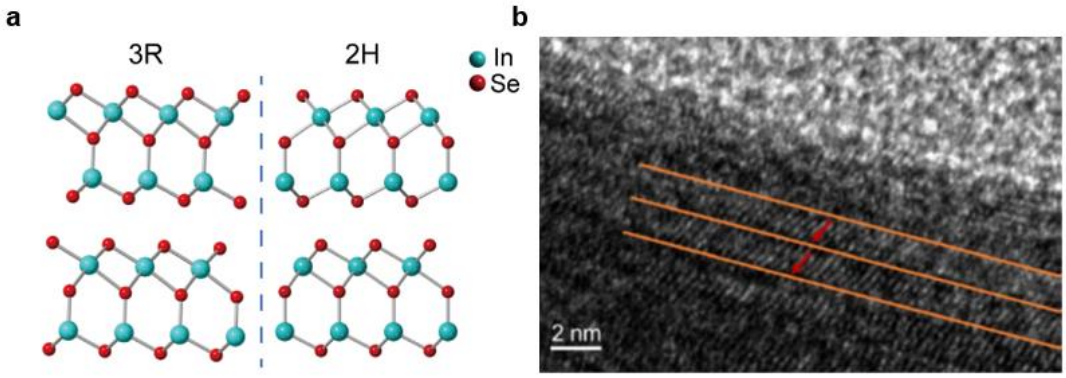

Figure 5-2 a) Two different stacking modes of ferroelectric α-In_2Se_3: rhombohedral (3R) structure and hexagonal (2H). b) TEM of a side-view α-In_2Se_3 nanosheet

To investigate the ferroelectricity of α-In_2Se_3, a nanosheet exfoliated from the bulk was transferred to a conductive Pt substrate and the amplitude and phase were measured using piezoresponse force microscopy (PFM), which were determined by the magnitude of the local piezoelectric response and the polarization orientation of the ferroelectric domain, respectively. The topography, phase, and amplitude images acquired using Dual AC Resonance-Tracking (DART) mode of PFM demonstrate a clear phase and amplitude difference in the area marked by the arrow. The change in amplitude and phase at the locations of the arrows is obvious in Figure 5-3a. Additionally, piezoelectric and amplitude loops are typical ferroelectric material behaviors that show the dynamic process of ferroelectric domain reversal. The sharp shift in polarity observed in parallelogram-like piezoelectric response loops and

butterfly-like amplitude loops suggests that the polarity is driven up or down by the writing voltage (Figure 5-3b). In summary, the PFM measurements and crystal structure analyses performed in this work indicate that the α-In_2Se_3 nanosheets employed in this investigation are intrinsically ferroelectric.

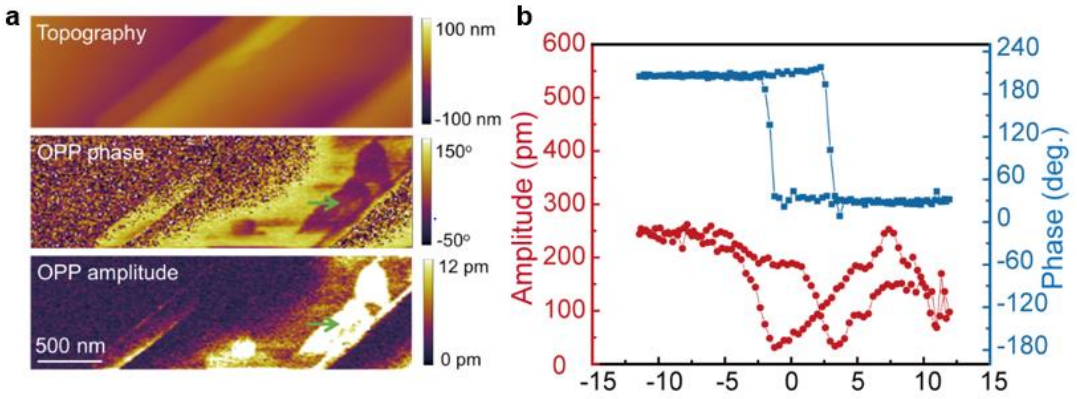

Figure 5-3 a) Topography, OOP PFM phase and OOP PFM amplitude images show opposite domain orientation (arrow location), scale bar is 500 nm. b) PFM phase and PFM amplitude hysteresis loops of α-In_2Se_3 on Pt substrate indicate the switchable ferroelectric nature under external voltage

For determining the light absorption capability of α-In_2Se_3 and GaSe, photoluminescence (PL) spectra were obtained using a 532 nm laser. To avoid damaging the 2D materials, the laser power was set to 1 mW. According to Figure 5-4a, b, the PL peak of α-In_2Se_3 is 870 nm, whereas the GaSe peak is 620 nm, showing that the hybrid structure of device can absorb both visible and near-infrared light.

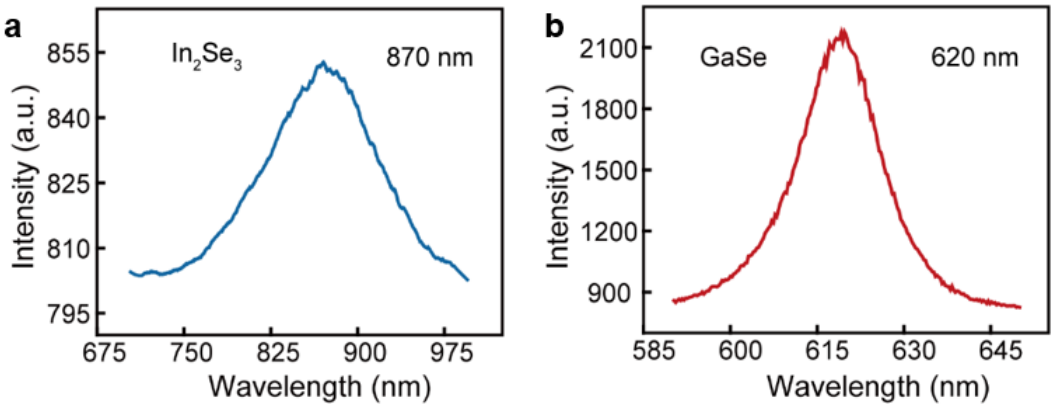

Figure 5-4 PL spectra of a) α-In_2Se_3 and b) GaSe under 532 nm laser

5.3 Mimicking the behaviors of biological synapse

5.3.1 Emulation of optic nerve

The optic nerve structure and a schematic diagram of the OES device are depicted in Figure 5-5a, b. When the presynaptic neuron is excited, neurotransmitters are released into the postsynaptic neuron, and its concentration affects whether the postsynaptic neuron generates postsynaptic current (PSC) or not. The weight of a synapse represents the strength of the connections between neurons, and it may change in response to neuronal activity, a phenomenon known as synaptic plasticity. Between the source and drain electrodes, the channel conductance is defined as the synaptic weight that may be modulated by electrical and light inputs. The following section illustrates the electrical synaptic behaviors.

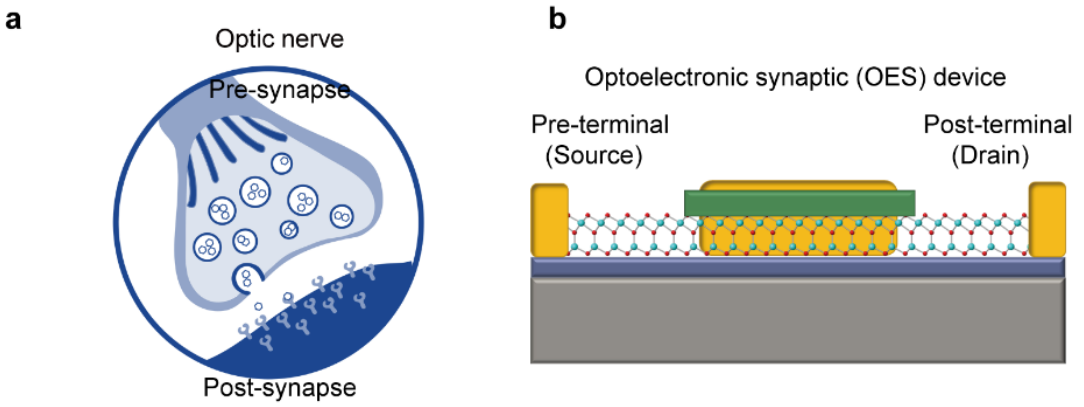

Figure 5-5 a) Schematic of optic nerve and b) A side-view diagram of the OES device

Paired-pulse facilitation (PPF) is a kind of short-term synaptic plasticity that describes the effect of two successive spikes on synaptic weights. The device is triggered by two electrical pulses (2 V, width 90 ms, interval 270 ms) in the inset of Figure 5-6, and the PSC generated by the second electrical pulse is much higher, suggesting considerable facilitation. The PPF index can be calculated as the ratio of two PSCs, i.e. PPF index = [(A2-A1)/A1]×100 %. As seen in figure, the PPF index can reach up to 41% when the interval duration is minimum, and the index drops exponentially with increasing interval time. The behavior is similar to that of enhancing neurotransmitter release in a synapse.

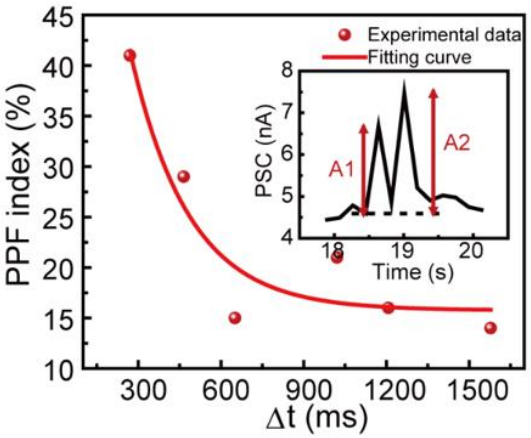

Figure 5-6 PPF index as a function of electrical pulse interval time Δt, the fitting curve shows that PPF decreases exponentially with the increase of Δt. The inset displays PSC triggered by two consecutive electrical pulses; A is defined as the amplitudes of PSC

The switch of ferroelectric polarization (P_{FE}) can be used to control the electrical characteristics of the material. Thus, the conductance of OES devices using ferroelectric semiconductor as the channel can be controlled by modulating the amplitude of the electrical pulses. It is used to switch the domains of α-In_2Se_3, mimicking synaptic dynamics such as long-term potentiation/depression (LTP/LTD). As seen in Figure 5-7, the conductance of the device channel increases from 6.21 to 9.70 nS after 20 consecutive electrical pulses (1 V, width 175 ms), and the LTP process exhibits 20 discrete conductance states. When negative voltage pulses were applied during LTD, orientations of some domains were reversed, resulting in a gradual decrease in conductance. To quantify and examine the performance of OES devices, we extracted nonlinearity (NL), cycle to cycle variation (cyc), and symmetry from the above LTP/LTD curves. The NL and cyc values were calculated by fitting the LTP/LTD curves using Equations below,[191] where G_{LTP} and G_{LTD} denote the conductance of the LTP and LTD curves, respectively. The number of pulses applied is denoted by P, while the highest value is represented by P_{max}. Additionally, G_{min} and G_{max} are the minimal and maximum conductance values. A indicates the magnitude of the nonlinearity in the LTP/LTD curve. Furthermore, because the symmetry is defined as LTD NL/LTP NL, the ideal symmetry is 1.

$$G_{LTP} = B\left(1 - e^{\left(-\frac{P}{A}\right)}\right) + G_{min} \quad (5\text{-}1)$$

$$G_{LTD} = -B\left(1 - e^{\left(\frac{P-P_{max}}{A}\right)}\right) + G_{max} \quad (5\text{-}2)$$

$$B = (G_{max} - G_{min})/\left(1 - e^{\frac{-P_{max}}{A}}\right) \quad (5\text{-}3)$$

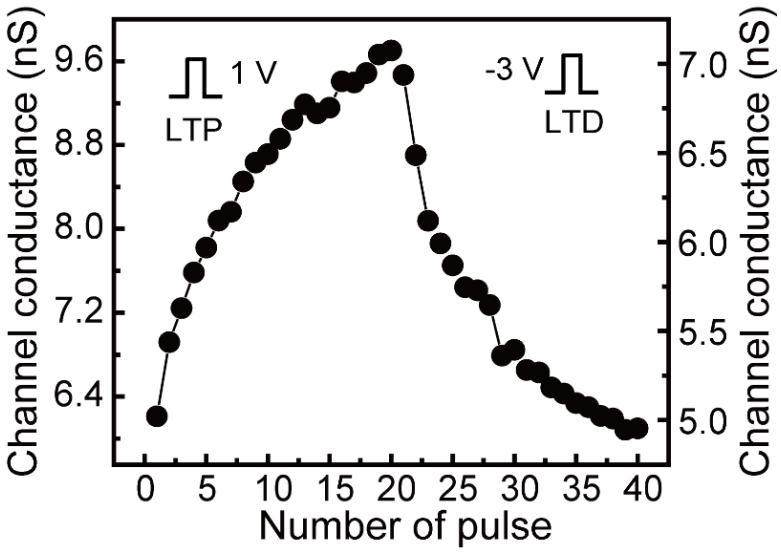

Figure 5-7 LTP and LTD operations under 1 V (175 ms) as well as -3 V (175 ms) 20 applied pulses, respectively

Here, 20 consecutive 1 V and -3 V voltages applied as an example has been shown in the Figure 5-7 named as case1. Additionally, the 2 V, -4 V (case 2) and 3 V, -5 V (case 3) voltages are also determined. The details are presented in the radar plot (Figure 5-8a), which demonstrates that all NLs remain below 4, with a minimum value of 2.21, that is very close to the ideal value of 1. Moreover, regardless of the amplitude of the electrical pulse, cycs are always less than 2% and the maximum symmetry value is less than 1.6, indicating that the performance of device does not change significantly with applied voltage, which is advantageous for reducing noise

interference caused by read and write voltages. To increase the accuracy of hardware-based neural networks, 100 electrical pulses were applied to the OES device, as illustrated in Figure 5-8b. When compared to 20 consecutive pulses, the increased number of pulses has no obvious influence on the performance of device, and the related parameters will be explored and applied in the following part regarding the neuromorphic computing simulation.

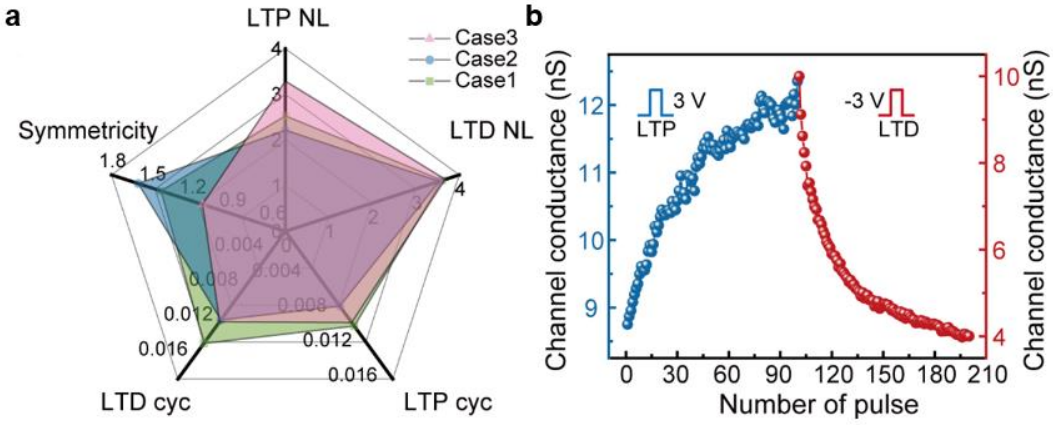

Figure 5-8 a) Nonlinearity (NL), cycle to cycle variation (cyc) and symmetry of LTP and LTD under different cases: case1(1 V, -3 V), case2 (2 V, -4 V), case3 (3 V, -5 V). b) LTP and LTD operations under 3 V (175 ms) as well as -3 V (175 ms) 100 applied pulses, respectively

5.3.2 Photonic synapse mimicking the retina

Figure 5-9a depicts the working mechanism of retina schematically. Light stimuli were used to explore the response of a photonic synapse that mimics the retina (Figure 5-9b). When the OES device was subjected to a light pulse, an increase in conductance was seen, exactly as the retina can translate visible light into neuronal

excitement. When the light stimulus was removed, the conductance declined over time due to the photogating effect of the α-In_2Se_3/GaSe heterostructure.

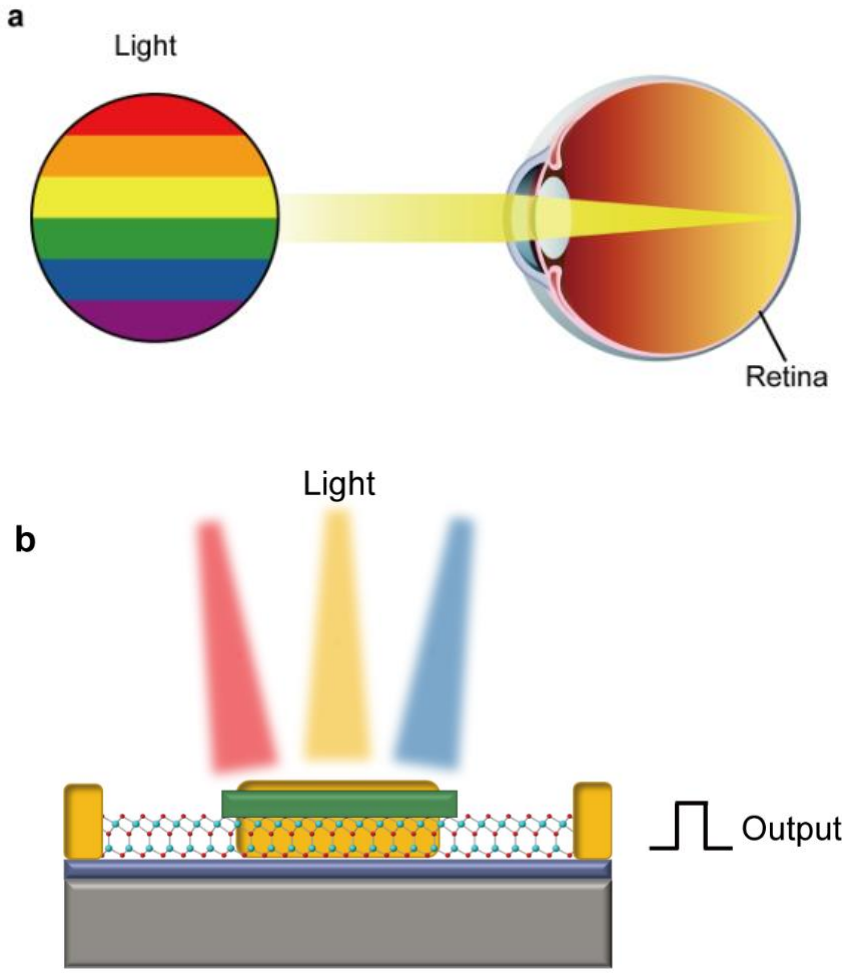

Figure 5-9 a) Working mechanism of the retina. b) Schematic of OES device under light pulses to mimics the retina

As shown in Figure 5-10a, b, the PSC produced by the second optical stimulus is much greater than that of the first, and the PPF index declines exponentially to a low value as the time interval between the two stimuli increase. It is worth noting that the OES device has a longer decay period when exposed to light pulses than subjected to electrical pulses due to two distinct mechanisms. The one is induced by

the reversal of ferroelectric domains, whereas the other is caused by the photogating effect.

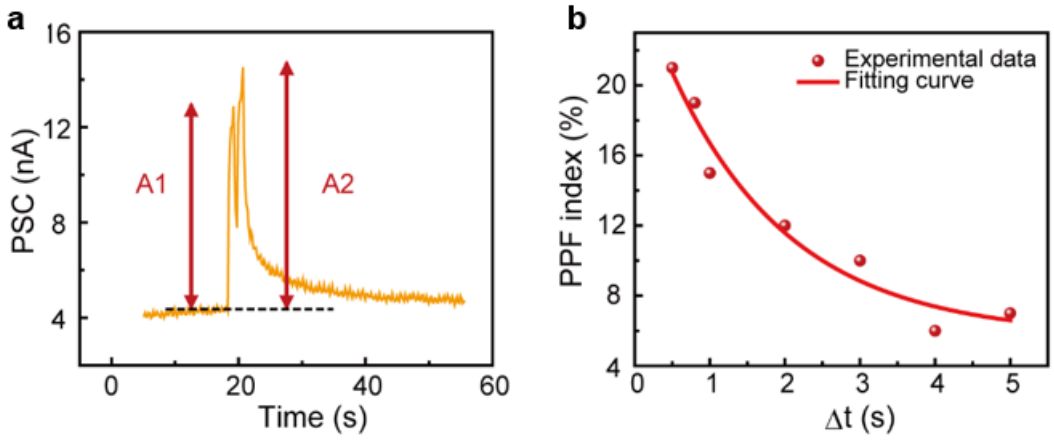

Figure 5-10 a) The PSCs triggered by a pair of light pulses (808 nm wavelength, 7.8 mW cm^{-2}, width 1 s) with Δt=0.5 s. b) PPF index as a function of light pulse interval time Δt

Figure 5-11 displays the evolution of the PSC of the OES device over time when exposed to 5, 10, and 20 light pulses, respectively (808 nm wavelength, 5.7 mW cm^{-2}, 1 s). There is no doubting that the PSC grows as the number of light pulses increases and the decay period becomes longer. This is similar with the phenomena known as persistence of vision, which describes the fact that an image stays in the biological visual system for a period of time following the removal of a light stimulus and served as the inspiration for the development of cinema.

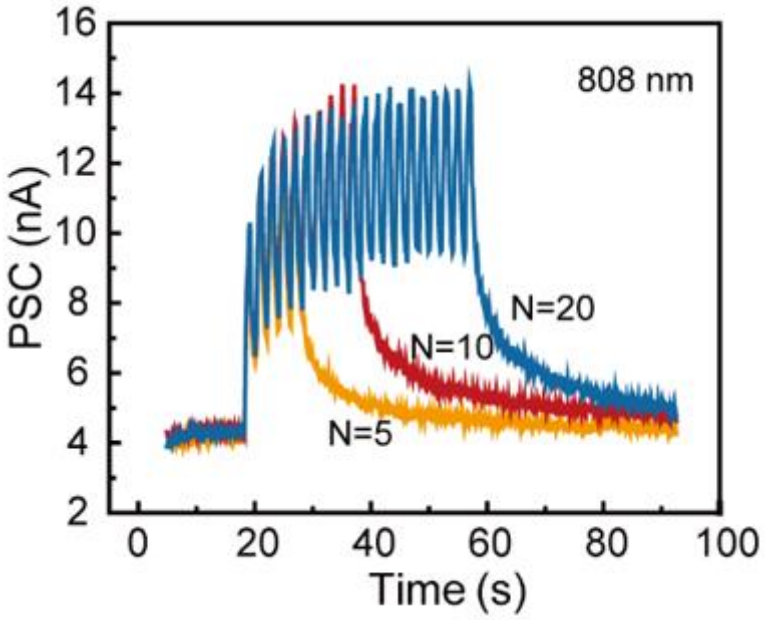

Figure 5-11 The PSC triggered by 5, 10 and 20 consecutive light pulses (808 nm wavelength, 5.7 mW cm^{-2}, 1 s)

The biological retina not only converts light stimuli into electrical signals, but also identifies different colors, which is referred to as wavelength selectivity. However, the majority of current artificial optoelectronic synapses only respond to the density, number, and duration of light pulses. To perform color recognition with traditional vision sensors, additional accessories are generally necessary.[192, 193] In this case, the OES device combines the capabilities of sensing and color recognition. To investigate the operation of OES devices, light pulses of 450 nm, 808 nm, and 980 nm with the same density of 5.7 mW cm^{-2} were used. As illustrated in Figure 5-12a, when a 450 nm light pulse is applied to the OES device, the photocurrent rapidly saturates and can reach up to 52 nA, which is significantly higher than the 808 nm example (Figure 5-12b). Additionally, there is almost no photogenerated current

measured at 980 nm (Figure 5-12c). According to the PL spectra and the energy band structure of p-n junction (Figure 5-12d-f), the distinct PSC patterns are mostly attributable to the two materials' different absorption capacities at different light wavelengths. Thus, the perceptive capability of the biological retina with color recognition is successfully implemented in this OES device.

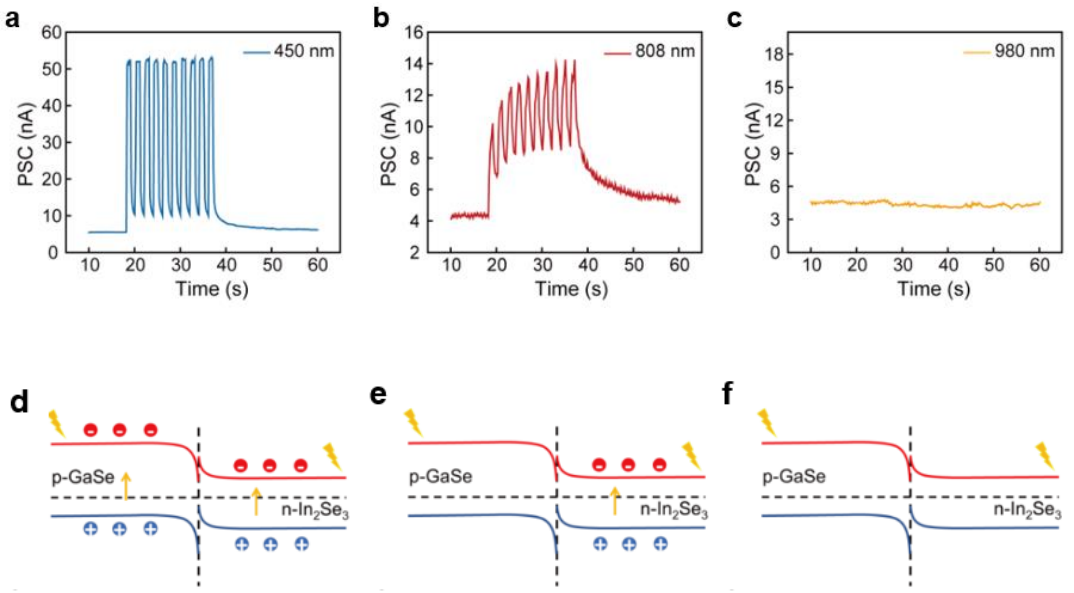

Figure 5-12 The different responses of PSC under 10 light pulses (5.7 mW cm^{-2}, 1 s) with a) 450 nm, b) 808 nm and c) 980 nm wavelength, respectively and related diagram of band structure d-f)

5.3.3 Emulation of Pavlov's dog experiment

The famous Pavlov's dog experiment was successfully executed in the device to mimic the classical conditioned reflex, which is commonly utilized by animals and humans to associate diverse stimuli together, as illustrated in Figure 5-13. Light pulses, according to the previous experimental results, can more easily create larger

PSCs than electrical pulses. Light pulses are therefore identified as food (unconditioned stimulus) to promote salivation (unconditioned response), whereas electrical pulses are employed to simulate the bell (conditioned stimulus) to trigger a conditioned reaction for the dog. A PSC of 7 nA is utilized as a threshold in this case to determine whether the device has learned to correlate electrical stimuli with light signal.

Prior to training, 20 electrical pulses were utilized to simulate bell ringing (3 V, width 175 ms), as shown in Figure 5-13a, and the PSC was eventually maintained below the threshold, indicating that it did not promote salivation. A PSC of 10 nA, on the other hand, indicated that salivation could be sustained for a long period in response to a light pulse (18.7 mW cm^{-2}, width 7 s, 450 nm wavelength), showing that the dog's unconditioned response to food was distinct and powerful (Figure 5-13b). Following that, Figure 5-13c displays the dog's training process, in which ringing the bell while feeding formed an association between the food and the bell. After training, 20 electrical pulses were delivered to the OES device, and the PSC can reach up to 8.9 nA, which is above the threshold value, as shown in Figure 5-13d. After that, the electrical pulses were applied every 120 seconds. The PSC gradually declines with increasing time, as seen in the figure, which is similar with the forgetting process in the biological nerve system. The photogating effect is primarily responsible for the success of mimicking the classical conditioned reflex, in which a large number of photogenerated carriers are separated under light by the

built-in electric field of the α-In_2Se_3/GaSe heterostructure, and the carriers require a period of time to recombine after the pulses are removed.

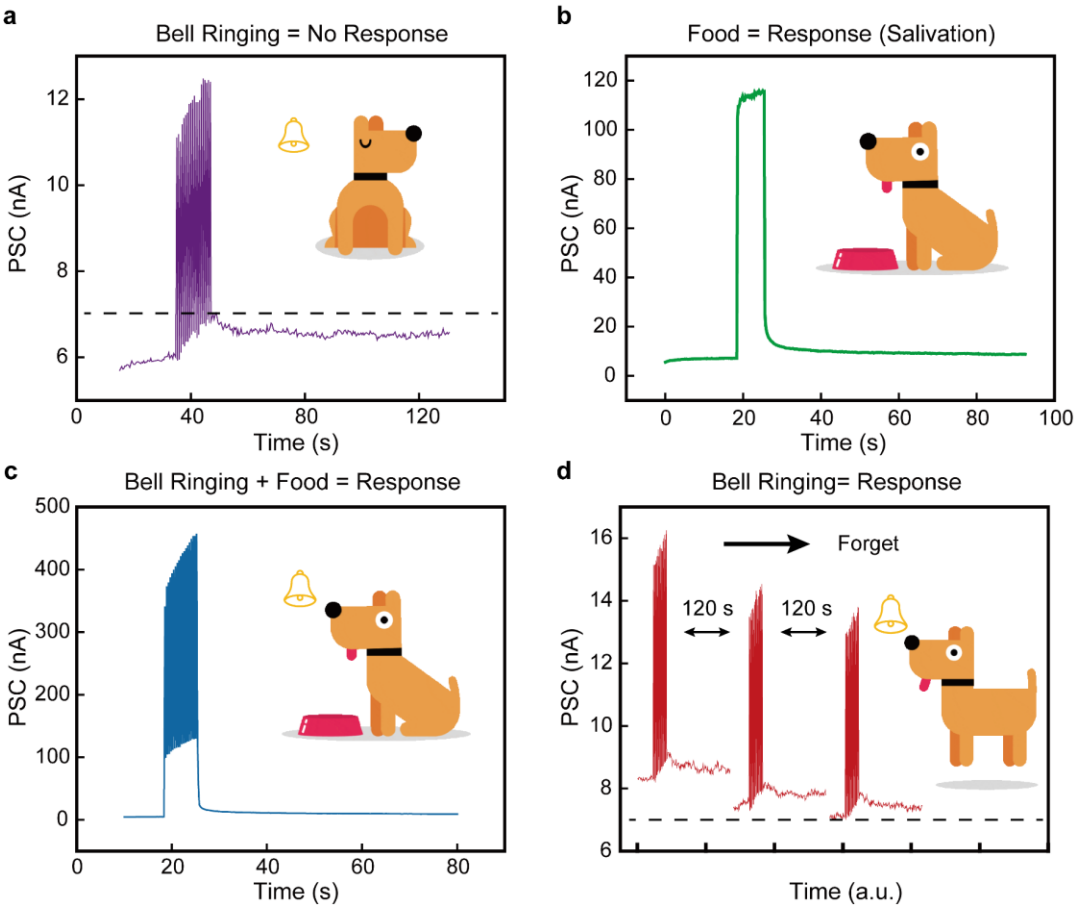

Figure 5-13 Pavlov's dog experiments to associate electrical and light stimuli together. a) 20 electrical pulses were applied, the PSC was below threshold of 7 nA (no response). b) A PSC of 10 nA was in response to a light pulse (18.7 mW cm^{-2}, width 7 s, 450 nm wavelength) (salivation). c) In order to couple different stimuli, the coincidence stimuli consist of electrical and light pulses were imposed on device. d) After training, electrical pulses alone can induce above-threshold PSCs. A forgetting behavior was observed with increasing time.

5.4 Information storage

Ferroelectric materials are promising candidates for memory due to their reversible polarization orientation that can be controlled with an applied electric field. Besides the conventional oxide ferroelectric materials, the emergence of 2D vdW semiconducting ferroelectric materials enables device miniaturization. The memory function of the OES device based on ferroelectric α-In_2Se_3 is examined in this section, and the mechanism behind is discussed and analyzed carefully. To investigate the ferroelectric domain switch in response to an applied electric field, *I-V* curves were measured by sweeping the voltage between -2 V and 2 V, -4 V and 4 V, and -6 V and 6 V in the dark, as shown in Figure 5-14. Under various sweep voltages, typical hysteresis loops are observed, with the arrows denoting the sweep direction.

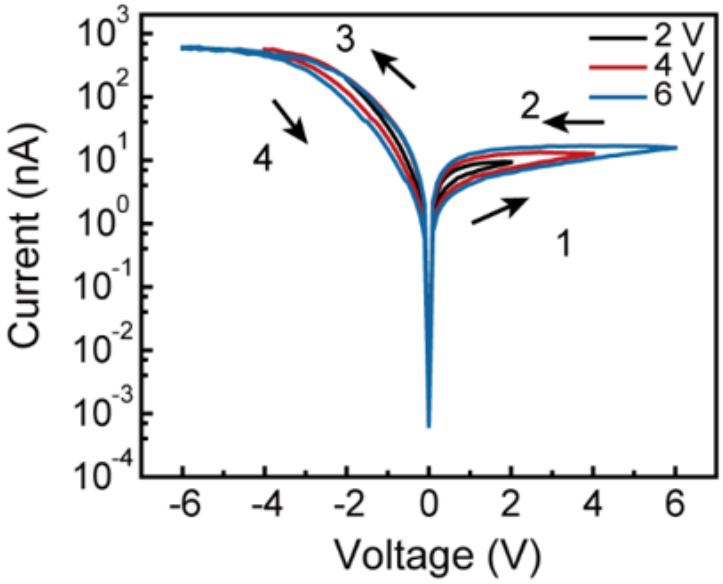

Figure 5-14 *I-V* hysteresis curves under sweep from 2 V to 6 V

As far as we know, there are two distinct directions of current variation in the hysteresis loop with respect to the applied sweep voltage for devices based on the α-In_2Se_3 channel. Figure 5-15 illustrates one case in which the currents in stages 1 and 3 of the hysteresis loops are less than those in stages 2 and 4. Such hysteresis loops are observable in devices where metal electrodes are prepared on α-In_2Se_3 using E-beam, bringing the surface and sides of α-In_2Se_3 into contact with the metal, and energetic particles produced during the electrode preparation process may damage the interface between the metal and α-In_2Se_3.[111] IP ferroelectricity is thought to have a significant role in this case, according to the literature.[194] In this investigation, however, α-In_2Se_3 was added after the electrodes were prepared to form vdW contacts. Currents are greater in stages 2 and 3 of hysteresis loops than in stages 1 and 4. We speculate that the difference in direction of current change is principally determined by the presence of OOP ferroelectricity, in which bound charges on the top and bottom surfaces can operate as a gate. Gu et al. presented a planar device based on α-In_2Se_3 with one electrode on the bottom surface of the left side and the other on the top surface of the right side, considering that both IP and OOP ferroelectricity have an effect on the device.[195] Their work also obtained a hysteresis loop similar to ours, implying that our speculation regarding the influence of OOP ferroelectricity on the *I-V* curve is reasonable.

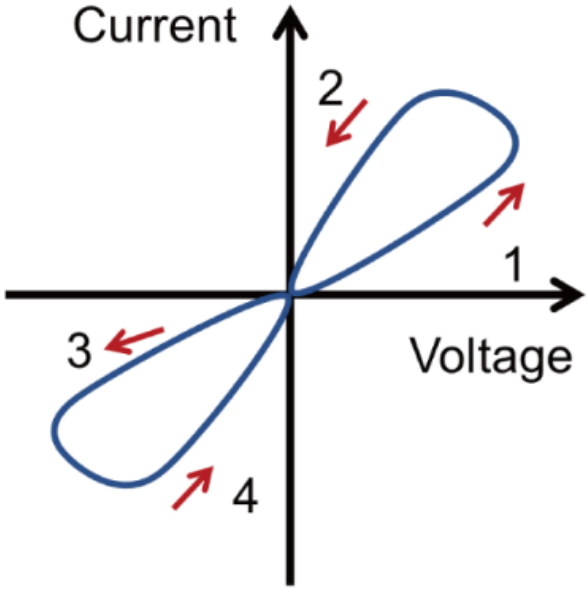

Figure 5-15 The *I-V* curve where the currents of stage 1 and 3 in hysteresis loop are smaller than those of stage 2 and 4

When a high voltage is applied to the device, diode-like rectification behavior is observed, and the forward and reverse directions can be switched. As displayed in Figure 5-16a, when a -20 V electrical pulse (width 5 s) is applied, the direction of ferroelectric polarization (P_{FE}) switches to the left, promoting current flow at negative voltage bias. In Figure 5-16b, the 50 periodic photoresponses up to 0.1 pA are shown under zero bias and light pulses (18.7 mW cm^{-2}, 0.1 Hz, 450 nm wavelength). The ferroelectric photovoltaic effect is responsible for the self-power characteristic. When a voltage of 20 V was applied to the device, the ferroelectric polarization direction was reversed to the right, and the rectification of the diode was also switched (Figure 5-16c). Figure 5-16d exhibits a lower photoresponse current than Figure 5b, which may be attributable to the fact that some ferroelectric domains

are not completely reversed. Thus, the information stored in the OES device as memory can be read nondestructively using light pulses.

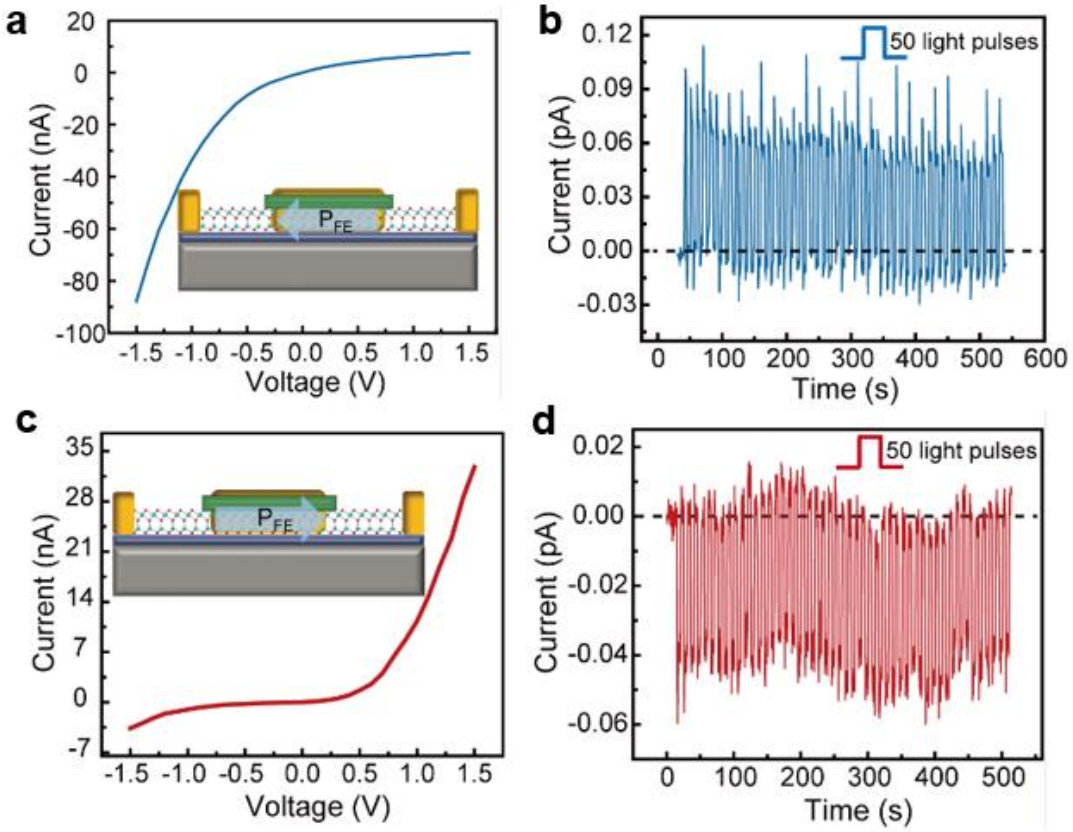

Figure 5-16 a) *I-V* curve under ferroelectric polarization orientation shown in inset. b) Photoresponse at zero bias voltage under 50 light pulses (18.7 mW cm^{-2}, 0.1 Hz, 450 nm wavelength) and the ferroelectric polarization orientation in a). c) The *I-V* curve after a positive voltage applied, and d) corresponding photoresponse

5.5 Information processing

Apart from sensing external inputs and storing data, logic functions built into synaptic devices are very desirable. Here, light and electrical pulses are defined as input signals, and the PSC is utilized to represent the output value. Figure 5-17 shows

how light and electrical pulses are used to implement AND logic. To ensure the logic function's precision, "0" and "1" are carefully defined. The logic input's "1" and "0" are determined by light switching (9.1 W cm^{-2}, 450 nm), and for electrical signals, the 0.1 V bias is considered as the "0," while the 3 V electrical pulse is considered as the "1." When a "1" of light and a "1" of electrical signal are applied to the synaptic device simultaneously, the "1" of PSC output over the threshold (30 nA) can be observed. The large difference between the "0" and "1" states of PSC currents allows for a wide range of threshold definitions while also improving the precision of logic operation.

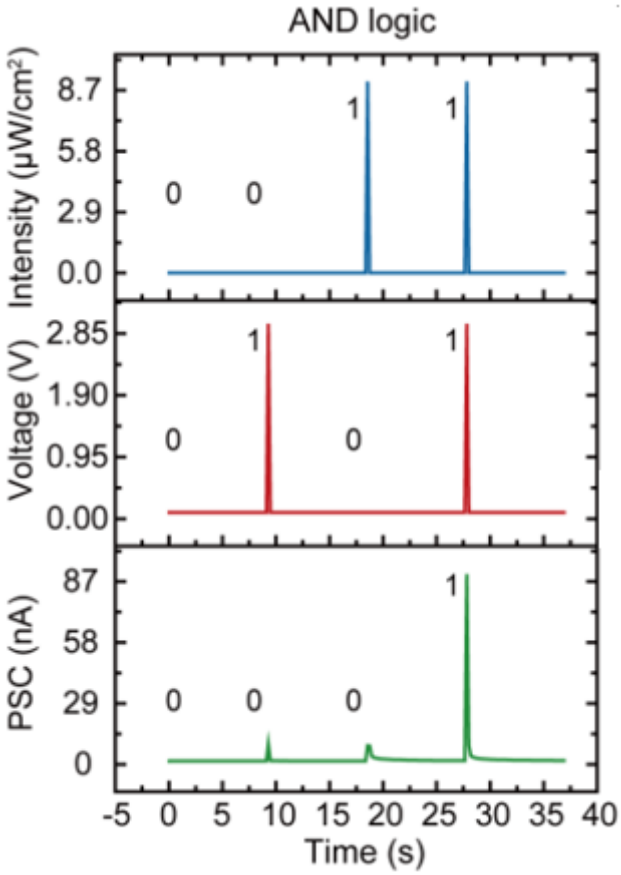

Figure 5-17 The “AND” logic function of device under light and electrical pulses

Another logic function is proposed based on the ferroelectricity of α-In_2Se_3, in which the top gate separates the channel into left and right halves. Figure 5-18a illustrates the *I-V* curve of the p-GaSe/n-In_2Se_3 heterostructure. The rectification behavior is due to the built-in electric field in the heterostructure, and the hysteresis loop is attributed to the polarization inversion characteristic of ferroelectric heterostructures.[161, 196] When the polarization orientations of left half channel are identical to those of the right half, Figure 5-18b shows a photoresponse (0.1 pA) to light pulses (450 nm wavelength, 18.7 mW cm^{-2}, period 10 s, width 3 s) at zero bias. As illustrated in Figure 5-18c, when an electrical pulse (15 V, 5 s) is applied between the top gate and the drain, the polarity of the ferroelectricity in the right half of the channel is inverted, and no rise in PSC is observed under the light pulse. The coincidence of electrical and optical signals may create further opportunities for synaptic devices to expand their logic functionalities.

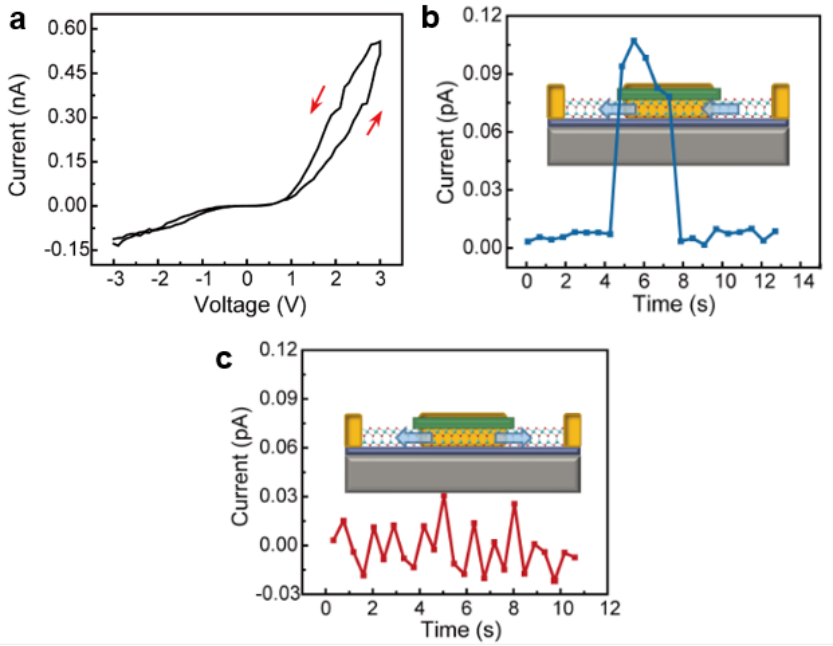

Figure 5-18 a) The *I-V* hysteresis curves of ferroelectric α-In_2Se_3/GaSe vdW heterostructure. Photoresponse at zero bias voltage when the polarization orientations of two parts of channels are b) the same or c) opposite. The orientation of polarization is indicated by the arrows

A crossbar composed of synaptic devices, such as the OES device used in this study, is a promising candidate for resolving the bottleneck problem associated with von Neumann-based computing systems. Crossbar can significantly reduce signal latency by avoiding data travel and allowing for parallel computation. In Figure 5-19, each input terminal is defined as a neuron in the input layer (X_i), and each output terminal is described as a neuron in the output layer (Y_j). Additionally, W_{ij} is used to represent the weight of the synaptic device that connects the neurons. When voltage is applied to a programmable synaptic device, the conductance changes in response to the external voltage, and the crossbar can be used to simulate a neural network because the current is additive.

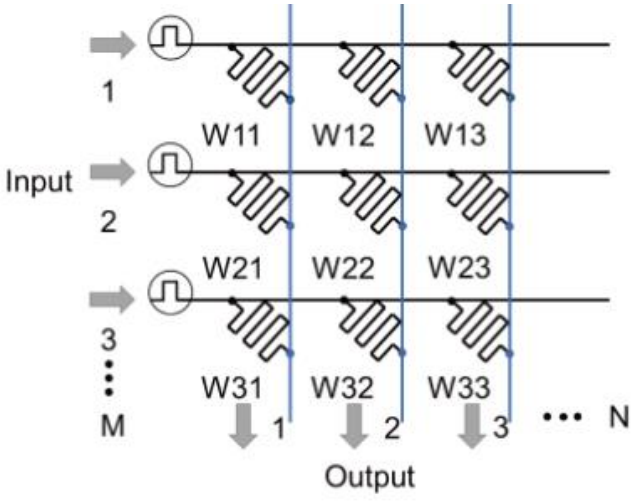

Figure 5-19 The basic principle of crossbar

To verify the feasibility of the crossbar made up of OES devices, an artificial neural network (ANN) was developed using the extracted device parameters. The ANN was then used to simulate and evaluate the crossbar's behavior. Due to its unique nonlinearity in comparison to other logics, XOR is used to train ANN in this case. As seen in Figure 5-20a, the ANN is composed of three layers: the input layer, the hidden layer, and the output layer. The program code was written in Python using the back propagation algorithm and the crosssim platform's neural core. In the first step, the computer generates an 8×3 array and a 3×4 array at random to represent the weights between the input and hidden layers, as well as between the hidden and output layers. Following that, the input values are propagated through the ANN (using the sigmoid activation function) to produce the output values. After the difference between the output value and the target output value is multiplied by the input value and the learning rate (0.2), it is added to the original weight array to complete the update. The process above is repeated until the convergence requirement is satisfied or the output value of ANN meets the specified target value. The accuracy rate is computed in this case using:

$$\text{Accuracy rate}=\left[1-\frac{\sum_{i=1}^{n}|Y_{Oi}-Y_{Ti}|}{n}\right]\times 100\% \quad (n=4) \tag{5-4}$$

Where Y_O denotes the output and Y_T represents the target value. As illustrated in Figure 5-20b, the accuracy of the crossbar made up of OES devices for XOR logic can be maintained at 90% after 1000 trainings, which is comparable to the accuracy achieved under ideal software conditions (96%). To further validate the reliability of

crossbar, we introduce Gaussian write noise into the weight update process. The results indicate that the pace of convergence is reduced, but the ultimate accuracy can still be close to 90%. Indeed, ANNs can make right judgments as long as their accuracy rate exceeds 50%. As a result, our proposed synaptic device-based neural network is capable of performing logical computations.

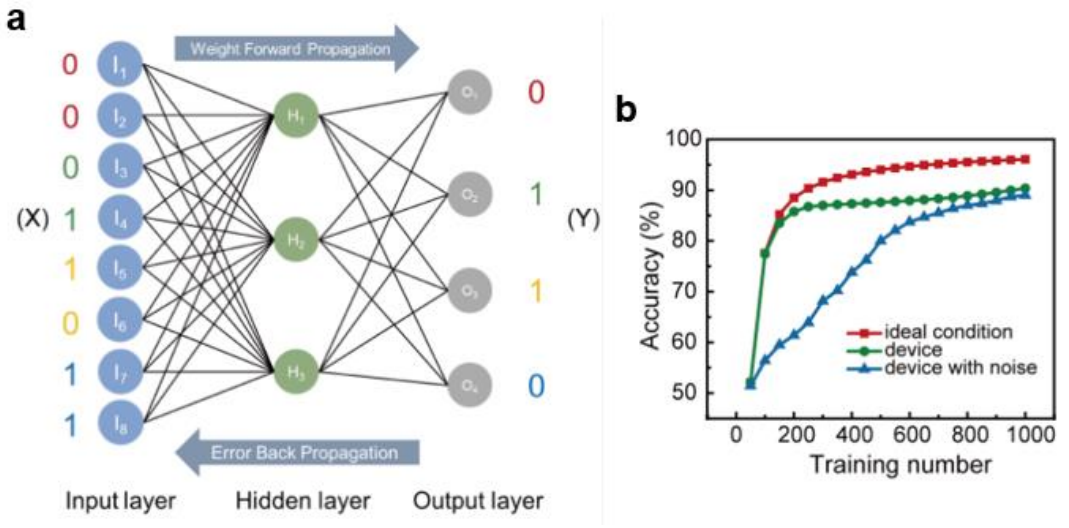

Figure 5-20 a) An ANN built to perform XOR logic. b) Accuracy rate as a function of training number

5.6 Summary

In conclusion, a novel multifunctional optoelectronic synaptic device based on ferroelectric α-In_2Se_3/GaSe vdW heterostructures is presented to imitate the entire human visual system at the device level. By switching the ferroelectric domains, the plasticity of biological synapses such as PPF, LTP, and LTD are realized. The photonic synapse's wavelength selectivity implies that our OES device not only converts light stimuli to electrical signals, but also has the ability to detect colors in

the same way that the retina does. Additionally, the success of Pavlov's dog experiment demonstrates the ability of our device to couple light and electrical signals, emulating assisted learning in the human brain. More importantly, in addition to synaptic behaviors, logic functions and memory are integrated in the device with the help of unique ferroelectricity, thus accomplishing the task of mimicking the visual cortex. In a simulated ANN, a high accuracy rate for XOR logic was attained, demonstrating the robustness of crossbar. Our work makes a substantial advancement toward emulating the entire human visual system using ferroelectric vdW heterostructures, and the multifunctional synaptic device presented in this study has tremendous potential for processing complicated visual information.

Chapter 6 Conclusion and Future Prospect

6.1 Conclusion

The emergence of 2D layered piezoelectric and ferroelectric materials offers the possibility to solve the problems of conventional oxide dominated ferroelectric materials. For example, the 2D ferroelectric α-In_2Se_3 can exhibit robust ferroelectricity even at the atomic level, which effectively addresses the critical thickness problem of ferroelectrics. Although HfO_2 has also been reported to show intrinsic ferroelectricity in monolayer thickness, lattice matching is still a great challenge for preparation of heterostructure, whereas vdW contacts of layered materials do not need to concern about this issue. On the other hand, compared to the wide forbidden band gap in conventional ferroelectrics, the semiconductor properties of ferroelectric α-In_2Se_3 show great potential in the field of electronics and optoelectronics. In this thesis, the effect of piezoelectricity on the physical properties of α-In_2Se_3 is investigated and discussed, and electronic and optoelectronic synaptic devices based on α-In_2Se_3 are proposed for neuromorphic computing.

Firstly, controllable biaxial strain was imposed on the α-In_2Se_3 nanosheets by an electromechanical device which consists of a piezoelectric substrate and metal electrodes. When applying strain, a red shift of Raman spectra can be observed. The Grüneisen parameter is used to analyze the effect of strain on vibrational behavior. Photoluminescence characterization shows that there is a blue shift can reach up to almost 215.82 meV per 1% strain which is much higher than conventional

semiconductors. The effect of strain induced piezoelectric field on band gap is elaborated in detail. The method provides a powerful tool to investigate the effect of biaxial strain on the band gap of 2D materials and promise a wide range of applications in nanostructured optoelectronic devices.

Secondly, with the help of ferroelectricity in 2D vdW α-In_2Se_3, an artificial neuronal device was elaborately designed. And the linearly separable and nonseparable logic functions can be performed in a single artificial neuron based on the principle of combinational logic and stateful logic, respectively. Besides, a photoswitchable manner between AND and OR logic is observed in the device due to the semiconducting nature of ferroelectric α-In_2Se_3. On the other hand, as a neuronal device, complex functions analogous to that of the brain are highly desirable for AI to handle diverse tasks in the real world. Therefore, the essential synaptic behaviors of multi-terminal devices are demonstrated, and the gate terminal not only serves as a pre-synapse but also a modulator. An artificial neural network is built based on our proposed device for handwritten digital image recognition to verify the reliability of the device. Moreover, successful emulation of desiring or refusing food-intake allows the device to carry out positive and negative feedback when faced to complicated situations. The experimental results make an important step toward simplifying the current redundant artificial neural networks and provide an adaptable strategy for AI to solve complex tasks in the real world.

Thirdly, a multifunctional optoelectronic synapse based on 2D ferroelectric α-In_2Se_3/GaSe vdW heterostructure is proposed to emulate the entire biological visual system. Visual perception and color recognition can be achieved in the device by photogating effect for mimicking the retina. Electric modulation mode plays the role of transmitting excitatory signals. Moreover, beyond synaptic behaviors, logic functions and memory are incorporated in the device thanks to the help of unique ferroelectricity, which achieve the objective of emulating the visual cortex in the brain. The success of Pavlov's dog experiment further validates our device's ability of handling multi-input signals. Furthermore, a high accuracy rate for XOR logic and image recognition is obtained in a simulated artificial neural network. With visual perception, logic function and memory enabled at the single device level, our proposed multifunctional optoelectronic synapse can process complex visual information and may simplify the design of artificial visual systems.

6.2 Future prospect

The discovery of 2D vdW ferroelectric materials is a significant milestone towards tackling the challenges faced by conventional ferroelectric materials, such as critical thickness, wide forbidden band width, etc. Among the several 2D ferroelectric materials discovered so far, α-In_2Se_3 due to its 1.4 eV band gap and robust ferroelectric properties even in monolayers at room temperature shows great potential for applications in multifunctional, ultra-thin electronics and optoelectronics. In 2016, ferroelectric properties in α-In_2Se_3 were successfully

predicted, in the following years preparation of α-In_2Se_3 by CVD and MBE was reported and some simple devices such as FETs were demonstrated. However, it should be noted that the exploration and application of α-In_2Se_3 is still at an initial stage, and many issues as well as challenges need to be addressed.

First of all, most of the current devices based on α-In_2Se_3 are prepared using mechanically exfoliated nanosheets. The exfoliated nanosheets derived from crystals ensure the high crystalline quality of the material, but it greatly limits the preparation of devices at the circuit level. Moreover, the size of the nanosheets obtained so far from bottom-up methods such as MBE and CVD can only be maintained at the micron scale. In addition, the piezoelectric properties in ferroelectric α-In_2Se_3 also provide abundant opportunities for the preparation of flexible devices, such as pressure sensors, etc. For α-In_2Se_3, a great advantage over conventional ferroelectric materials is its semiconducting properties and high response to visible light, therefore, how to design electronic and optoelectronic synaptic devices in order to facilitate the development of neuromorphic computing is also an interesting topic. Anyway, in our opinion, there is still a lot of work that needs to be done to exploit ferroelectric α-In_2Se_3, especially in the field of multifunctional devices.

References

1. Alexe, M.; Harnagea, C.; Hesse, D.; Gosele, U., Patterning and switching of nanosize ferroelectric memory cells. *Appl. Phy.s Lett.* **1999,** *75* (12), 1793-1795.

2. Hoffman, J.; Pan, X. A.; Reiner, J. W.; Walker, F. J.; Han, J. P.; Ahn, C. H.; Ma, T. P., Ferroelectric field effect transistors for memory applications. *Adv. Mater.* **2010,** *22* (26-27), 2957-2961.

3. Huang, H. T., Solar energy ferroelectric photovoltaics. *Nat. Photonics* **2010,** *4* (3), 134-135.

4. Mason, W. P., Piezoelectricity, its history and applications. *J. Acoust. Soc. Am.* **1981,** *70* (6), 1561-1566.

5. Saigusa, Y., Quartz-based piezoelectric materials. In *Advanced Piezoelectric Materials*, Elsevier: 2017; pp 197-233.

6. Ballas, R.G., The piezoelectric effect–an indispensable solid state effect for contemporary actuator and sensor technologies. *J. Phys.: Conf. Ser.* **2021,** *1775* (1), 012012.

7. Fang, H., Introduction. In *Novel Devices Based on Relaxor Ferroelectric PMN-PT Single Crystals*, Springer Singapore: Singapore, 2020; pp 1-28.

8. Lone, I. H. ; Aslam, J. ; Radwan, N. R. E. ; Bashal, A. H. ; Ajlouni, A. F. A.; Akhter, A., Multiferroic ABO_3 transition metal oxides: a rare interaction of ferroelectricity and magnetism. *Nanoscale Res. Lett.* **2019**, *14*, 142.

9. Li, J. Y.; Liu, Y. M.; Zhang, Y. H.; Cai, H. L.; Xiong, R. G., Molecular ferroelectrics: where electronics meet biology. *Phys. Chem. Chem. Phys.* **2013,** *15* (48), 20786-20796.

10. Shahrokhi, S.; Gao, W. X.; Wang, Y. T.; Anandan, P. R.; Rahaman, M. Z.; Singh, S.; Wang, D. Y.; Cazorla, C.; Yuan, G. L.; Liu, J. M.; Wu, T., Emergence of ferroelectricity in halide perovskites. *Small Methods* **2020,** *4* (8), 2000149.

11. Valasek, J., Piezo-electric and allied phenomena in Rochelle salt. *Physical review* **1921,** *17* (4), 475.

12. Rabuffetti, F. A.; Richard L. B., Complex perovskite oxide nanocrystals: low-temperature synthesis and crystal structure. *Dalton Trans.* **2014**, *43*, 14499-14513.

13. Sawaguchi, E., Ferroelectricity versus antiferroelectricity in the solid solutions of $PbZrO_3$ and $PbTiO_3$. *J. Phys. Soc. Jpn.* **1953,** *8* (5), 615-629.

14. Kawai, H., The piezoelectricity of poly (vinylidene fluoride). *Jpn. J. Appl. Phys.* **1969,** *8* (7), 975.

15. Chen, X.; Han, X.; Shen, Q. D., PVDF-based ferroelectric polymers in modern flexible electronics. *Adv. Electron. Mater.* **2017,** *3* (5), 1600460.

16. Mathews, S.; Ramesh, R.; Venkatesan, T.; Benedetto, J., Ferroelectric field effect transistor based on epitaxial perovskite heterostructures. *Science* **1997,** *276* (5310), 238-240.

17. Ma, C.; Luo, Z.; Huang, W. C.; Zhao, L. T.; Chen, Q. L.; Lin, Y.; Liu, X.; Chen, Z. W.; Liu, C. C.; Sun, H. Y.; Jin, X.; Yin, Y. W.; Li, X. G., Sub-nanosecond memristor based on ferroelectric tunnel junction. *Nat. Commun.* **2020,** *11* (1), 1439.

18. Wang, Z. L.; Song, J. H., Piezoelectric nanogenerators based on zinc oxide nanowire arrays. *Science* **2006,** *312* (5771), 242-246.

19. Yang, Q.; Guo, X.; Wang, W. H.; Zhang, Y.; Xu, S.; Lien, D. H.; Wang, Z. L., Enhancing sensitivity of a single ZnO micro-/nanowire photodetector by piezo-phototronic effect. *Acs Nano* **2010,** *4* (10), 6285-6291.

20. Cheng, J. B.; Wang, C. L.; Zou, X. M.; Liao, L., Recent advances in optoelectronic devices based on 2D materials and their heterostructures. *Adv. Opt. Mater.* **2019,** *7* (1), 1800441.

21. Mas-Balleste, R.; Gomez-Navarro, C.; Gomez-Herrero, J.; Zamora, F., 2D materials: to graphene and beyond. *Nanoscale* **2011,** *3* (1), 20-30.

22. Tan, T.; Jiang, X. T.; Wang, C.; Yao, B. C.; Zhang, H., 2D material optoelectronics for information functional device applications: status and challenges. *Adv. Sci.* **2020,** *7* (11), 2000058.

23. Novoselov, K. S.; Geim, A. K.; Morozov, S. V.; Jiang, D.; Katsnelson, M. I.; Grigorieva, I. V.; Dubonos, S. V.; Firsov, A. A., Two-dimensional gas of massless Dirac fermions in graphene. *Nature* **2005,** *438* (7065), 197-200.

24. Li, C. L.; Cao, Q.; Wang, F. Z.; Xiao, Y. Q.; Li, Y. B.; Delaunay, J. J.; Zhu, H. W., Engineering graphene and TMDs based van der Waals heterostructures for photovoltaic and photoelectrochemical solar energy conversion. *Chem. Soc. Rev.* **2018,** *47* (13), 4981-5037.

25. Wang, J. G.; Ma, F. C.; Liang, W. J.; Sun, M. T., Electrical properties and applications of graphene, hexagonal boron nitride (h-BN), and graphene/h-BN heterostructures. *Mater. Today Phys.* **2017,** *2*, 6-34.

26. Naguib, M.; Mochalin, V. N.; Barsoum, M. W.; Gogotsi, Y., 25th Anniversary Article: MXenes: A new family of two-dimensional materials. *Adv. Mater.* **2014,** *26* (7), 992-1005.

27. Zhang, Q. M.; Xu, H. S.; Fang, F.; Cheng, Z. Y.; Xia, F.; You, H., Critical thickness of crystallization and discontinuous change in ferroelectric behavior with thickness in ferroelectric polymer thin films. *J. Appl. Phys.* **2001,** *89* (5), 2613-2616.

28. Hinchet, R.; Khan, U.; Falconi, C.; Kim, S. W., Piezoelectric properties in two-dimensional materials: simulations and experiments. *Mater. Today* **2018,** *21* (6), 611-630.

29. Cui, C. J.; Xue, F.; Hu, W. J.; Li, L. J., Two-dimensional materials with piezoelectric and ferroelectric functionalities. *Npj 2d Mater. Appl.* **2018,** *2*, 1-14.

30. Wu, W. Z.; Wang, L.; Li, Y. L.; Zhang, F.; Lin, L.; Niu, S. M.; Chenet, D.; Zhang, X.; Hao, Y. F.; Heinz, T. F.; Hone, J.; Wang, Z. L., Piezoelectricity of single-atomic-layer MoS_2 for energy conversion and piezotronics. *Nature* **2014,** *514* (7523), 470.

31. Zhu, H. Y.; Wang, Y.; Xiao, J.; Liu, M.; Xiong, S. M.; Wong, Z. J.; Ye, Z. L.; Ye, Y.; Yin, X. B.; Zhang, X., Observation of piezoelectricity in free-standing monolayer MoS_2. *Nat. Nanotechnol.* **2015,** *10* (2), 151-155.

32. Tang, Q.; Jiang, D. E., Stabilization and band-gap tuning of the 1T-MoS_2 monolayer by covalent functionalization. *Chem. Mater.* **2015,** *27* (10), 3743-3748.

33. Jiang, C. M.; Li, Q. K.; Huang, J. J.; Bi, S.; Ji, R. N.; Guo, Q. L., Single-layer MoS_2 mechanical resonant piezo-sensors with high mass sensitivity. *Acs. Appl. Mater. Inter.* **2020,** *12* (37), 41991-41998.

34. Zhang, K.; Peng, M. Z.; Wu, W.; Guo, J. M.; Gao, G. Y.; Liu, Y. D.; Kou, J. Z.; Wen, R. M.; Lei, Y.; Yu, A. F.; Zhang, Y.; Zhai, J. Y.; Wang, Z. L., A flexible p-CuO/n-MoS_2 heterostructure photodetector with enhanced photoresponse by the piezo-phototronic effect. *Mater. Horiz.* **2017,** *4* (2), 274-280.

35. Wu, M. H.; Lee, J. T.; Chung, Y. J.; Srinivaas, M.; Wu, J. M., Ultrahigh efficient degradation activity of single- and few-layered $MoSe_2$ nanoflowers in dark by piezo-catalyst effect. *Nano Energy* **2017,** *40*, 369-375.

36. Thakur, D.; Sharma, M.; Vaish, R.; Balakrishnan, V., WS_2 monolayer for piezo-phototronic dye degradation and bacterial disinfection. *Acs. Appl. Nano Mater.* **2021,** *4* (8), 7879-7887.

37. Blonsky, M. N.; Zhuang, H. L.; Singh, A. K.; Hennig, R. G., Ab initio prediction of piezoelectricity in two-dimensional materials. *Acs Nano* **2015,** *9* (10), 9885-9891.

38. Michel, K. H.; Verberck, B., Theory of elastic and piezoelectric effects in two-dimensional hexagonal boron nitride. *Phys. Rev. B* **2009,** *80* (22), 224301.

39. Duerloo, K. A. N.; Reed, E. J., Flexural Electromechanical Coupling: A nanoscale emergent property of boron nitride bilayers. *Nano Lett.* **2013,** *13* (4), 1681-1686.

40. Li, Y. L.; Rao, Y.; Mak, K. F.; You, Y. M.; Wang, S. Y.; Dean, C. R.; Heinz, T. F., Probing symmetry properties of few-layer MoS_2 and h-BN by optical second-harmonic generation. *Nano Lett.* **2013,** *13* (7), 3329-3333.

41. Zelisko, M.; Hanlumyuang, Y.; Yang, S. B.; Liu, Y. M.; Lei, C. H.; Li, J. Y.; Ajayan, P. M.; Sharma, P., Anomalous piezoelectricity in two-dimensional graphene nitride nanosheets. *Nat. Commun.* **2014,** *5*, 4284.

42. Noor-A-Alam, M.; Kim, H. J.; Shin, Y. H., Dipolar polarization and piezoelectricity of a hexagonal boron nitride sheet decorated with hydrogen and fluorine. *Phys. Chem. Chem. Phys.* **2014,** *16* (14), 6575-6582.

43. Lu, A. Y.; Zhu, H. Y.; Xiao, J.; Chuu, C. P.; Han, Y. M.; Chiu, M. H.; Cheng, C. C.; Yang, C. W.; Wei, K. H.; Yang, Y. M.; Wang, Y.; Sokaras, D.; Nordlund, D.; Yang, P. D.; Muller, D. A.; Chou, M. Y.; Zhang, X.; Li, L. J., Janus monolayers of transition metal dichalcogenides. *Nat. Nanotechnol.* **2017,** *12* (8), 744.

44. Gruverman, A.; Wu, D.; Lu, H.; Wang, Y.; Jang, H. W.; Folkman, C. M.; Zhuravlev, M. Y.; Felker, D.; Rzchowski, M.; Eom, C. B.; Tsymbal, E. Y., Tunneling electroresistance effect in ferroelectric tunnel junctions at the nanoscale. *Nano Lett.* **2009,** *9* (10), 3539-3543.

45. Cheema, S. S.; Kwon, D.; Shanker, N.; dos Reis, R.; Hsu, S. L.; Xiao, J.; Zhang, H. G.; Wagner, R.; Datar, A.; McCarter, M. R.; Serrao, C. R.; Yadav, A. K.; Karbasian, G.; Hsu, C. H.; Tan, A. J.; Wang, L. C.; Thakare, V.; Zhang, X.; Mehta, A.; Karapetrova, E.; Chopdekar, R. V.; Shafer, P.; Arenholz, E.; Hu, C. M.; Proksch, R.; Ramesh, R.; Ciston, J.; Salahuddin, S., Enhanced ferroelectricity in ultrathin films grown directly on silicon. *Nature* **2020,** *580* (7804), 478.

46. Yuan, S. G.; Luo, X.; Chan, H. L.; Xiao, C. C.; Dai, Y. W.; Xie, M. H.; Hao, J. H., Room-temperature ferroelectricity in $MoTe_2$ down to the atomic monolayer limit. *Nat. Commun.* **2019,** *10*, 1775.

47. Chang, K.; Liu, J. W.; Lin, H. C.; Wang, N.; Zhao, K.; Zhang, A. M.; Jin, F.; Zhong, Y.; Hu, X. P.; Duan, W. H.; Zhang, Q. M.; Fu, L.; Xue, Q. K.; Chen, X.; Ji, S. H., Discovery of robust in-plane ferroelectricity in atomic-thick SnTe. *Science* **2016,** *353* (6296), 274-278.

48. Liu, F. C.; You, L.; Seyler, K. L.; Li, X. B.; Yu, P.; Lin, J. H.; Wang, X. W.; Zhou, J. D.; Wang, H.; He, H. Y.; Pantelides, S. T.; Zhou, W.; Sharma, P.;

Xu, X. D.; Ajayan, P. M.; Wang, J. L.; Liu, Z., Room-temperature ferroelectricity in $CuInP_2S_6$ ultrathin flakes. *Nat. Commun.* **2016,** *7*, 12357.

49. Zhou, Y.; Wu, D.; Zhu, Y. H.; Cho, Y. J.; He, Q.; Yang, X.; Herrera, K.; Chu, Z. D.; Han, Y.; Downer, M. C.; Peng, H. L.; Lai, K. J., Out-of-plane piezoelectricity and ferroelectricity in layered alpha-In_2Se_3 nanoflakes. *Nano Lett.* **2017,** *17* (9), 5508-5513.

50. Cui, C. J.; Hu, W. J.; Yan, X. G.; Addiego, C.; Gao, W. P.; Wang, Y.; Wang, Z.; Li, L. Z.; Cheng, Y. C.; Li, P.; Zhang, X. X.; Alshareef, H. N.; Wu, T.; Zhu, W. G.; Pan, X. Q.; Li, L. J., Intercorrelated in-plane and out-of-plane ferroelectricity in ultrathin two-dimensional layered semiconductor In_2Se_3. *Nano Lett.* **2018,** *18* (2), 1253-1258.

51. Roldan, R.; Castellanos-Gomez, A.; Cappelluti, E.; Guinea, F., Strain engineering in semiconducting two-dimensional crystals. *J. Phys-Condens. Mat.* **2015,** *27* (31), 313201.

52. Ni, Z. H.; Yu, T.; Lu, Y. H.; Wang, Y. Y.; Feng, Y. P.; Shen, Z. X., Uniaxial strain on graphene: raman spectroscopy study and band-gap opening. *Acs Nano* **2008,** *2* (11), 2301-2305.

53. Wang, Y. L.; Cong, C. X.; Yang, W. H.; Shang, J. Z.; Peimyoo, N.; Chen, Y.; Kang, J. Y.; Wang, J. P.; Huang, W.; Yu, T., Strain-induced direct-indirect bandgap transition and phonon modulation in monolayer WS_2. *Nano Res.* **2015,** *8* (8), 2562-2572.

54. Wu, W. Z.; Wang, L.; Yu, R. M.; Liu, Y. Y.; Wei, S. H.; Hone, J.; Wang, Z. L., Piezophototronic effect in single-atomic-layer MoS_2 for strain-gated flexible optoelectronics. *Adv. Mater.* **2016,** *28* (38), 8463-8468.

55. Zheng, D. Q.; Zhao, Z. M.; Huang, R.; Nie, J. H.; Li, L. J.; Zhang, Y., High-performance piezo-phototronic solar cell based on two-dimensional materials. *Nano Energy* **2017,** *32*, 448-453.

56. Thiele, C.; Dorr, K.; Bilani, O.; Rodel, J.; Schultz, L., Influence of strain on the magnetization and magnetoelectric effect in $La_{(0.7)}A_{(0.3)}MnO_{(3)}$/PMN-PT(001) (A=Sr,Ca). *Phys. Rev. B* **2007,** *75* (5), 054408.

57. Zhang, Y.; Gao, G. Y.; Chan, H. L. W.; Dai, J. Y.; Wang, Y.; Hao, J. H., Piezo-phototronic effect-induced dual-mode light and ultrasound emissions from ZnS:Mn/PMN-PT thin-film structures. *Adv. Mater.* **2012,** *24* (13), 1729-1735.

58. Bai, G. X.; Zhang, Y.; Hao, J. H., Tuning of near-infrared luminescence of $SrTiO^{3}:Ni^{2+}$ thin films grown on piezoelectric PMN-PT via strain engineering. *Sci. Rep.* **2014,** *4*, 5724.

59. Wu, Z. P.; Zhang, Y.; Bai, G. X.; Tang, W. H.; Gao, J.; Hao, J. H., Effect of biaxial strain induced by piezoelectric PMN-PT on the upconversion photoluminescence of $BaTiO_3$:Yb/Er thin films. *Opt. Express* **2014,** *22* (23), 29014-29019.

60. Hui, Y. Y.; Liu, X. F.; Jie, W. J.; Chan, N. Y.; Hao, J. H.; Hsu, Y. T.; Li, L. J.; Guo, W. L.; Lau, S. P., Exceptional tunability of band energy in a compressively strained trilayer MoS_2 sheet. *Acs Nano* **2013,** *7* (8), 7126-7131.

61. Jie, W. J.; Hui, Y. Y.; Zhang, Y.; Lau, S. P.; Hao, J. H., Effects of controllable biaxial strain on the Raman spectra of monolayer graphene prepared by chemical vapor deposition. *Appl. Phys. Lett.* **2013,** *102* (22), 223112.

62. Bhattacharjee, S.; Wigchering, R.; Manning, H. G.; Boland, J. J.; Hurley, P. K., Emulating synaptic response in n- and p-channel MoS_2 transistors by utilizing charge trapping dynamics. *Sci. Rep.* **2020,** *10* (1), 12178.

63. Huh, W.; Lee, D.; Lee, C. H., Memristors based on 2D materials as an artificial synapse for neuromorphic electronics. *Adv. Mater.* **2020,** *32* (51), 2002092.

64. Chua, L., Memristor-the missing circuit element. *IEEE Transactions on circuit theory* **1971,** *18* (5), 507-519.

65. Strukov, D. B.; Snider, G. S.; Stewart, D. R.; Williams, R. S., The missing memristor found. *Nature* **2008,** *453* (7191), 80-83.

66. Yan, X. B.; Zhao, J. H.; Liu, S.; Zhou, Z. Y.; Liu, Q.; Chen, J. S.; Liu, X. Y., Memristor with Ag-cluster-doped TiO_2 films as artificial synapse for neuroinspired computing. *Adv. Funct. Mater.* **2018,** *28* (1), 1705320.

67. Li, B.; Liu, Y. Q.; Wan, C. J.; Liu, Z. Y.; Wang, M.; Qi, D. P.; Yu, J. C.; Cai, P. Q.; Xiao, M.; Zeng, Y.; Chen, X. D., Mediating short-term plasticity in an artificial memristive synapse by the orientation of silica mesopores. *Adv. Mater.* **2018,** *30* (16), 1706395.

68. Sangwan, V. K.; Jariwala, D.; Kim, I. S.; Chen, K. S.; Marks, T. J.; Lauhon, L. J.; Hersam, M. C., Gate-tunable memristive phenomena mediated by grain boundaries in single-layer MoS_2. *Nat. Nanotechnol.* **2015,** *10* (5), 403-406.

69. Sangwan, V. K.; Lee, H. S.; Bergeron, H.; Balla, I.; Beck, M. E.; Chen, K. S.; Hersam, M. C., Multi-terminal memtransistors from polycrystalline monolayer molybdenum disulfide. *Nature* **2018,** *554* (7693), 500.

70. Yan, X. B.; Zhao, Q. O. L.; Chen, A. P.; Zhao, J. H.; Zhou, Z. Y.; Wang, J. J.; Wang, H.; Zhang, L.; Li, X. Y.; Xiao, Z. A.; Wang, K. Y.; Qin, C. Y.; Wang,

G.; Pei, Y. F.; Li, H.; Ren, D. L.; Chen, J. S.; Liu, Q., Vacancy-induced synaptic behavior in 2D WS_2 nanosheet-based memristor for low-power neuromorphic computing. *Small* **2019,** *15* (24), 1901423.

71. Yoshida, M.; Suzuki, R.; Zhang, Y. J.; Nakano, M.; Iwasa, Y., Memristive phase switching in two-dimensional 1T-TaS_2 crystals. *Sci. Adv.* **2015,** *1* (9), e1500606

72. Mou, X.; Tang, J. S.; Lyu, Y. J.; Zhang, Q. T.; Yang, S. Y.; Xu, F.; Liu, W.; Xu, M. H.; Zhou, Y.; Sun, W.; Zhong, Y. A.; Gao, B.; Yu, P.; Qian, H.; Wu, H. Q., Analog memristive synapse based on topotactic phase transition for high-performance neuromorphic computing and neural network pruning. *Sci. Adv.* **2021,** *7* (29), eabh0648.

73. Guo, R.; Zhou, Y. X.; Wu, L. J.; Wang, Z. R.; Lim, Z. S.; Yan, X. B.; Lin, W. N.; Wang, H.; Yoong, H. Y.; Chen, S. H.; Ariando; Venkatesan, T.; Wang, J.; Chow, G. M.; Gruverman, A.; Miao, X. S.; Zhu, Y. M.; Chen, J. S., Control of synaptic plasticity learning of ferroelectric tunnel memristor by nanoscale interface engineering. *Acs. Appl. Mater. Inter.* **2018,** *10* (15), 12862-12869.

74. Ren, Y.; Yang, J. Q.; Zhou, L.; Mao, J. Y.; Zhang, S. R.; Zhou, Y.; Han, S. T., Gate-tunable synaptic plasticity through controlled polarity of charge trapping in fullerene composites. *Adv. Funct. Mater.* **2018,** *28* (50), 1805599.

75. Zhao, J.; Liu, F.; Huang, Q.; Lu, T. K.; Xi, M. Q.; Peng, L. M.; Liang, X. L., Charge trap-based carbon nanotube transistor for synaptic function mimicking. *Nano Res.* **2021,** *14* (11), 4258-4263.

76. Yang, F. S.; Li, M. J.; Lee, M. P.; Ho, I. Y.; Chen, J. Y.; Ling, H. F.; Li, Y. Z.; Chang, J. K.; Yang, S. H.; Chang, Y. M.; Lee, K. C.; Chou, Y. C.; Ho, C.

H.; Li, W. W.; Lien, C. H.; Lin, Y. F., Oxidation-boosted charge trapping in ultra-sensitive van der Waals materials for artificial synaptic features. *Nat. Commun.* **2020,** *11* (1), 2972.

77. Kim, M. K.; Lee, J. S., Ferroelectric analog synaptic transistors. *Nano Lett.* **2019,** *19* (3), 2044-2050.

78. Tian, B. B.; Liu, L.; Yan, M. G.; Wang, J. L.; Zhao, Q. B.; Zhong, N.; Xiang, P. H.; Sun, L.; Peng, H.; Shen, H.; Lin, T.; Dkhi, B.; Meng, X. J.; Chu, J. H.; Tang, X. D.; Duan, C. G., A robust artificial synapse based on organic ferroelectric polymer. *Adv. Electron. Mater.* **2019,** *5* (1), 1800600.

79. Han, X.; Xu, Z.; Wu, W.; Liu, X.; Yan, P.; Pan, C., Recent progress in optoelectronic synapses for artificial visual-perception system. *Small Structures* **2020,** *1* (3), 2000029.

80. Li, H. K.; Chen, T. P.; Liu, P.; Hu, S. G.; Liu, Y.; Zhang, Q.; Lee, P. S., A light-stimulated synaptic transistor with synaptic plasticity and memory functions based on $InGaZnO_x$-Al_2O_3 thin film structure. *J. Appl. Phys.* **2016,** *119* (24), 244505.

81. Dai, S. L.; Wu, X. H.; Liu, D. P.; Chu, Y. L.; Wang, K.; Yang, B.; Huang, J., Light-stimulated synaptic devices utilizing interfacial effect of organic field-effect transistors. *Acs. Appl. Mater. Inter.* **2018,** *10* (25), 21472-21480.

82. Wang, S. Y.; Chen, C. S.; Yu, Z. H.; He, Y. L.; Chen, X. Y.; Wan, Q.; Shi, Y.; Zhang, D. W.; Zhou, H.; Wang, X. R.; Zhou, P., A MoS_2/PTCDA hybrid heterostructure synapse with efficient photoelectric dual modulation and versatility. *Adv. Mater.* **2019,** *31* (3), 1806227.

83. Qian, C.; Oh, S.; Choi, Y.; Kim, J. H.; Sun, J.; Huang, H.; Yang, J. L.; Gao, Y. L.; Park, J. H.; Cho, J. H., Solar-stimulated optoelectronic synapse based

on organic heterostructure with linearly potentiated synaptic weight for neuromorphic computing. *Nano Energy* **2019,** *66*, 104095.

84. Lee, M.; Lee, W.; Choi, S.; Jo, J. W.; Kim, J.; Park, S. K.; Kim, Y. H., Brain-inspired photonic neuromorphic devices using photodynamic amorphous oxide semiconductors and their persistent photoconductivity. *Adv. Mater.* **2017,** *29* (28), 1700951.

85. Seo, S.; Lee, J. J.; Lee, R. G.; Kim, T. H.; Park, S.; Jung, S.; Lee, H. K.; Andreev, M.; Lee, K. B.; Jung, K. S.; Oh, S.; Lee, H. J.; Kim, K. S.; Yeom, G. Y.; Kim, Y. H.; Park, J. H., An optogenetics-inspired flexible van der Waals optoelectronic synapse and its application to a convolutional neural network. *Adv. Mater.* **2021,** *33* (40), 2102980.

86. Gao, E. L.; Lin, S. Z.; Qinn, Z.; Buehler, M. J.; Feng, X. Q.; Xu, Z. P., Mechanical exfoliation of two-dimensional materials. *J. Mech. Phys. Solids* **2018,** *115*, 248-262.

87. Huang, Y.; Pan, Y. H.; Yang, R.; Bao, L. H.; Meng, L.; Luo, H. L.; Cai, Y. Q.; Liu, G. D.; Zhao, W. J.; Zhou, Z.; Wu, L. M.; Zhu, Z. L.; Huang, M.; Liu, L. W.; Liu, L.; Cheng, P.; Wu, K. H.; Tian, S. B.; Gu, C. Z.; Shi, Y. G.; Guo, Y. F.; Cheng, Z. G.; Hu, J. P.; Zhao, L.; Yang, G. H.; Sutter, E.; Sutter, P.; Wang, Y. L.; Ji, W.; Zhou, X. J.; Gao, H. J., Universal mechanical exfoliation of large-area 2D crystals. *Nat. Commun.* **2020,** *11* (1), 2453.

88. Paton, K. R.; Varrla, E.; Backes, C.; Smith, R. J.; Khan, U.; O'Neill, A.; Boland, C.; Lotya, M.; Istrate, O. M.; King, P.; Higgins, T.; Barwich, S.; May, P.; Puczkarski, P.; Ahmed, I.; Moebius, M.; Pettersson, H.; Long, E.; Coelho, J.; O'Brien, S. E.; McGuire, E. K.; Sanchez, B. M.; Duesberg, G. S.; McEvoy, N.;

Pennycook, T. J.; Downing, C.; Crossley, A.; Nicolosi, V.; Coleman, J. N., Scalable production of large quantities of defect-free few-layer graphene by shear exfoliation in liquids. *Nat. Mater.* **2014,** *13* (6), 624-630.

89. Zheng, J.; Zhang, H.; Dong, S. H.; Liu, Y. P.; Nai, C. T.; Shin, H. S.; Jeong, H. Y.; Liu, B.; Loh, K. P., High yield exfoliation of two-dimensional chalcogenides using sodium naphthalenide. *Nat. Commun.* **2014,** *5*, 2995.

90. Naguib, M.; Kurtoglu, M.; Presser, V.; Lu, J.; Niu, J. J.; Heon, M.; Hultman, L.; Gogotsi, Y.; Barsoum, M. W., Two-dimensional nanocrystals produced by exfoliation of Ti_3AlC_2. *Adv. Mater.* **2011,** *23* (37), 4248-4253.

91. Cai, X. K.; Luo, Y. T.; Liu, B.; Cheng, H. M., Preparation of 2D material dispersions and their applications. *Chem. Soc. Rev.* **2018,** *47* (16), 6224-6266.

92. Li, D. W.; Xiao, Z. Y.; Mu, S.; Wang, F.; Liu, Y.; Song, J. F.; Huang, X.; Jiang, L. J.; Xiao, J.; Liu, L.; Ducharme, S.; Cui, B.; Hong, X.; Jiang, L.; Silvain, J. F.; Lu, Y. F., A facile space-confined solid-phase sulfurization strategy for growth of high-quality ultrathin molybdenum disulfide single crystals. *Nano Lett.* **2018,** *18* (3), 2021-2032.

93. Lim, Y. F.; Priyadarshi, K.; Bussolotti, F.; Gogoi, P. K.; Cui, X. Y.; Yang, M.; Pan, J. S.; Tong, S. W.; Wang, S. J.; Pennycook, S.; Goh, K. E. J.; Wee, A. T. S.; Wong, S. L.; Chi, D. Z., Modification of vapor phase concentrations in MoS_2 growth using a NiO foam barrier. *Acs Nano* **2018,** *12* (2), 1339-1349.

94. Yu, H.; Liao, M. Z.; Zhao, W. J.; Liu, G. D.; Zhou, X. J.; Wei, Z.; Xu, X. Z.; Liu, K. H.; Hu, Z. H.; Deng, K.; Zhou, S. Y.; Shi, J. A.; Gu, L.; Shen, C.; Zhang, T. T.; Du, L. J.; Xie, L.; Zhu, J. Q.; Chen, W.; Yang, R.; Shi, D. X.; Zhang,

G. Y., Wafer-scale growth and transfer of highly-oriented monolayer MoS_2 continuous films. *Acs Nano* **2017,** *11* (12), 12001-12007.

95. Xia, J.; Huang, X.; Liu, L. Z.; Wang, M.; Wang, L.; Huang, B.; Zhu, D. D.; Li, J. J.; Gu, C. Z.; Meng, X. M., CVD synthesis of large-area, highly crystalline $MoSe_2$ atomic layers on diverse substrates and application to photodetectors. *Nanoscale* **2014,** *6* (15), 8949-8955.

96. Perea-Lopez, N.; Lin, Z.; Pradhan, N. R.; Iniguez-Rabago, A.; Elias, A. L.; McCreary, A.; Lou, J.; Ajayan, P. M.; Terrones, H.; Balicas, L.; Terrones, M., CVD-grown monolayered MoS_2 as an effective photosensor operating at low-voltage. *2d Mater.* **2014,** *1* (1), 011004.

97. Zhang, Y.; Ji, Q. Q.; Han, G. F.; Ju, J.; Shi, J. P.; Ma, D. L.; Sun, J. Y.; Zhang, Y. S.; Li, M. J.; Lang, X. Y.; Zhang, Y. F.; Liu, Z. F., Dendritic, transferable, strictly monolayer MoS_2 flakes synthesized on $SrTiO_3$ single crystals for efficient electrocatalytic applications. *Acs Nano* **2014,** *8* (8), 8617-8624.

98. Li, C.; Zhang, Y.; Ji, Q. Q.; Shi, J. P.; Chen, Z. L.; Zhou, X. B.; Fang, Q. Y.; Zhang, Y. F., Substrate effect on the growth of monolayer dendritic MoS_2 on $LaAlO_3$ (100) and its electrocatalytic applications. *2d Mater.* **2016,** *3* (3), 035001.

99. Zhang, Y.; Ji, Q. Q.; Wen, J. X.; Li, J.; Li, C.; Shi, J. P.; Zhou, X. B.; Shi, K. B.; Chen, H. J.; Li, Y. C.; Deng, S. Z.; Xu, N. S.; Liu, Z. F.; Zhang, Y. F., Monolayer MoS_2 dendrites on a symmetry-disparate $SrTiO_3$ (001) substrate: formation mechanism and interface interaction. *Adv. Funct. Mater.* **2016,** *26* (19), 3299-3305.

100. Chen, Y. B.; Sun, J. Y.; Gao, J. F.; Du, F.; Han, Q.; Nie, Y. F.; Chen, Z.; Bachmatiuk, A.; Priydarshi, M. K.; Ma, D. L.; Song, X. J.; Wu, X. S.; Xiong, C.

Y.; Rummeli, M. H.; Ding, F.; Zhang, Y. F.; Liu, Z. F., Growing uniform graphene disks and films on molten glass for heating devices and cell culture. *Adv. Mater.* **2015,** *27* (47), 7839-7846.

101. McCreary, K. M.; Hanbicki, A. T.; Robinson, J. T.; Cobas, E.; Culbertson, J. C.; Friedman, A. L.; Jernigan, G. G.; Jonker, B. T., Large-area synthesis of continuous and uniform MoS_2 monolayer films on graphene. *Adv. Funct. Mater.* **2014,** *24* (41), 6449-6454.

102. Lee, E.; Lee, S. G.; Lee, W. H.; Lee, H. C.; Nguyen, N. N.; Yoo, M. S.; Cho, K., Direct CVD growth of a graphene/MoS_2 heterostructure with interfacial bonding for two-dimensional electronics. *Chem. Mater.* **2020,** *32* (11), 4544-4552.

103. Li, M. L.; Zhu, Y. S.; Li, T. S.; Lin, Y.; Cai, H. B.; Li, S. J.; Ding, H. Y.; Pan, N.; Wang, X. P., One-step CVD fabrication and optoelectronic properties of SnS_2/SnS vertical heterostructures. *Inorg. Chem. Front.* **2018,** *5* (8), 1828-1835.

104. Li, F.; Xu, B. Y.; Yang, W.; Qi, Z. Y.; Ma, C.; Wang, Y. J.; Zhang, X. H.; Luo, Z. R.; Liang, D. L.; Li, D.; Li, Z. W.; Pan, A. L., High-performance optoelectronic devices based on van der Waals vertical MoS_2/$MoSe_2$ heterostructures. *Nano Res.* **2020,** *13* (4), 1053-1059.

105. Yan, A. M.; Velasco, J.; Kahn, S.; Watanabe, K.; Taniguchi, T.; Wang, F.; Crommie, M. F.; Zettl, A., Direct growth of single- and few-layer MoS_2 on h-BN with preferred relative rotation angles. *Nano Lett.* **2015,** *15* (10), 6324-6331.

106. Li, M. Y.; Shi, Y. M.; Cheng, C. C.; Lu, L. S.; Lin, Y. C.; Tang, H. L.; Tsai, M. L.; Chu, C. W.; Wei, K. H.; He, J. H.; Chang, W. H.; Suenaga, K.; Li, L. J., Epitaxial growth of a monolayer WSe_2-MoS_2 lateral p-n junction with an atomically sharp interface. *Science* **2015,** *349* (6247), 524-528.

107. Xie, S. E.; Tu, L. J.; Han, Y. M.; Huang, L. J.; Kang, K.; Lao, K. U.; Poddar, P.; Park, C.; Muller, D. A.; DiStasio, R. A.; Park, J., Coherent, atomically thin transition-metal dichalcogenide superlattices with engineered strain. *Science* **2018,** *359* (6380), 1131-1135.

108. Guo, H. W.; Hu, Z.; Liu, Z. B.; Tian, J. G., Stacking of 2D materials. *Adv. Funct. Mater.* **2021,** *31* (4), 2007810.

109. Cao, Y.; Fatemi, V.; Fang, S.; Watanabe, K.; Taniguchi, T.; Kaxiras, E.; Jarillo-Herrero, P., Unconventional superconductivity in magic-angle graphene superlattices. *Nature* **2018,** *556* (7699), 43.

110. Li, Y. T.; Huang, L.; Zhong, M. Z.; Wei, Z. M.; Li, J. B., An efficient and low-cost photolithographic-pattern-transfer technique to fabricate electrode arrays for micro-/nanoelectronics. *Adv. Mater. Technol.* **2016,** *1* (1), 1600001.

111. Liu, Y.; Guo, J.; Zhu, E. B.; Liao, L.; Lee, S. J.; Ding, M. N.; Shakir, I.; Gambin, V.; Huang, Y.; Duan, X. F., Approaching the Schottky-Mott limit in van der Waals metal-semiconductor junctions. *Nature* **2018,** *557* (7707), 696.

112. Williams, D. B.; Carter, C. B., The transmission electron microscope. In *Transmission electron microscopy*, Springer: 1996; pp 3-17.

113. Gruverman, A.; Alexe, M.; Meier, D., Piezoresponse force microscopy and nanoferroic phenomena. *Nat. Commun.* **2019,** *10*, 1661.

114. Soergel, E., Piezoresponse force microscopy (PFM). *J. Phys. D. Appl. Phys.* **2011,** *44* (46), 464003.

115. Salehzadeh, O.; Djavid, M.; Tran, N. H.; Shih, I.; Mi, Z., Optically pumped two-dimensional MoS_2 lasers operating at room-temperature. *Nano Lett.* **2015,** *15* (8), 5302-6.

116. Xia, X. W. a. F., Stacked 2D materials shed light. *Nat. Mater.* **2015,** *14*, 264.

117. Yang, Z.; Jie, W.; Mak, C. H.; Lin, S.; Lin, H.; Yang, X.; Yan, F.; Lau, S. P.; Hao, J., Wafer-scale synthesis of high-quality semiconducting two-dimensional layered inse with broadband photoresponse. *ACS Nano* **2017,** *11* (4), 4225-4236.

118. Lin, P.; Zhu, L.; Li, D.; Xu, L.; Pan, C.; Wang, Z., Piezo-phototronic effect for enhanced flexible MoS_2/WSe_2 van der Waals photodiodes. *Adv. Funct. Mater.* **2018,** *28* (35) 1802849.

119. Wu, W.; Wang, L.; Yu, R.; Liu, Y.; Wei, S. H.; Hone, J.; Wang, Z. L., Piezophototronic effect in single-atomic-layer Mos_2 for strain-gated flexible optoelectronics. *Adv. Mater.* **2016,** *28* (38), 8463-8468.

120. Conley, H. J.; Wang, B.; Ziegler, J. I.; Haglund, R. F.; Pantelides, S. T.; Bolotin, K. I., Bandgap engineering of strained monolayer and bilayer MoS_2. *Nano Lett.* **2013,** *13* (8), 3626-3630.

121. Ding, W. J.; Zhu, J. B.; Wang, Z.; Gao, Y. F.; Xiao, D.; Gu, Y.; Zhang, Z. Y.; Zhu, W. G., Prediction of intrinsic two-dimensional ferroelectrics in In_2Se_3 and other III_2-VI_3 van der Waals materials. *Nat. Commun.* **2017,** *8*, 14956.

122. Xue, F.; Zhang, J. W.; Hu, W. J.; Hsu, W. T.; Han, A.; Leung, S. F.; Huang, J. K.; Wan, Y.; Liu, S. H.; Zhang, J. L.; He, J. H.; Chang, W. H.; Wang, Z. L.; Zhang, X. X.; Li, L. J., Multidirection piezoelectricity in mono- and multilayered hexagonal alpha-In_2Se_3. *Acs Nano* **2018,** *12* (5), 4976-4983.

123. Jie, W. J.; Hui, Y. Y.; Chan, N. Y.; Zhang, Y.; Lau, S. P.; Hao, J. H., Ferroelectric polarization effects on the transport properties of graphene/PMN-PT field effect transistors. *J. Phys. Chem. C* **2013,** *117* (26), 13747-13752.

124. Wan, S.; Li, Y.; Li, W.; Mao, X.; Zhu, W.; Zeng, H., Room-temperature ferroelectricity and a switchable diode effect in two-dimensional alpha-In_2Se_3 thin layers. *Nanoscale* **2018,** *10* (31), 14885-14892.

125. Xue, F.; Hu, W.; Lee, K. C.; Lu, L. S.; Zhang, J.; Tang, H. L.; Han, A.; Hsu, W. T.; Tu, S.; Chang, W. H.; Lien, C. H.; He, J. H.; Zhang, Z.; Li, L. J.; Zhang, X., Room-temperature ferroelectricity in hexagonally layered α-In_2Se_3 nanoflakes down to the monolayer limit. *Adv. Funct. Mater.* **2018,** *28* (50), 1803738.

126. Hanfland, M.; Beister, H.; Syassen, K., Graphite under pressure: Equation of state and first-order Raman modes. *Phys. Rev. B Condens. Matter.* **1989,** *39* (17), 12598-12603.

127. Mohiuddin, T. M. G.; Lombardo, A.; Nair, R. R.; Bonetti, A.; Savini, G.; Jalil, R.; Bonini, N.; Basko, D. M.; Galiotis, C.; Marzari, N.; Novoselov, K. S.; Geim, A. K.; Ferrari, A. C., Uniaxial strain in graphene by Raman spectroscopy:Gpeak splitting, Grüneisen parameters, and sample orientation. *Phys. Rev. B* **2009,** *79* (20), 205433.

128. Shao, R. W.; Zheng, K.; Wei, B.; Zhang, Y. F.; Li, Y. J.; Han, X. D.; Zhang, Z.; Zou, J., Bandgap engineering and manipulating electronic and optical properties of ZnO nanowires by uniaxial strain. *Nanoscale* **2014,** *6* (9), 4936-41.

129. Shiri, D.; Kong, Y.; Buin, A.; Anantram, M. P., Strain induced change of bandgap and effective mass in silicon nanowires. *Appl. Phys. Lett.* **2008,** *93* (7), 073114.

130. Rastelli, A.; Ding, F.; Plumhof, J. D.; Kumar, S.; Trotta, R.; Deneke, C.; Malachias, A.; Atkinson, P.; Zallo, E.; Zander, T.; Herklotz, A.; Singh, R.; Křápek, V.; Schröter, J. R.; Kiravittaya, S.; Benyoucef, M.; Hafenbrak, R.; Jöns, K. D.;

Thurmer, D. J.; Grimm, D.; Bester, G.; Dörr, K.; Michler, P.; Schmidt, O. G., Controlling quantum dot emission by integration of semiconductor nanomembranes onto piezoelectric actuators. *physica status solidi (b)* **2012,** *249* (4), 687-696.

131. Mak, K. F.; Lui, C. H.; Shan, J.; Heinz, T. F., Observation of an electric-field-induced band gap in bilayer graphene by infrared spectroscopy. *Phys. Rev. Lett.* **2009,** *102* (25), 256405.

132. Liu, X.; Zhang, Q.; Yip, J. N.; Xiong, Q.; Sum, T. C., Wavelength tunable single nanowire lasers based on surface plasmon polariton enhanced Burstein-Moss effect. *Nano Lett.* **2013,** *13* (11), 5336-43.

133. F. Widmann, J. S., B. Daudin, G. Feuillet, J. L. Rouvie`re, and N. T. Pelekanos, Blue-light emission from GaN self-assembled quantum dots due to giant piezoelectric effect. *Phys. Rev. B* **1998,** *58* (24), R15989(R).

134. Sanguinetti, S.; Gurioli, M.; Grilli, E.; Guzzi, M.; Henini, M., Piezoelectric-induced quantum-confined Stark effect in self-assembled InAs quantum dots grown on (N11) GaAs substrates. *Appl. Phys. Lett.* **2000,** *77* (13), 1982-1984.

135. Gotoh, H.; Tawara, T.; Kobayashi, Y.; Kobayashi, N.; Saitoh, T., Piezoelectric effects on photoluminescence properties in 10-nm-thick InGaN quantum wells. *Appl. Phys. Lett.* **2003,** *83* (23), 4791-4793.

136. Hu, L.; Huang, X., Peculiar electronic, strong in-plane and out-of-plane second harmonic generation and piezoelectric properties of atom-thick α-M_2X_3 (M = Ga, In; X = S, Se): role of spontaneous electric dipole orientations. *RSC Advances* **2017,** *7* (87), 55034-55043.

137. Raranskii, N. D.; Balazyuk, V. N.; Kovalyuk, Z. D.; Mel'nik, N. I.; Gevik, V. B., Crystal growth and elastic properties of In_2Se_3. *Inorg. Mater.* **2011,** *47* (11), 1174-1177.

138. C. Julien, M. E., K. Kambas AND M. Balkanski, Electrical and optical properties of In_2Se_3 thin films. *Thin Solid Films* **1986,** *137* (1), 27-37.

139. Robin B. Jacobs-Gedrim, M. S., Nikhil Jain, Christopher A. Durcan, Michael T. Murphy, Thomas M. Murray, Richard J. Matyi, Richard L. Moore, II, and Bin Yu, Extraordinary photoresponse in two-dimensional In_2Se_3 nanosheets. *ACS Nano* **2014,** *8* (1), 514–521.

140. Park, H. L.; Kim, H.; Lim, D.; Zhou, H.; Kim, Y. H.; Lee, Y.; Park, S.; Lee, T. W., Retina-inspired carbon nitride-based photonic synapses for selective detection of uv light. *Adv. Mater.* **2020,** *32* (11), 1906899.

141. Seo, S.; Jo, S. H.; Kim, S.; Shim, J.; Oh, S.; Kim, J. H.; Heo, K.; Choi, J. W.; Choi, C.; Oh, S.; Kuzum, D.; Wong, H. S. P.; Park, J. H., Artificial optic-neural synapse for colored and color-mixed pattern recognition. *Nat. Commun.* **2018,** *9*, 5106.

142. Xue, F.; He, X.; Wang, Z. Y.; Retamal, J. R. D.; Chai, Z.; Jing, L. L.; Zhang, C. H.; Fang, H.; Chai, Y.; Jiang, T.; Zhang, W. D.; Alshareef, H. N.; Ji, Z. G.; Li, L. J.; He, J. H.; Zhang, X. X., Giant ferroelectric resistance switching controlled by a modulatory terminal for low-power neuromorphic in-memory computing. *Adv. Mater.* **2021,** *33* (21), 2008709.

143. Zhang, Y. H.; Qu, P.; Ji, Y.; Zhang, W. H.; Gao, G. R.; Wang, G. R.; Song, S.; Li, G. Q.; Chen, W. G.; Zheng, W. M.; Chen, F.; Pei, J.; Zhao, R.;

Zhao, M. G.; Shi, L. P., A system hierarchy for brain-inspired computing. *Nature* **2020,** *586* (7829), 378.

144. Zhou, F. C.; Zhou, Z.; Chen, J. W.; Choy, T. H.; Wang, J. L.; Zhang, N.; Lin, Z. Y.; Yu, S. M.; Kang, J. F.; Wong, H. S. P.; Chai, Y., Optoelectronic resistive random access memory for neuromorphic vision sensors. *Nat. Nanotechnol.* **2019,** *14* (8), 776.

145. Rosenblatt, F., The perceptron: A probabilistic model for information storage and organization in the brain. *Psychological Review* **1958,** *65*, 386–408.

146. M. Marvin, P. Seymour, Perceptrons, M.I.T. Press, 1969. *M. Marvin, P. Seymour, Perceptrons, M.I.T. Press, 1969.*

147. Gidon, A.; Zolnik, T. A.; Fidzinski, P.; Bolduan, F.; Papoutsi, A.; Poirazi, P.; Holtkamp, M.; Vida, I.; Larkum, M. E., Dendritic action potentials and computation in human layer 2/3 cortical neurons. *Science* **2020,** *367* (6473), 83.

148. Indiveri, G.; Douglas, F., Robotic vision - Neuromorphic vision sensors. *Science* **2000,** *288* (5469), 1189-1190.

149. Morton, G. J.; Cummings, D. E.; Baskin, D. G.; Barsh, G. S.; Schwartz, M. W., Central nervous system control of food intake and body weight. *Nature* **2006,** *443* (7109), 289-295.

150. Schwartz, M. W.; Woods, S. C.; Porte, D.; Seeley, R. J.; Baskin, D. G., Central nervous system control of food intake. *Nature* **2000,** *404* (6778), 661-671.

151. Ge, C.; Liu, C. X.; Zhou, Q. L.; Zhang, Q. H.; Du, J. Y.; Li, J. K.; Wang, C.; Gu, L.; Yang, G. Z.; Jin, K. J., A Ferrite Synaptic Transistor with topotactic transformation. *Adv. Mater.* **2019,** *31* (19), 1900379.

152. Tran, M. D.; Kim, H.; Kim, J. S.; Doan, M. H.; Chau, T. K.; Vu, Q. A.; Kim, J. H.; Lee, Y. H., Two-terminal multibit optical memory via van der Waals heterostructure. *Adv. Mater.* **2019,** *31* (7), 1807075.

153. Xu, W.; Cho, H.; Kim, Y. H.; Kim, Y. T.; Wolf, C.; Park, C. G.; Lee, T. W., Organometal halide perovskite artificial synapses. *Adv. Mater.* **2016,** *28* (28), 5916.

154. Hua, Q. L.; Cui, X.; Liu, H. T.; Pan, C. F.; Hu, W. G.; Wang, Z. L., Piezotronic synapse based on a single GaN microwire for artificial sensory systems. *Nano Lett.* **2020,** *20* (5), 3761-3768.

155. Luo, S. W.; Liao, K. H.; Lei, P. X.; Jiang, T.; Chen, S. Y.; Xie, Q.; Luo, W. B.; Huang, W.; Yuan, S. G.; Jie, W. J.; Hao, J. H., A synaptic memristor based on two-dimensional layered WSe_2 nanosheets with short- and long-term plasticity dagger. *Nanoscale* **2021,** *13* (13), 6654-6660.

156. Luo, Z. D.; Xia, X.; Yang, M. M.; Wilson, N. R.; Gruverman, A.; Alexe, M., Artificial optoelectronic synapses based on ferroelectric field-effect enabled 2D transition metal dichalcogenide memristive transistors. *Acs Nano* **2020,** *14* (1), 746-754.

157. Tang, J.; He, C. L.; Tang, J. S.; Yue, K.; Zhang, Q. T.; Liu, Y. Z.; Wang, Q. Q.; Wang, S. P.; Li, N.; Shen, C.; Zhao, Y. C.; Liu, J. Y.; Yuan, J. H.; Wei, Z.; Li, J. W.; Watanabe, K.; Taniguchi, T.; Shang, D. S.; Wang, S. G.; Yang, W.; Yang, R.; Shi, D. X.; Zhang, G. Y., A reliable all-2D materials artificial synapse for high energy-efficient neuromorphic computing. *Adv. Funct. Mater.* **2021,** *31* (27), 2011083.

158. Zhou, J.; Li, W.; Chen, Y.; Lin, Y. H.; Yi, M. D.; Li, J. Y.; Qian, Y. Z.; Guo, Y.; Cao, K. Y.; Xie, L. H.; Ling, H. F.; Ren, Z. J.; Xu, J. P.; Zhu, J. T.; Yan, S. K.; Huang, W., A monochloro copper phthalocyanine memristor with high-temperature resilience for electronic synapse applications. *Adv. Mater.* **2021,** *33* (5), 2006201.

159. Ghittorelli, M.; Lenz, T.; Dehsari, H. S.; Zhao, D.; Asadi, K.; Blom, P. W. M.; Kovacs-Vajna, Z. M.; de Leeuw, D. M.; Torricelli, F., Quantum tunnelling and charge accumulation in organic ferroelectric memory diodes. *Nat. Commun.* **2017,** *8*, 15741.

160. Kim, W. Y.; Kim, H. D.; Kim, T. T.; Park, H. S.; Lee, K.; Choi, H. J.; Lee, S. H.; Son, J.; Park, N.; Min, B., Graphene-ferroelectric metadevices for nonvolatile memory and reconfigurable logic-gate operations. *Nat. Commun.* **2016,** *7*, 10429.

161. Yuan, S. G.; Yang, Z. B.; Xie, C.; Yan, F.; Dai, J. Y.; Lau, S. P.; Chan, H. L. W.; Hao, J. H., Ferroelectric-driven performance enhancement of graphene field-effect transistors based on vertical tunneling heterostructures. *Adv. Mater.* **2016,** *28* (45), 10048-10054.

162. Ding, W. J.; Zhu, J. B.; Wang, Z.; Gao, Y. F.; Xiao, D.; Gu, Y.; Zhang, Z. Y.; Zhu, W. G., Prediction of intrinsic two-dimensional ferroelectrics in In_2Se_3 and other III_2-VI_3 van der Waals materials. *Nat. Commun.* **2017,** *8*, 14956.

163. Io, W. F.; Yuan, S. G.; Pang, S. Y.; Wong, L. W.; Zhao, J.; Hao, J. H., Temperature- and thickness-dependence of robust out-of-plane ferroelectricity in CVD grown ultrathin van der Waals alpha-In_2Se_3layers. *Nano Res.* **2020,** *13* (7), 1897-1902.

164. Wan, S. Y.; Li, Y.; Li, W.; Mao, X. Y.; Zhu, W. G.; Zeng, H. T., Room-temperature ferroelectricity and a switchable diode effect in two-dimensional alpha-In2Se3 thin layers. *Nanoscale* **2018,** *10* (31), 14885-14892.

165. Xue, F.; Hu, W. J.; Lee, K. C.; Lu, L. S.; Zhang, J. W.; Tang, H. L.; Han, A.; Hsu, W. T.; Tu, S. B.; Chang, W. H.; Lien, C. H.; He, J. H.; Zhang, Z. D.; Li, L. J.; Zhang, X. X., Room-temperature ferroelectricity in hexagonally layered alpha-In_2Se_3 nanoflakes down to the monolayer limit. *Adv. Funct. Mater.* **2018,** *28* (50), 1803738.

166. Si, M. W.; Saha, A. K.; Gao, S. J.; Qiu, G.; Qin, J. K.; Duan, Y. Q.; Jian, J.; Niu, C.; Wang, H. Y.; Wu, W. Z.; Gupta, S. K.; Ye, P. D. D., A ferroelectric semiconductor field-effect transistor. *Nat. Electron.* **2019,** *2* (12), 580-586.

167. Borghetti, J.; Snider, G. S.; Kuekes, P. J.; Yang, J. J.; Stewart, D. R.; Williams, R. S., 'Memristive' switches enable 'stateful' logic operations via material implication. *Nature* **2010,** *464* (7290), 873-876.

168. Liu, C. S.; Chen, H. W.; Hou, X.; Zhang, H.; Han, J.; Jiang, Y. G.; Zeng, X. Y.; Zhang, D. W.; Zhou, P., Small footprint transistor architecture for photoswitching logic and in situ memory. *Nat. Nanotechnol.* **2019,** *14* (7), 662.

169. S. Agarwal, R. B. J.-G., A. H. Hsia, D. R. Hughart, E. J. Fuller, A. A. Talin, C. D. James, S. J. Plimpton, and M. J. Marinella, Achieving ideal accuracies in analog neuromorphic computing using periodic carry. *IEEE Symposium on VLSI Technology Kyoto, Japan* **June 2017**.

170. Bodenhagen, L.; Fugl, A. R.; Jordt, A.; Willatzen, M.; Andersen, K. A.; Olsen, M. M.; Koch, R.; Petersen, H. G.; Kruger, N., An adaptable robot vision

system performing manipulation actions with flexible objects. *IEEE T. Autom. Sci. Eng.* **2014,** *11* (3), 749-765.

171. Meiring, G. A. M.; Myburgh, H. C., A review of intelligent driving style analysis systems and related artificial intelligence algorithms. *Sensors-Basel* **2015,** *15* (12), 30653-30682.

172. Grigorescu, S.; Trasnea, B.; Cocias, T.; Macesanu, G., A survey of deep learning techniques for autonomous driving. *J. Field Robot* **2020,** *37* (3), 362-386.

173. Meng, Y.; Li, F. Z.; Lan, C. Y.; Bu, X. M.; Kang, X. L.; Wei, R. J.; Yip, S.; Li, D. P.; Wang, F.; Takahashi, T.; Hosomi, T.; Nagashima, K.; Yanagida, T.; Ho, J. C., Artificial visual systems enabled by quasi-two-dimensional electron gases in oxide superlattice nanowires. *Sci. Adv.* **2020,** *6* (46), 6389.

174. Kumar, A., Computer-vision-based fabric defect detection: A survey. *ITIE* **2008,** *55* (1), 348-363.

175. Xia, Q. F.; Yang, J. J., Memristive crossbar arrays for brain-inspired computing. *Nat. Mater.* **2019,** *18* (4), 309-323.

176. Kim, Y.; Chortos, A.; Xu, W. T.; Liu, Y. X.; Oh, J. Y.; Son, D.; Kang, J.; Foudeh, A. M.; Zhu, C. X.; Lee, Y.; Niu, S. M.; Liu, J.; Pfattner, R.; Bao, Z. N.; Lee, T. W., A bioinspired flexible organic artificial afferent nerve. *Science* **2018,** *360* (6392), 998.

177. Huh, W.; Jang, S.; Lee, J. Y.; Lee, D.; Lee, D.; Lee, J. M.; Park, H. G.; Kim, J. C.; Jeong, H. Y.; Wang, G.; Lee, C. H., Synaptic barristor based on phase-engineered 2D heterostructures. *Adv. Mater.* **2018,** *30* (35), 1801447.

178. Dongyang Li, C. L., Nasir Ilyas, Xiangdong Jiang, Fucai Liu, Deen Gu,Ming Xu, Yadong Jiang, and Wei Li, Color-recognizing Si-based photonic synapse for articial visual system. *Adv. Intell. Syst.* **2020,** *2* (11), 2000107.

179. Seo, S.; Kang, B. S.; Lee, J. J.; Ryu, H. J.; Kim, S.; Kim, H.; Oh, S.; Shim, J.; Heo, K.; Oh, S.; Park, J. H., Artificial van der Waals hybrid synapse and its application to acoustic pattern recognition. *Nat. Commun.* **2020,** *11* (1), 3936.

180. Li, H. L.; Jiang, X. T.; Ye, W. B.; Zhang, H.; Zhou, L.; Zhang, F.; She, D. H.; Zhou, Y.; Han, S. T., Fully photon modulated heterostructure for neuromorphic computing. *Nano Energy* **2019,** *65*, 104000.

181. Chen, Y.; Qiu, W. J.; Wang, X. W.; Liu, W. R.; Wang, J. X.; Dai, G. Z.; Yuan, Y. B.; Gao, Y. L.; Sun, J., Solar-blind SnO_2 nanowire photo-synapses for associative learning and coincidence detection. *Nano Energy* **2019,** *62*, 393-400.

182. Geim, A. K., Graphene: Status and prospects. *Science* **2009,** *324* (5934), 1530-1534.

183. Choi, W.; Choudhary, N.; Han, G. H.; Park, J.; Akinwande, D.; Lee, Y. H., Recent development of two-dimensional transition metal dichalcogenides and their applications. *Mater. Today* **2017,** *20* (3), 116-130.

184. Wang, S. Y.; Chen, C. S.; Yu, Z. H.; He, Y. L.; Chen, X. Y.; Wan, Q.; Shi, Y.; Zhang, D. W.; Zhou, H.; Wang, X. R.; Zhou, P., A MoS_2/PTCDA hybrid heterostructure synapse with efficient photoelectric dual modulation and versatility. *Adv. Mater.* **2019,** *31* (3), 1806227.

185. Choquet, D.; Triller, A., The dynamic synapse. *Neuron* **2013,** *80* (3), 691-703.

186. Thorpe, S.; Fize, D.; Marlot, C., Speed of processing in the human visual system. *Nature* **1996,** *381* (6582), 520-522.

187. Yang, R., In-memory computing with ferroelectrics. *Nat. Electron.* **2020,** *3* (5), 237-238.

188. Lee, Y.; Park, J.; Cho, S.; Shin, Y. E.; Lee, H.; Kim, J.; Myoung, J.; Cho, S.; Kang, S.; Baig, C.; Ko, H., Flexible ferroelectric sensors with ultrahigh pressure sensitivity and linear response over exceptionally broad pressure range. *Acs Nano* **2018,** *12* (4), 4045-4054.

189. Gerra, G.; Tagantsev, A. K.; Setter, N.; Parlinski, K., Ionic polarizability of conductive metal oxides and critical thickness for ferroelectricity in $BaTiO_3$. *Phys. Rev. Lett.* **2006,** *96* (10), 107603.

190. Guo, F.; Lyu, Y. X.; Jedrzejczyk, M. B.; Zhao, Y. Q.; Io, W. F.; Bai, G. X.; Wu, W. Z.; Hao, J. H., Piezoelectric biaxial strain effects on the optical and photoluminescence spectra of 2D III-VI compound alpha-In_2Se_3 nanosheets. *Appl. Phys. Lett.* **2020,** *116* (11), 113101.

191. P.-Y. Chen, X. P., S. Yu, NeuroSim+: An integrated device-to-algorithm framework for benchmarking synaptic devices and array architectures. *IEEE International Electron Devices Meeting (IEDM) San Francisco, USA* **2017**.

192. Chung, K. H.; Chan, Y. H., A lossless compression scheme for Bayer color filter array images. *ITIP* **2008,** *17* (2), 134-144.

193. Park, W.; Pak, S.; Shim, H.; Le, H. A. N.; Im, M.; Chang, S.; Yu, J., Photometric transformation from RGB Bayer filter system to Johnson-Cousins BVR filter system. *Adv. Space Res.* **2016,** *57* (1), 509-518.

194. Lv, B. H.; Yan, Z.; Xue, W. H.; Yang, R. L.; Li, J. Y.; Ci, W. J.; Pang, R. X.; Zhou, P.; Liu, G.; Liu, Z. Y.; Zhu, W. G.; Xu, X. H., Layer-dependent ferroelectricity in 2H-stacked few-layer alpha-In_2Se_3. *Mater. Horiz.* **2021,** *8* (5), 1472-1480.

195. Gabel, M.; Gu, Y., Understanding Microscopic operating mechanisms of a van der Waals planar ferroelectric memristor. *Adv. Funct. Mater.* **2021,** *31* (9), 2009999.

196. Poh, S. M.; Tan, S. J. R.; Wang, H.; Song, P.; Abidi, I. H.; Zhao, X.; Dan, J. D.; Chen, J. S.; Luo, Z. T.; Pennycook, S. J.; Neto, A. H. C.; Loh, K. P., Molecular-Beam Epitaxy of two-dimensional In_2Se_3 and its giant electroresistance switching in ferroresistive memory junction. *Nano Lett.* **2018,** *18* (10), 6340-6346.